UNIVERSIDAD AUTÓNOMA DE MADRID
FACULTAD DE CIENCIAS
DEPARTAMENTO DE FÍSICA TEÓRICA

Lepton Flavour Violation and Dark Matter Phenomenology

Memoria de Tesis Doctoral realizada por

Bryan Zaldívar Montero

presentada ante el Departamento de Física Teórica
de la Universidad Autónoma de Madrid
para la obtención del Título de Doctor en Ciencias.

Tesis Doctoral dirigida por

Alberto Casas
Jesús Moreno
del I.F.T.
de la Universidad Autónoma de Madrid

Madrid, Febrero 2013.

AGRADECIMIENTOS

CONTENTS

CHAPTER 1

GENERAL INTRODUCTION AND MOTIVATIONS

One of the open questions in particle physics nowadays is the so-called *flavour puzzle*: why there is a hierarchical structure of fermion masses and mixings, and why there are two replicas of the lightest fermions? The leptonic sector presents even more challenging features than the quark sector, where the mixings between flavour eigenstates show an approximately perturbative texture. Indeed, in the neutrino sector the values of the mixing angles appear 'randomly' distributed, and one of the mixing angles is close to maximal. On the other hand, the masses of neutrinos are believed to be below ~ 0.3 eV, i.e. six orders of magnitude smaller than the lightest charged fermion (the electron). This should be compared with the $\sim$ five orders of magnitude expanded by the masses of the nine charged fermions (from the electron to the top mass), more or less equally distributed in between.

Certainly, the Standard Model (SM) can be trivially extended to accommodate neutrino masses. However, the previous huge gap between the neutrinos and the rest of SM particles has posed a strong motivation to develop theoretical models that could explain it. One of the most popular theoretical frameworks to accommodate such small neutrino masses is the so-called *Seesaw* mechanism. The idea is that right-handed (RH) neutrinos, which are singlets under the SM gauge group, can have large Majorana masses (as they are not controlled by the electroweak-breaking scale). Then the lightest (approximately pure left-handed) neutrinos get masses suppressed by the ratio of the Higgs VEV and the right-handed Majorana mass, thus becoming extremely light.

The Seesaw scenario can be easily formulated within a supersymmetric framework. Indeed, this is highly motivated by the fact that the massive right-handed neutrinos introduce large (logarithmic) corrections to the Higgs mass, which worsens the notorious Hierarchy-Problem of the Standard Model. On the other hand, the neutrino Yukawa couplings must present an off-diagonal structure (to generate the neutrino mixings), which in turn induces off-diagonal entries in the slepton matrices. The latter may potentially trigger processes which violate Lepton flavour, for example $\mu \to e\gamma$.

The results of the first part of this thesis have been worked out in this context. In particular we have derived an algorithm to scan the large parameter space of the (supersymmetric or not) Seesaw in a *complete way*. We have done this using the so-called $R-$parametrisation and show that the results are consisted with those obtained using other parametrisations. In particular, we demonstrate that if the scan is complete, the branching ratio $\mathrm{BR}(\mu \to e\gamma)$ is *not* sensitive to the angle θ_{13} of the neutrino (PMNS) mixing matrix. This result rectifies previous claims in the literature stating that there was a strong dependence between these two quantities. We explain that the reason for those previous results was essentially that they were based on an incomplete scan of the Seesaw parameter space.

The second part of the thesis is devoted to the study of Dark Matter (DM) issues. The existence of DM is probably the strongest evidence to believe that the Standard Model is an incomplete theory, since in order to account for the assorted observations of DM one has to extend the SM with extra degrees of freedom. There are many candidates to play the role of the DM particles. One of the best-motivated ones are the so called WIMPs (weakly interacting massive particles). The reason is the following. If one assumes that the DM-genesis occurs in the early universe, in a similar fashion to the rest of the particles, then the DM-particles lived in thermal equilibrium until the global temperature decreased below a certain threshold. Then the DM particles decoupled from the thermal bath, annihilating massively until -due to the expansion of the universe- no DM particle were able to find a partner to annihilate with. After this moment the DM abundance became "frozen". The calculation shows that for DM-masses of electroweak size (from GeV to TeV) with weak interactions (similar to neutrinos) the final DM-abundance is in the range consistent with observations. In this context, the DM particles are expected to participate not only in gravitational interactions with the rest of SM particles, but also in other kind of processes, e.g. in electroweak interactions, behaving similarly to neutrinos but with a much larger mass.

There are three basic experimental strategies to search for DM nowadays. The first one is the so-called "Indirect Detection", in which one attempts to detect the DM annihilation or decay subproducts generated in the Galactic Centre (or in Galaxy Clusters). For example, the electrons and positrons produced in processes like DM DM$\to e^+e^-$ taking place in regions where there are strong magnetic fields, will produce synchrotron radiation which can directly point towards us. Thus by measuring synchrotron fluxes from different directions in the sky, we may detect DM signals. The second experimental approach is "Direct Detection". The idea is that the DM particles of the galactic halo can interact, from time to time, with nucleons of a heavy material, e.g. xenon placed in containers deep underground, producing recoil energies which could be measured if the process is energetic enough. The third experimental strategy is the DM production in colliders. E.g. the LHC, the idea is that the DM particles could be directly produced in some proton-proton collisions. Once produced, the DM particles would escape the detector, as neutrinos do, contributing to the missing energy. In this way a DM signal can be identified indirectly by studying the other

-visible- products of the scattering. This occurs for instance in processes like $q\bar{q} \to j$ DM DM, in which a quark-antiquark pair annihilate into a pair of DM particles plus a jet (which can be originated by a gluon emitted by the initial states).

In our results, we first combine different bounds coming from collider searches of assorted (leptonic or hadronic) nature, as LEP and Tevatron. We show that, considering leptonic and hadronic bounds at the same time constrains much further the parameter space of generic DM models, which we study in a model-independent fashion through different classes of effective theories. We include in the analysis additional bounds coming from Direct Detection searches, as well as the requirement of a correct relic abundance. All this results in quite severe exclusion limits, excluding a particular class of effective theories. Finally, we perform a detailed study of possible synchrotron signals coming from DM annihilation at the Galactic Centre, comparing the corresponding bounds with those obtained from other searches, e.g. direct production in colliders (LEP, Tevatron and LHC) and other indirect-detection searches. We study the DM induced synchrotron-signal not only in the effective theory, but also in two particular ultraviolet realisations, which represent the most simple extensions of the SM to account for Dark Matter, obtaining important restrictions on their parameter-spaces.

The thesis is organised as follows. In chapter 2 I expose some introductory elements and motivations of Supersymmetry, the MSSM and the Seesaw mechanism. I also give the basis of the calculation of Lepton-Flavor violation effects and Leptogenesis in this context. In chapter 3 I introduce the Dark Matter subject, describing the first experimental evidences, the theoretical formalism and the present experimental strategies. Finally, the original works and results are presented in chapters 4, 5 and 6, which are a compendium of the main accomplishments of my thesis.

CHAPTER 2

SUPERSYMMETRY AND LEPTON FLAVOUR VIOLATION

2.1 Elements of SUSY

Nowadays, Supersymmetry (SUSY) is an usual ingredient in theories beyond the Standard Model (SM). There are indeed strong theoretical reasons supporting the idea that SUSY is a good symmetry of nature in some region of scales.

Maybe the first motivation about its existence came from the idea of generalising the Poincare symmetry, allowing for transformations that take fermions into bosons and vice-versa. The idea was improved in the context of String Theory, at its early stages. The easiest way to introduce fermions in the original bosonic string was through supersymmetry. From a more phenomenological perspective, a supersymmetric version of the Standard Model presents very attractive properties, as the gauge coupling unification at a high scale (not far from M_P) and the relaxation of the infamous hierarchy problem. The electroweak breaking requires the Higgs mass-term to be $\mathcal{O}(100\text{ GeV})$. However, the quadratic contributions to this mass-term arising from radiative corrections (e.g. from a loop of tops) are much higher if the cut-off is beyond a few TeV. This translates into a strong fine-tuning between the initial tree-level mass and the size of the radiative corrections. SUSY provides an automatic cancellation of the quadratic divergences, and thus an elegant way-out to this problem. Although there may be caveats about the interpretation of the fine-tuning, the hierarchy problem is still commonly accepted by the scientific community as a strong indication that there should exist new physics at $\mathcal{O}$(TeV).

Unfortunately, Supersymmetry has not been observed in experiments, which requires it to be spontaneously broken. The corresponding effective theory at low-scale consists of a supersymmetric Lagrangian plus a bunch of terms which break SUSY in an explicit, but "soft", fashion.

Concerning the supersymmetric Lagrangian, the minimal (N=1) supersymmetric extension of the Standard Model is the so-called Minimal Supersymmetric Standard Model (MSSM). The particle content of the MSSM is given in Table 2.1. It consists of the usual SM spectrum plus a supersymmetric partner of each SM particle. Besides, the Higgs sector has to be extended, including two Higgs doublets, H_u, H_d. This is required [1] to keep the anomaly cancellation (since the fermonic components of the Higgs superfields contribute to the gauge anomalies) and also to provide masses to up- as well as down-type quarks and leptons.

Chiral super-multiplet fields				
Names		spin 0	spin 1/2	$SU(3)_C, SU(2)_L, U(1)_y$
squarks, quarks	Q	$(\tilde{u}_L, \tilde{d}_L)$	(u_L, d_L)	**3**, **2**, 1/3
	$\bar{U}$	$\tilde{\bar{u}}_L = \tilde{u}_R^\dagger$	$\bar{u}_L = (u_R)^c$	$\bar{3}$, **1**, -4/3
	$\bar{D}$	$\tilde{\bar{d}}_L = \tilde{d}_R^\dagger$	$\bar{d}_L = (d_R)^c$	$\bar{3}$, **1**, 2/3
sleptons, leptons	L	$(\tilde{\nu}_{eL}, \tilde{e}_L)$	(ν_{eL}, e_L)	**1**, **2**, -1
	$\bar{E}$	$\tilde{\bar{e}}_L = \tilde{e}_R^\dagger$	$\bar{e}_L = (e_R)^c$	**1**, **1**, 2
Higgs, Higgsinos	H_u	(H_u^+, H_u^0)	$(\tilde{H}_u^+, \tilde{H}_u^0)$	**1**, **2**, 1
	H_d	(H_d^0, H_d^-)	$(\tilde{H}_d^0, \tilde{H}_d^-)$	**1**, **2**, -1
Gauge super-multiplet fields				
		spin 1/2	spin 1	$SU(3)_C, SU(2)_L, U(1)_y$
gluinos, gluons		$\tilde{g}$	g	**8**, **1**, 0
winos, W bosons		$\tilde{W}^\pm, \tilde{W}^0$	$W^\pm, W^0$	**1**, **3**, 0
bino, B boson		$\tilde{B}$	B	**1**, **1**, 0

Table 2.1: *Particle content of the Minimal Supersymmetric Standard Model.*

The superpotential of the MSSM is given by the most general renormalizable holomorphic function of the superfields consistent with all the symmetries of the theory (including some version of $R-$parity to prevent lepton- and baryon-number violation and thus proton decay),

$$W = y_u^{ij} \bar{U}_i Q_j \cdot H_u - y_d^{ij} \bar{D}_i Q_j \cdot H_d - y_e^{ij} \bar{E}_i L_j \cdot H_d + \mu H_u \cdot H_d, \tag{2.1}$$

where the dots denote SU(2)-invariant products of two doublets (colour indices are not shown), the y's are the Yukawa couplings and μ mass-term is an additional supersymmetric parameter. The corresponding supersymmetric Lagrangian can be derived using the standard rules. In particular, this Lagrangian contains the following pieces:

[1] From the more formal point of view, this comes from the need of building a holomorphic superpotential.

- *Yukawa-terms*. These arise from the general expression

$$\frac{1}{2}\sum_{nm}\frac{\partial^2 W(\phi)}{\partial\phi_n\partial\phi_m}\left(\psi_{nL}^T\varepsilon\psi_{mL}\right),$$

  where the superpotential is expressed as a function of just the scalar components of all the superfields, ϕ_n; and ψ_n are the corresponding fermions. This part of the Lagrangian contains the usual SM Yukawa terms plus their supersymmetric counterparts. E.g. from the $u-$type Yukawa one gets

$$y_u\bar{u}Q\cdot H_u + y_u\bar{\tilde{u}}Q\cdot\tilde{H}_u + y_u\bar{u}\tilde{Q}\cdot\tilde{H}_u.$$

- *Scalar potential*. It arises from the general expression

$$V=\sum_n\left|\frac{\partial W(\phi)}{\partial\phi_n}\right|^2 + \left(\sum_{nm}\phi_n^*(t_A)_{nm}\phi_m\right)^2.$$

  This includes terms like

$$|y_u|^2|\tilde{Q}\cdot H_u|^2 + |y_u|^2|\bar{\tilde{u}}\cdot H_u|^2 + |y_u|^2|\bar{\tilde{u}}\tilde{Q}|^2 + |y_u\bar{\tilde{u}}\tilde{Q}+\mu H_d|^2$$

  and similar expressions for down-type quarks and leptons.

- Usual pure-gauge Standard Model interactions coming from the kinetic terms for ϕ and ψ_L plus additional gaugino – gauge-boson – gaugino vertices,

$$\bar{\lambda}_a\gamma^\mu C_{abc}A_{b\mu}\lambda_c$$

  where a,b,c are group-labels of the corresponding adjoint representation and C_{abc} is the group structure-function.

- *Matter-Gaugino interactions*: They have the general structure

$$i\sqrt{2}\sum_{Anm}\left(\bar{\psi}_{nL}(t_a)_{nm}\lambda_a\right)\phi_m + \text{h.c.},$$

  including terms like

$$(\bar{u}T_{SU(3)}\tilde{g})\tilde{u} + (\bar{d}T_{SU(3)}\tilde{g})\tilde{d} + (\bar{u}T_{SU(2)}\tilde{W}^+)\tilde{d} + (\bar{u}T_{SU(2)}\tilde{W}^0)\tilde{u} + (\bar{u}T_{U(1)}\tilde{B}^0)\tilde{u} + \cdots$$

On the other hand, the SUSY soft-breaking Lagrangian is parametrised by the soft terms, namely:

- Gaugino masses for each gauge group:

$$-\frac{1}{2}(M_3\tilde{g}^a\cdot\tilde{g}^a + M_2\tilde{W}^a\cdot\tilde{W}^a + M_1\tilde{B}\cdot\tilde{B} + \text{h.c.}), \tag{2.2}$$

  where M_i are assumed to be real, are all real, so they do not introduce any new CP-violation. However they can be either positive or negative.

- Squark $(\text{mass})^2$ terms:

$$-m^2_{Qij}\tilde{Q}^\dagger_i\cdot\tilde{Q}_j - m^2_{\bar{\tilde{u}}ij}\bar{\tilde{u}}^\dagger_{Li}\bar{\tilde{u}}_{Lj} - m^2_{\bar{\tilde{d}}ij}\bar{\tilde{d}}^\dagger_{Li}\bar{\tilde{d}}_{Lj}; \tag{2.3}$$

- Slepton $(\text{mass})^2$ terms:

$$-m^2_{Lij}\tilde{L}^\dagger_i\cdot\tilde{L}_j - m^2_{\bar{\tilde{e}}ij}\bar{\tilde{e}}^\dagger_{Li}\bar{\tilde{e}}_{Lj}; \tag{2.4}$$

- Higgs $(\text{mass})^2$ terms:

$$-m^2_{H_u}H^\dagger_u\cdot H_u - m^2_{H_d}H^\dagger_d\cdot H_d - (bH_u\cdot H_d + \text{h.c.}) \tag{2.5}$$

  where $H^\dagger_u\cdot H_u = |H^+_u|^2 + |H^0_u|^2$ (and similarly for H_d) and $H_u\cdot H_d = H^+_u H^-_d - H^0_u H^0_d$.

- Trilinear scalar couplings:

$$-a^{ij}_u\bar{\tilde{u}}_{Li}\tilde{Q}_j\cdot H_u + a^{ij}_d\bar{\tilde{d}}_{Li}\tilde{Q}_j\cdot H_d + a^{ij}_e\bar{\tilde{e}}_{Li}\tilde{L}_j\cdot H_d + \text{h.c.} \tag{2.6}$$

Admittedly, the soft terms introduce a huge amount of parameters in the theory. However, extensive regions of the parameter space are in fact excluded phenomenologically. In particular, generic values of most of the new parameters trigger processes of flavour changing neutral currents (FCNC) or CP-violation, at levels that are excluded by experiments. For example, if the matrix $\mathbf{m}^2_{\tilde{L}}$ in (2.4) has a non-suppressed off-diagonal term such as $(m^2_{\tilde{L}})_{e\mu}\tilde{e}^\dagger_L\tilde{\mu}_L$ (in the basis where charged-lepton masses are diagonal), then $\mu\to e+\gamma$ occurs at unacceptable rates. These kinds of restrictions partially justify the assumptions of the popular "constrained MSSM" (CMSSM), which amounts to start with complete universal soft terms at the unification scale (M_X)

$$M_3 = M_2 = M_1 = m_{1/2}; \tag{2.7}$$

$$\mathbf{m}^2_{\tilde{Q}} = \mathbf{m}^2_{\bar{\tilde{u}}} = \mathbf{m}^2_{\bar{\tilde{d}}} = \mathbf{m}^2_{\tilde{L}} = \mathbf{m}^2_{\bar{\tilde{e}}} = m^2_0\mathbf{1}, \tag{2.8}$$

$$m^2_{H_u} = m^2_{H_d} = m^2_0; \tag{2.9}$$

and

$$\mathbf{a}_u = A_0\mathbf{y}_u, \quad \mathbf{a}_d = A_0\mathbf{y}_d, \quad \mathbf{a}_e = A_0\mathbf{y}_e. \tag{2.10}$$

Of course, such full universality is not required to get consistency with the previous phenomenological restrictions, but it is a possibility that can arise in some well-motivated scenarios of SUSY breaking and transmission to the observable sector, e.g. gravity mediation in minimal supergravity or dilation-dominance in string-inspired supergravity.

On the other hand, despite the initial diagonal mass matrices for squarks and leptons, they get off-diagonal entries along the RG evolution from the M_X to the electroweak scale, triggered by the various (flavour-violating) Yukawa couplings.

2.1.1 Neutrino masses and mixings

Assuming neutrinos as Majorana particles, the flavour eigenstates, $|\nu_\alpha\rangle$, can be expressed as linear combinations of the mass eigenstates, $|\nu_i\rangle$

$$|\nu_\alpha\rangle = \sum_{i=1}^{3} U^*_{\alpha i}|\nu_i\rangle \tag{2.11}$$

where U is the unitary matrix (known as the PMNS matrix) that diagonalises the neutrino mass-matrix written in the flavour-basis. U can be parametrized according to the following decomposition:

$$U = V \cdot \mathrm{diag}(e^{i\phi_1}, e^{i\phi_2}, 1), \tag{2.12}$$

where the unitary matrix V has the form

$$V = \begin{pmatrix} c_{13}c_{12} & c_{13}s_{12} & s_{13}e^{-i\delta} \\ -c_{23}s_{12} - s_{23}s_{13}c_{12}e^{i\delta} & c_{23}c_{12} - s_{23}s_{13}s_{12}e^{i\delta} & s_{23}c_{13} \\ s_{23}s_{12} - c_{23}s_{13}c_{12}e^{i\delta} & -s_{23}c_{12} - c_{23}s_{13}s_{12}e^{i\delta} & c_{23}c_{13} \end{pmatrix} . \tag{2.13}$$

with $s_{ij} \equiv \sin\theta_{ij}$, $c_{ij} \equiv \cos\theta_{ij}$. The present experimental ranges for the three mixing angles are

$$\sin^2(2\theta_{12}) = 0.857 \pm 0.024, \quad \sin^2(2\theta_{23}) > 0.95, \quad \sin^2(2\theta_{13}) = 0.098 \pm 0.013 \tag{2.14}$$

Concerning the mass eigenvalues, the experiments of neutrino oscillations provide precise information on two squared-mass differences. Denoting m_3 the most split mass-eigenvalue, these are given by

$$\begin{aligned} |m_2^2 - m_1^2| &= (7.50 \pm 0.20) \times 10^{-5}\ \mathrm{eV}^2 \\ |m_3^2 - m_2^2| &= (2.32^{+0.12}_{-0.08}) \times 10^{-3}\ \mathrm{eV}^2 \end{aligned} \tag{2.15}$$

The absolute scale of the neutrino masses is not known, though we have several upper bounds coming from from tritium beta-decay, neutrino less double beta-decay and cosmological (CMB) limits. Roughly speaking, the heaviest neutrino should be at most ~ 0.3 eV. This allows for two kinds of neutrino mass- hierarchy: $m_3 > m_1, m_2$ ("normal hierarchy") or $m_3 < m_1, m_2$ ("inverted hierarchy").

The remarkable smallness of the neutrino masses cries out for a theoretical explanation. In this sense, the Seesaw mechanism has probably became the most popular one. Next we describe the Seesaw framework in the supersymmetric context.

2.1.2 Supersymmetric See-saw

The Seesaw mechanism is based on the assumption that the neutrinos have standard Yukawa-like interactions, which requires to introduce one right-handed neutrino per family, *plus* a

Majorana mass terms for the latter. These are described by the following extended superpotential

$$W = W_0 - \frac{1}{2}(\nu_R^c)^T \mathcal{M} \nu_R^c + (\nu_R^c)^T Y_\nu L \cdot H_2, \tag{2.16}$$

where W_0 is the superpotential (2.1), and $\mathcal{M}$ is a 3×3 matrix accounting for the masses of the right-handed neutrinos[2]. The diagonalization of the full 6×6 neutrino mass-matrix gives two mass eigenstates (per generation), one with masses of order $\frac{Y_\nu^2 v^2}{M} \ll v$, and the other with mass of order[3] M. Since the right-handed Majorana mass-matrix does not have electroweak origin, it can in principle take arbitrary large values, which translates in very suppressed masses for the light ($\sim$ left-handed) neutrinos.

Alternatively, one can integrate-out the right-handed neutrinos, thus obtaining the effective Lagrangian with the mass term for the three light left-handed neutrinos. Let us now sketch this calculation

The effective generating functional Z_{eff} is defined in this case according to the following expression:

$$e^{iZ_{\text{eff}}} \equiv \frac{\int [dN_R^c]^2 \exp\left(i\int d^4x \mathcal{L}(N_R^c(x),\phi_i(x))\right)}{\int [dN_R^c]^2 \exp\left(i\int d^4x \mathcal{L}(N_R^c(x),0)\right)} \tag{2.17}$$

where N_R^c are the basis of right-handed neutrinos where $\mathcal{M}$ is diagonal, and $\mathcal{L}(N_R^c(x),\phi_i(x))$ is the Lagrangian obtained from the superpotential (2.16). So the procedure is now to complete the square, which can be done by the following rearrangement:

$$\begin{aligned}
\int d^4x\, \mathcal{L} &= \int d^4x \left[-\frac{1}{2}(N_R^c)^T \mathcal{D} N_R^c + \frac{1}{2}\left((N_R^c)^T Y_\nu L\cdot H_2 + \text{h.c.}\right)\right] \\
&= \int d^4x \left[N_R^c - \mathcal{D}^{-1}(Y_\nu L\cdot H_2)\right]^T \mathcal{D}\left[N_R^c - \mathcal{D}^{-1}(Y_\nu L\cdot H_2)\right] \\
&- \int d^4x (Y_\nu L\cdot H_2)^T \mathcal{D}^{-1}(Y_\nu L\cdot H_2)
\end{aligned} \tag{2.18}$$

where $\mathcal{D} \equiv \partial\!\!\!/_x + \mathcal{M}$, and $\mathcal{D}^{-1} = \Delta_F(x-y)$, with

$$(\partial\!\!\!/_x + \mathcal{M})\Delta_F(x-y) = -\delta^{(4)}(x-y).$$

Now, redefining a new heavy field as

$$N_R^{\prime c} \equiv N_R^c - \mathcal{D}^{-1}(Y_\nu L\cdot H_2)$$

[2] If one imposes conservation of lepton number, this Majorana term is forbidden, but since lepton number is a global symmetry (which is accidentally conserved in the pure SM) there is no reason why it should be respected.

[3] This is an estimation for the case of 1-generation, where M is the mass of the unique right-handed neutrino.

we see that $\int [dN_R^c]^2 = \int [dN_R^{'c}]^2$; thus

$$\begin{aligned} e^{iZ_{\rm eff}} &= \frac{\int [dN_R^{'c}]^2 \exp\left[i\int d^4x \left(-\frac{1}{2}(N_R^{'c})^T \mathcal{D} N_R^{'c} + \frac{1}{2}(Y_\nu L\cdot H_2)^T \mathcal{D}^{-1}(Y_\nu L\cdot H_2)\right)\right]}{\int [dN_R^{'c}]^2 \exp\left[i\int d^4x \left(-\frac{1}{2}(N_R^{c})^T \mathcal{D} N_R^{c}\right)\right]} \\ &= \exp\left(\frac{i}{2}\int d^4x (Y_\nu L\cdot H_2)^T \mathcal{D}^{-1}(Y_\nu L\cdot H_2)\right) \\ &= \exp\left(\frac{i}{2}\int d^4y d^4x (Y_\nu(x)L(x)\cdot H_2(x))^T \Delta_F(x-y)(Y_\nu(y)L(y)\cdot H_2(y))\right). \end{aligned} \tag{2.19}$$

Finally one may obtain a local Lagrangian by noting that the heavy particle propagator is peaked at small distances. So for $J(x) \equiv Y_\nu(x)L(x)\cdot H_2(x)$ we can Taylor expand

$$J(y) = J(x) + (y-x)^\mu [\partial_\mu J(y)]_{y=x} + ...$$

and keep to a good approximation the leading term. Also we can write the propagator as

$$\int d^4y \Delta_F(x-y) = -\int d^4y d^4p \frac{e^{-ip\cdot(x-y)}}{p+\mathcal{M}} = -\int d^4y d^4p \frac{e^{-ip\cdot(x-y)}}{\mathcal{M}(1+p/\mathcal{M})}$$

so for small momenta compared to the scales in $\mathcal{M}$ one has

$$\int d^4y \Delta_F(x-y) \approx -\frac{1}{\mathcal{M}} \tag{2.20}$$

giving the result

$$Z_{\rm eff} = \frac{1}{2}\int d^4x (Y_\nu L\cdot H_2)^T \mathcal{M}^{-1}(Y_\nu L\cdot H_2) \tag{2.21}$$

The relation (2.21) is simply the Weinberg, dim=5 operator, which accounts for the light neutrino masses. Once the scalar Higgses of the MSSM acquire vevs, we have:

$$\mathcal{M}_\nu = Y_\nu^T \mathcal{M}^{-1} Y_\nu \langle H_2^0\rangle^2 . \tag{2.22}$$

2.1.3 LFV processes in the supersymmetric See-saw

The mixing in the neutrino sector leads, in analogy with the Kobayashi-Maskawa effect for quarks, to processes for which the lepton flavour is violated (LFV processes). In the context of the SM those processes are strongly suppressed due to the tiny mass of the neutrinos. However, in the supersymmetric case, even starting with universal conditions at M_X, the non-diagonal neutrino mass matrices contribute along the RG running to the appearance of off-diagonal entries in the slepton mass matrices; which triggers LFV processes. Let us focus

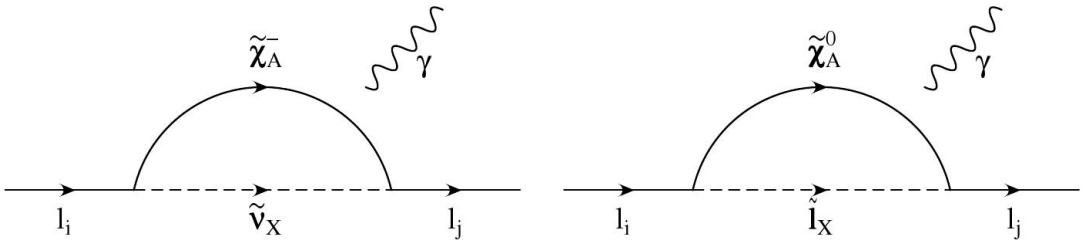

Figure 2.1: Feynman diagrams which give rise to $l_i \to l_j\gamma$. $\tilde{\nu}_X$ and $\tilde{l}_X$ represent the mass eigenstates of sneutrinos and charges sleptons, and $\tilde{\chi}^-$, $\tilde{\chi}^0$ the charginos and neutralinos. (Taken from "Oscillating neutrinos and $\mu \to e,\gamma$". J.A. Casas and A. Ibarra. Nucl.Phys. B618 (2001) 171-204).

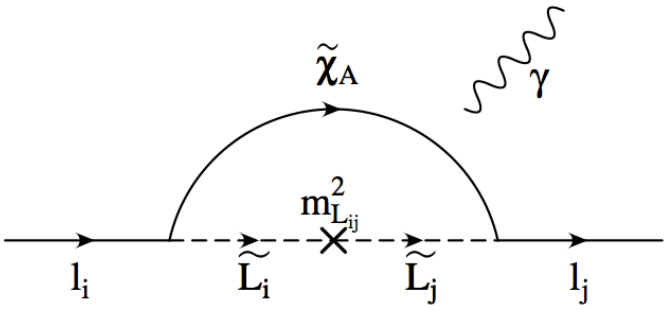

Figure 2.2: Dominant diagram in the process $l_i \to l_j\gamma$, in the mass-insertion approximation. $\tilde{L}_i$ are the slepton doublets in the basis where the gauge interactions and the charged-lepton Yukawa couplings are flavour-diagonal. (Taken from "Oscillating neutrinos and $\mu \to e,\gamma$". J.A. Casas and A. Ibarra. Nucl.Phys. B618 (2001) 171-204).

on the most popular ones, namely $l_i \to l_j\gamma$ processes ($i \neq j$ are family indices). At 1-loop level, the relevant diagrams are shown in Figure 2.1.

The expression for the amplitude of the process, in terms of effective vertices is given by:

$$T = e\varepsilon^{\alpha *}\bar{u}_i(p-q)\left[q^2\gamma_\alpha(A^1_L P_L + A^1_R P_R) + m_{lj} i\sigma_{\alpha\beta}q^\beta(A^2_L P_L + A^2_R P_R)\right]u_j(p) \qquad (2.23)$$

where e is the charge of the electron and muon; ε^α is the polarisation vector of the photon; $u_i(p)$ is the wave-function of a spinor i with momentum p; q is the momentum of the photon; $P_{L,R}$ are the usual helicity projectors, and

$$A_{L,R} = A^{(n)}_{L,R} + A^{(c)}_{L,R} \qquad (2.24)$$

are the amplitudes of the processes. If the emitted photon is on-shell[4], then the first term

[4]The photon can be virtual in other types of processes, e.g. $\mu - e$ conversion, where the emitted photon interacts with the recoiling nucleus.

on the RHS of (2.23) gives no contribution to the effective amplitude and so only the A_2 coefficients in eq. (2.23) are relevant. Hence we drop the super-index "2" in what follows. The super-indices (n) and (c) label neutralino or chargino contributions, respectively. The L(left) or R(right) labels are associated to the chirality of the interacting fermions. Now, in the chargino-neutralino basis, the $A-$amplitudes read:

$$\begin{aligned} A_L^{(n)} &= \frac{1}{32\pi^2}\frac{1}{m^2_{\tilde{l}_x}}\left[N^{L(l)}_{iAx}N^{L(l)*}_{jAx}\frac{1}{6(1-X_{Ax})^4}\right. \\ &\times \quad (1-6X_{Ax}+3X^2_{Ax}+2X^3_{Ax}-6X^2_{Ax}\ln X_{Ax}) \\ &+ \quad \left. N^{L(l)}_{iAx}N^{R(l)*}_{jAx}\frac{M_{\tilde{\chi}^0_A}}{m_{lj}}\frac{1}{(1-X_{Ax})^3}(1-X^2_{Ax}+2X_{Ax}\ln X_{Ax})\right] \end{aligned} \tag{2.25}$$

$$\begin{aligned} A_L^{(c)} &= -\frac{1}{32\pi^2}\frac{1}{m^2_{\tilde{\nu}_x}}\left[C^{L(l)}_{iAx}C^{L(l)*}_{jAx}\frac{1}{6(1-X_{Ax})^4}\right. \\ &\times \quad (2+3X_{Ax}-6X^2_{Ax}+X^3_{Ax}+6X_{Ax}\ln X_{Ax}) \\ &+ \quad \left. C^{L(l)}_{iAx}C^{R(l)*}_{jAx}\frac{M_{\tilde{\chi}^-_A}}{m_{lj}}\frac{1}{(1-X_{Ax})^3}(-3+4X_{Ax}-X^2_{Ax}-2\ln X_{Ax})\right] \end{aligned} \tag{2.26}$$

$$A_R^{(n)} = A_L^{(n)}\Big|_{L\leftrightarrow R} \tag{2.27}$$

$$A_R^{(c)} = A_L^{(c)}\Big|_{L\leftrightarrow R} \tag{2.28}$$

where $X_{Ax} \equiv M^2_{\tilde{\chi}^0_A}/m^2_{\tilde{l}_x}$ (with A labelling the gaugino, and x labelling the slepton), and the **C**, **N** matrices are defined as:

$$C^R_{iAx} = -g_2(O_R)_{A1}U^{\nu}_{X,i}, \quad C^L_{iAx} = g_2\frac{m_{l_i}}{\sqrt{2}m_W\cos\beta}(O_L)_{A2}U^{\nu}_{X,i}\,, \tag{2.29}$$

with $A = 1,2$ and $X = 1,2,3$; and

$$N^R_{iAx} = -\frac{g_2}{\sqrt{2}}\{[-(O_N)_{A2}-(O_N)_{A1}\tan\theta_W]U^l_{X,i}+\frac{m_{l_i}}{m_W\cos\beta}(O_N)_{A3}U^l_{X,i+3}\}\,, \tag{2.30}$$

$$N^L_{iAx} = -\frac{g_2}{\sqrt{2}}\{\frac{m_{l_i}}{m_W\cos\beta}(O_N)_{A3}U^l_{X,i}+2(O_N)_{A1}\tan\theta_W U^l_{X,i+3}\} \tag{2.31}$$

with $A = 1..4$ and $X = 1..6$. The matrices $O_{R,L}$ (O_N) are the ones that diagonalise the chargino (neutralino) mass matrix. The matrices U^{ν} and U^l are the ones diagonalising the sneutrinos and charged sleptons, respectively.

In the previous expressions, the flavour-violating sources are in the non-diagonal structure of the **C**, **B** matrices, which in turn comes from the off-diagonal entries in the slepton mass matrices generated along the RG running. A more intuitive way to see that is to evaluate the previous diagrams in the mass-insertion approximation, as shown in Fig. 2.2. Then it is clear that they are proportional to $(m^2_{\tilde{l}})_{ij}$. The dominant contribution to these off-diagonal entries is usually due to the neutrino-Yukawa interactions (unless the scale of the right-handed Majorana masses is much below M_X) and has the form

$$(m^2_{\tilde{l}})_{ij} \supset -\frac{1}{8\pi^2}(3m_0^2+A_0^2)\left[(Y_\nu^\dagger)_{ik}\ln\left(\frac{M_X}{M_k}\right)\delta_{kl}(Y_\nu)_{lj}\right] \tag{2.32}$$

where M_k is the mass of the k-th right-handed neutrino ($k = 1...3$).

2.2 Leptogenesis

Observations indicate that the number of baryons present in the universe is unequal to the number of anti-baryons. Indeed the stars, galaxies and clusters consist essentially of matter and there is no antimatter. There are good reasons to believe that this asymmetry has been generated dynamically instead of being caused by an asymmetry in the initial conditions; the most important being maybe the one related to inflation, which is nowadays quite accepted by the community. In this scheme, any primordial baryon asymmetry would have been exponentially diluted away by inflation.

The ingredients that have to be present in order for a dynamical asymmetry to be generated are called the Sakharov conditions: 1) There has to be a baryon number (B) violation. This condition is required in order to evolve from an initial state with $\Delta B = 0$ to a state $\Delta B \neq 0$. 2) C and CP violation, because otherwise the processes creating baryons would have the same rate as those creating anti-baryons. And 3) departure from equilibrium, since in chemical equilibrium the inverse processes would erase the asymmetries generated. Actually the Standard Model have all the ingredients present but it fails in explaining an asymmetry as large as the one observed.

The observed baryon asymmetry is:

$$\eta_B \equiv \left.\frac{n_B - n_{\bar{B}}}{n_\gamma}\right|_0 = (6.19 \pm 0.15)\times 10^{-10}\,, \tag{2.33}$$

where $n_B, n_{\bar{B}}$ is the number density of baryons and anti-baryons, respectively, and n_γ is the number density of photons. The subscript 0 denotes values at present time. There are different ways to infer the previous value of η_B. One of them is using Big Bang Nucleosynthesis (BBN) predictions. It turns out that the primordial abundances of the light elements (D, ^{3}He, ^{4}He, and ^{7}Li) are strongly dependent on η_B, but most surprisingly, there is a range of η_B values which is consistent with all four abundances, and it is in total agreement with (2.33).

The second method takes into account the Cosmic Microwave Background (CMB) radiation, whose main features can be described as "acoustic" waves of the photon-baryon fluid. The observed spectrum strongly depends on the baryon number density n_B and thus on the asymmetry η_B. It is impressive that the requirement on n_B coming from CMB is perfectly in agreement with that coming from BBN.

Leptogenesis comes as one of the alternatives of New Physics for the generation of the baryon asymmetry. In this framework, the asymmetry is first generated in the lepton sector. For example, in the Seesaw mechanism, the Yukawa interaction of the neutrinos provide the necessary source of CP violation. The rate of those interactions can be slow enough in order not to reach the equilibrium with the thermal bath. Lepton number violation comes directly from the RH Majorana mass term in the Lagrangian. Finally, the Standard Model sphaleron processes play a crucial role in partially converting the lepton asymmetry into a baryon asymmetry. Thus, in the context of Seesaw, leptogenesis is qualitatively unavoidable, and the question of whether or not it can successfully explain the baryon asymmetry is a quantitative one.

We consider leptogenesis via the decays of N_1, which is the lightest RH neutrino. When the decay is into a single flavour α, $N_1 \to L_\alpha \phi$ or $\bar{L}_\alpha \phi^\dagger$, one can write [5]

$$Y_{\Delta B} = \frac{n_B - n_{\bar{B}}}{s} \simeq \frac{135\zeta(3)}{4\pi^4 g_\star} \times C_{\text{sphal}} \times \eta \times \varepsilon \,, \tag{2.34}$$

where s is the entropy density. Here $g_\star$ is the number of degrees of freedom of the theory. The other factors in this equation deserve a more detailed explanation.

The quantity ε is the CP asymmetry factor, which is defined as

$$\varepsilon \equiv \frac{\Gamma(N_1 \to \phi L) - \Gamma(N_1 \to \phi^\dagger \bar{L})}{\Gamma(N_1 \to \phi L) + \Gamma(N_1 \to \phi^\dagger \bar{L})} \,. \tag{2.35}$$

It is straightforward to see that $\varepsilon = 0$ if the above rates are computed at tree-level. However the interference between the tree-level and the 1-loop contributions induces a non-vanishing ε. More precisely, if we consider the amplitude $\mathcal{M} = c_0\mathcal{A}_0 + c_1\mathcal{A}_1$, where $c_i, \mathcal{A}_i$ are the coefficients and amplitudes of the tree-level and 1-loop processes, respectively, ε is given by:

$$\varepsilon = \frac{\text{Im}(c_0 c_1^*) 2 \int \text{Im}(\mathcal{A}_0 \mathcal{A}_1^*) \tilde{\delta} d\Pi_{L,\phi}}{|c_0|^2 \int |\mathcal{A}_0|^2 \tilde{\delta} d\Pi_{L,\phi}} \tag{2.36}$$

where

$$\tilde{\delta} = (2\pi)^4 \delta^{(4)}(P_i - P_f), \quad d\Pi_{L,\phi} = \frac{d^3 p_L}{2E_L(2\pi)^3} \frac{d^3 p_\phi}{2E_\phi(2\pi)^3}$$

and P_i, P_f are, respectively, the incoming 4-momentum (i.e. P_{N_1}) and the outgoing 4-momentum (i.e. $P_\phi + P_L$). Notice that ε is directly dependent on the imaginary parts of the amplitudes,

[5] For more details see section 3.4.1

encoding the CP violation. For the Seesaw model the result is:

$$\varepsilon = \frac{1}{8\pi}\frac{\sum_{j=2,3}\mathrm{Im}\{[(YY^\dagger)_{1j}]^2\}g(x_j)}{8\pi(YY^\dagger)_{11}} \tag{2.37}$$

where Y is the neutrino Yukawa matrix and $x_j \equiv M_j^2/M_1^2$. The $g(x)$ function, within the MSSM, is

$$g(x) = \sqrt{x}\left[\frac{2}{1-x} - \log\left(\frac{1+x}{x}\right)\right]$$

Coming back to eq.(2.34), the quantity η parametrises the out-of-equilibrium dynamics, and is called the efficiency factor. Indeed, if the processes are almost in thermal equilibrium, inverse processes can probably washout the asymmetries generated by the N_1 decays, thus making the asymmetry generation less efficient. A simple criterion[6] for evaluating if a process thermalises with the particles of the thermal bath, is to compare its reaction rate Γ with the expansion rate of the universe, H. In this way, processes for which $\Gamma > H$ occur more rapidly than the expansion rate of the universe and those thermalise. In the same way, if $\Gamma < H$ those process do not reach thermal equilibrium. However, in general, one needs to solve the full relevant Boltzmann equations in order to check if a process actually thermalises or not.

The efficiency factor η comes from the solution of the Boltzmann equations for the number density of the lightest RH neutrino, n_{N_1}, and the $B-L$ asymmetry, n_{B-L}, in such a way that in the limit of an initial thermal abundance of N_1 and no washout, it tends to unity. It actually smoothly interpolates between two regimes: the strong washout regime, in which the reaction rate of the N_1 decay, Γ_D, is larger than H, and thus the inverse decay strongly erases the asymmetry; and the weak washout regime, where $\Gamma_D < H$, and the inverse processes are not efficient enough to affect the asymmetry generated by the direct ones. In the weak washout regime the final asymmetry in general depends on the initial conditions.

The two main quantities involved in the computation of η are precisely related to Γ and H:

$$\tilde{m} \equiv \frac{8\pi v^2}{M_1^2}\Gamma_D = \frac{(YY^\dagger)_{11}v^2}{M_1}, \quad m_\star \equiv \frac{8\pi v^2}{M_1^2}H(T=M_1) \simeq 10^{-3}\mathrm{eV}\ . \tag{2.38}$$

In terms of these, the η parameter can be expressed as:

$$\eta = \left[\left(\frac{2\tilde{m}}{m_\star}\right)^{1.16} + \frac{2m_\star}{\tilde{m}}\right]^{-1} \tag{2.39}$$

Finally, the C_{sphal} term in (2.34) has to do with the conversion of part of the L generated by the leptogenesis, into B by means of Standard Model sphalerons, which render $B+L$ to zero, while preserving the total $B-L$.

[6] I will elaborate much more around this in the next chapter, dedicated to Dark Matter.

CHAPTER 3

DARK MATTER PHENOMENOLOGY

The starting point of the subject goes back to 1933. In that year, the Swiss astrophysicist Fritz Zwicky discovered a mismatch between luminous and gravitational masses of the Coma galaxy cluster, and called this extra content "dark matter" (DM). Today, 80 years after that discovery, DM is still evading detection, although at present the new generation of experiments could make us feel that the discoveries are closer than ever.

In the second part of this thesis, I deal with the phenomenology of DM, focusing on the implications of colliders data, as well as on the study of sub-products of DM annihilation in our Galaxy. In my works I attempted to contribute to the complementarity between these two approaches in constraining DM properties.

This chapter is organised as follows. In section 1 I comment about well stablished experimental evidences of missing mass in the universe. Section 2 is devoted to the DM candidates of different nature that have been considered. In section 3, I deal with the dynamics and thermodynamics of the early universe. Section 4 is devoted to the Boltzmann formalism which is necessary to study the evolution of DM abundance. Finally, in section 5, I present the main experiments covering the different strategies to search for DM candidates.

3.1 Experimental evidences of Dark Matter

After Zwicky's discovery, there were almost 40 years where the scientific community basically ignored the "missing mass problem". However in the early 70's Vera Cooper Rubin measured the velocity curves of edge-on spiral galaxies to an unprecedented accuracy. She demonstrated that most stars in spiral galaxies orbit the centre at roughly the same speed. This was consistent with an embedding of the spiral galaxies in a much larger halo of invisible mass.

Different methods have been used to estimate the matter density of the universe. One

of the oldest is the so-called mass-to-light (M/L) ratios. Using the second Newton's Law, one can estimate the rotation velocity v_l of a luminous mass $M_l(r)$ contained in a radius r, by computing $M_l(r)$ as a function of the mass density which is extracted from line-of-sight radial luminosity distribution. This velocity $v_l = \sqrt{GM_l(r)/r}$ is then compared with actual observations of the kinematics of stars at different radii, i.e. the rotation curves. In the absence of non-luminous matter, the theoretical prediction should coincide with the observed rotation curves. However, it has been demonstrated that galaxies, clusters of galaxies and super-clusters have a significant fraction of this missing component.

Starting from small scales (stellar sizes, say) the observations show a linear increase of M/L ratio with R. However, as more large-scale measurements are considered, that initial linearity disappears, and beyond $R \approx 1$ Mpc the M/L ratios approach to a plateau, consistent with a total matter density $\Omega_m h^2 \approx 0.3$.

There are other methods which independently probe and quantify the presence of dark matter in the universe. One of them is the so-called "gravitational lensing" effect. This effect is a direct consequence of General Relativity, where the trajectory of photons is affected by the curvature of space-time induced by the presence of massive objects. As a consequence, light rays leaving a source in different directions are sometimes focused on the same spot (the observer here on Earth) by an intermediate galaxy or cluster producing multiple distorted images of the source.

A third method is based on the measurement of the baryons-to-matter ratio, defined by $f_b \equiv \Omega_b/\Omega_m$. Assuming that the luminous (baryonic) matter is measured, then the aim is to measure independently the ratio f_b. It has been demonstrated that the visible matter in galaxies largely resides in hot ionised gas, with only a small fraction in stars. This means that baryon-to-matter is well approximated by the gas-to-matter ratio, which can be measured via: a) X-ray spectrum; by measuring the mean gas temperature from the overall shape of the X-ray spectrum, and the absolute value of the gas density from the X-ray luminosity; and b) the Sunyaev-Zeldovich effect; by which the CMB photons can Inverse-Compton scatter off the hot electrons of the gas, lowering down the intensity of CMB radiation as compared to the unscattered CMB.

These independent methods, among others, provide compelling evidence that the baryon density is of order 5% of the critical density, while the total matter density is about five times larger. This clearly states that most of the matter in the universe is in the form of a non-luminous, "dark" matter.

3.2 Dark Matter candidates

3.2.1 Baryonic Dark Matter?

One possibility which is nowadays disfavoured by experiments, is the so called MACHOs (from MAssive Compact Halo Objects), which are purely baryonic objects, however very

difficult to detect.

Indeed, our ability to observe stars has its limitations, because below some level of luminosity we can not detect anything. It turns out that the total mass density due to stars is well approximated by $\rho_s \approx m_c^{-0.35}/0.35$, where m_c is the lowest observable stellar mass. It means that the reduction of the lowest threshold of detectable stellar mass by a factor of 2 results in an increase of the stellar mass density of a factor 3.6 .

Brown dwarfs are an example of a MACHO. Stars are born from self-gravitating clouds of gas. Gravitational collapse of this gas will cause the temperature to rise until nuclear burning can begin, after which the star is born. However, it can happen that before the temperature rises up to this point, the *electron degeneracy* prevents the collapse to continue. Electron degeneracy is a consequence of the Pauli exclusion principle, and causes the electrons in dense matter to be in a state of continuous motion, increasing the pressure of the gas. This happens for objects whose mass is order $0.08M_\odot$ or smaller.

White dwarfs are more popular. They form from the collapse of the stellar core once the nuclear burning ceased. Their mass is typically smaller than $1.4M_\odot$, and their death as a star is followed by a helium flash which blows off the outer parts of the star, thus creating a planetary nebula. However the core continues in its own gravitational collapse until electron degeneracy is reached. They gradually cool down, becoming frequently difficult to observe due to its low luminosity (typically 10^{-3} to 10^{-4} of the Sun's one).

Neutron stars are another example of a MACHO. They are the created after the gravitational collapse of a supernova, remaining afterwards typical masses in the range $1.4M_\odot \lesssim M \lesssim 2M_\odot$. In this case, the collapse of the dead star is stronger and electrons and protons can get sufficiently closely packed that neutrons are formed. Then, the collapse continues until neutron degeneracy is reached. This objects can have typical sizes of 30 km diameter. Finally, if the star's mass is larger than $2M_\odot$, the gravitational collapse is so strong that the radius of the objects shrinks under the Schwarzschild radius, thus becoming a black hole.

All of these are compact sub-stellar objects that can not be directly observed, thus being a form of "dark matter". However, even with their contributions added to the visible matter, the total matter content of the universe is significantly short.

In summary, all the above points to the presence of a non-baryonic dark matter.

3.2.2 Non-baryonic Dark Matter

The strongest hint about the non-baryonic nature of DM comes from Big Bang Nucleosynthesis (BBN). Indeed, having extra baryonic matter would spoil the success of BBN predictions. Thus, particles not affecting BBN have to be either very rare or very weakly coupled (WIMPs). Dark Matter can be classified according to its kinetic energy at the decoupling time:

Hot Dark Matter (HDM). The Standard Model's candidate for DM, the neutrino, enters into this category. When the temperature in the universe was about 1 MeV, the rate

of interactions such as $\nu e \leftrightarrow \nu e$, which keep neutrinos coupled to the rest of the plasma, dropped below the rate of the expansion of the universe. Therefore, the neutrinos were relativistic by then (thus they are "hot"). These velocities were larger at high redshifts, which resulted in major effects on the development of self-gravitating structures. In this case, the structure formation occurs with larger super-clusters forming first in flat sheets and subsequently fragmenting into smaller pieces to form clusters, galaxies and stars. The predictions of HDM model strongly disagree with observations.

Cold Dark Matter (CDM). Most of the DM candidates coming from theories BSM fall into this category. Popular examples are neutralinos, coming from SUSY theories, sterile heavy neutrinos, and extra scalars coming from theories with minimal extra content. Most of WIMP models lie also in this option. Cosmological observations strongly favour this option, as it implies a bottom-up structure formation, from smaller structures forming first (stars, galaxies) to the large-scale structures that with observe today. However, there are two important discrepancies between predictions of the CDM model and observation of galaxies and their clustering: a) the cuspy halo problem (CDM predicts the central density slopes of galaxies to be much steeper than the observed ones); and b) the missing satellites problem (CDM simulations predict an excess in the number of small dwarf galaxies, those having about 1/1000 of the Milky Way mass).

Warm Dark Matter (WDM). This model interpolates between HDM and CDM, and examples of these can be sterile neutrinos which are not so heavy, and gravitinos. However if the gravitino is not very heavy (order TeV or less), it can lead to the so-called *gravitino problem*. In the gravitino case, if it is stable, then its density turns out to be much larger than the DM density observed. If it is unstable, since its interactions are only gravitational, the decay rate is very suppressed, and its life-time is much larger than the era of BBN, thus its decay products (photons, hadrons) can have disastrous effect on BBN predictions.

3.3 Early universe

In this section I briefly describe the dynamics in the early universe, from the time when inflation is over. At the end of the day the relic density of a Dark Matter particle will be derived from the Boltzmann equation.

3.3.1 The dynamics of the universe's evolution

The evolution of the universe as a whole can be studied taking into account only its gravitational interactions.

Let us consider the Einstein equation:

$$R_{\alpha\beta} - \frac{1}{2} g_{\alpha\beta} R = 8\pi G T_{\alpha\beta} \ , \tag{3.1}$$

where $R_{\alpha\beta}$ is the Riemman tensor, R stands for the scalar curvature and $T_{\alpha\beta}$ is the energy-momentum tensor. Two particular useful forms of the latter are the so-called dust approximation:

$$T_{\alpha\beta} = \rho u_\alpha u_\beta \ , \tag{3.2}$$

and the perfect fluid approximation:

$$T_{\alpha\beta} = (\rho + P) u_\alpha u_\beta + P g_{\alpha\beta} \ , \tag{3.3}$$

where ρ is the energy density, P the pressure, and $u_\alpha \equiv \dot{x}_\alpha$. Dust approximation provides a good description of a matter-dominated universe, whereas the perfect fluid approximation is good when dealing with the radiation-dominated era.

When solving (3.1) in the perfect fluid approximation[1], we arrive to the set of Friedmann equations

$$\dot{a}^2 + k = \frac{8\pi G}{3}\rho a^2, \quad \dot{\rho} + 3(\rho + P)H = 0, \quad P = P(\rho) \ , \tag{3.4}$$

where a is the scale factor in the Friedman-Lemaitre-Robertson-Walker (FLRW) metric tensor, $k = +1, 0, -1$ for a positive, flat or negative curvature of the universe, respectively; and H stands for the Hubble parameter $H \equiv \dot{a}/a$.

The solution of the 2nd Friedmann equation shows how the density scales with the radius a:

a) In matter domination, $P = 0$ and

$$\begin{aligned} \dot{\rho} + 3\rho\frac{\dot{a}}{a} = 0 \quad &\Rightarrow \quad \frac{d}{dt}(\rho a^3) = 0 \\ \rho \quad &\propto \quad a^{-3} \end{aligned} \tag{3.5}$$

b) In radiation domination, $P = \frac{1}{3}\rho$ and

$$\begin{aligned} \dot{\rho} + 4\rho\frac{\dot{a}}{a} = 0 \quad &\Rightarrow \quad \frac{d}{dt}(\rho a^4) = 0 \\ \rho \quad &\propto \quad a^{-4} \end{aligned} \tag{3.6}$$

Then, knowing $\rho = \rho(a)$, we can solve the 1st Friedmann equation to see the evolution of the scale factor $a(t)$, in a flat, closed or open universe. The result is represented in fig. 3.1.

On the other hand, the 1st Friedmann equation can be rewritten as:

$$\frac{k}{a^2 H^2} \quad = \quad \frac{8\pi G}{3H^2}\rho - 1 \equiv \frac{\rho}{\rho_c} - 1 \equiv \Omega - 1 \ , \tag{3.7}$$

[1] Note that the dust approximation is the pressure-less limit of the perfect fluid one.

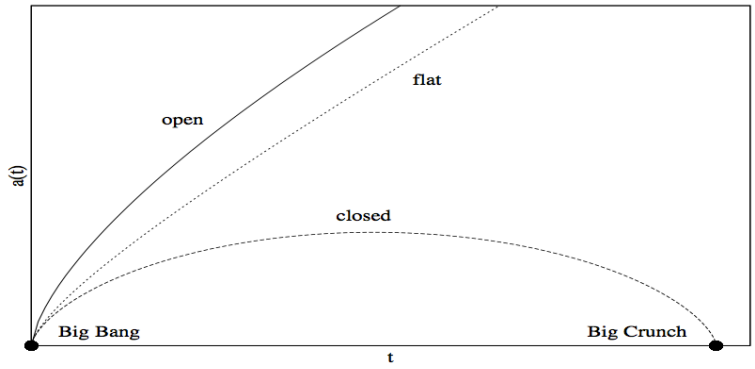

Figure 3.1: Evolution of the scale factor $a(t)$ for different geometries of the universe. (Taken from "Course on Astrophysics". Balsa Terzic. PHYS 652 -2008).

where we have defined the critical energy-density $\rho_c \equiv 3H^2/(8\pi G)$. The density ratio $\Omega = \Omega_m + \Omega_r + \Omega_\Lambda$ is composed by matter, radiation and dark-energy[2]. In terms of how the different energy densities scale with a, and considering[3]

$$\frac{\rho_i}{\rho_i^{(0)}} = \left(\frac{a_0}{a}\right)^n \Rightarrow \rho_i = \rho_c^{(0)}\Omega_i^{(0)}\left(\frac{a_0}{a}\right)^n = \frac{3H_0^2}{8\pi G}\Omega_i^{(0)}\left(\frac{a_0}{a}\right)^n$$

we have

$$H^2 = H_0^2\left[\frac{\Omega_r^{(0)}}{a^4} + \frac{\Omega_m^{(0)}}{a^3} + \frac{\Omega_k^{(0)}}{a^2} + \Omega_\Lambda^{(0)}\right] \tag{3.8}$$

where we have normalised the scale factor today $a_0 = 1$, and $\Omega_k \equiv -k/a^2H^2$.

Age of the universe

From eq.(3.8) we can estimate the age of the universe. Considering that it is flat (k consistent with zero) we have

$$t_0 = \frac{1}{H_0}\int_0^1 da\left[\frac{\Omega_r^{(0)}}{a^2} + \frac{\Omega_m^{(0)}}{a} + a^2\Omega_\Lambda^{(0)}\right]^{-1/2}. \tag{3.9}$$

Solving (3.9) numerically and considering that today, according to observations, we have $\Omega_r^{(0)} \approx 0, \Omega_m^{(0)} \approx 0.27, \Omega_\Lambda^{(0)} \approx 0.73$, $H_0 \approx 0.71$ km/s/Mpc, we can estimate the value of $t_0 \approx 4\times10^{17}s \approx 13\times10^9$ years.

Matter-radiation equality. Since we know how the energy density of radiation ρ_r behaves, we can compare it to the energy density of matter ρ_m in order to know when both

[2] After including the cosmological constant Λ in the Einstein equation (3.1).

[3] The subindex i corresponds to matter, radiation or dark-energy, and $n = 3,4,0$ for matter, radiation and dark-energy cases, respectively. a_0 and H_0 are the scale factor and Hubble parameter today, as well as $\rho^{(0)}$ and $\Omega^{(0)}$ refer to the values today.

components in the universe were comparable. We know that $\rho_r/\rho_m \propto a_0/a = 1+z$, where a_0 is the scale factor today. Thus we can write

$$\frac{\rho_r}{\rho_m} = \frac{\rho_r}{\rho_m}\bigg|_{\text{today}} (1+z) \Rightarrow 1+z_{\text{eq}} = \frac{\rho_m}{\rho_r}\bigg|_{\text{today}}, \tag{3.10}$$

where z_{eq} is the redshift at the time of the matter-radiation equality. We can evaluate those densities today:

$$\begin{aligned} \rho_m^{\text{today}} &= \frac{3H_0^2\Omega_m}{8\pi G} \simeq 1.8\times 10^{-32}\Omega_m h^2 \text{ kg/cm}^3 \\ \rho_r^{\text{today}} &= g_*\frac{\pi^2}{30}\frac{(k_B T_\gamma^{\text{today}})^4}{c^5\hbar^3} \simeq 7.8\times 10^{-37} \text{ kg/cm}^3 . \end{aligned} \tag{3.11}$$

Now, evidence suggests that $\Omega_m h^2 \sim 0.13$, giving $z_{\text{eq}} \sim 3200$, or, in terms of temperature[4], $T_{\text{eq}} \sim 0.74$eV, or approximately 8700 K. In time, integrating (3.9) until $a_{\text{eq}} = 1/(1+z_{\text{eq}}) \approx 0.0003$, it would be approximately 7×10^{-6}secs.

Radiation-Dark Energy equality. A similar estimation can be made in order to know when radiation and dark energy became equal:

$$\begin{aligned} \frac{\rho_r}{\rho_\Lambda} = \frac{\Omega_r}{\Omega_\Lambda} &= \frac{1}{a^4}\frac{\Omega_r^{(0)}}{\Omega_\Lambda^{(0)}} = \frac{4.12\times 10^{-5}}{a^4 h^2 \Omega_\Lambda^{(0)}} \\ a_{eq} \equiv a\big|_{\frac{\rho_r}{\rho_\Lambda}=1} &\approx 0.1 . \end{aligned} \tag{3.12}$$

This is translated into 5.4×10^8 years, redshift $z \approx 9$, and a temperature of 27K approximately, or 0.002eV.

Matter-Dark Energy equality. Finally, the last equality happened "soon" ago, after which the universe became dark energy-dominated and will continue to be like this. The moment in which this occurred is

$$\begin{aligned} \frac{\rho_m}{\rho_\Lambda} = \frac{\Omega_m}{\Omega_\Lambda} &= \frac{1}{a^3}\frac{\Omega_m^{(0)}}{\Omega_\Lambda^{(0)}} = \frac{0.27}{0.73 a^3} \\ a_{eq} \equiv a\big|_{\frac{\rho_m}{\rho_\Lambda}=1} &\approx 0.73 . \end{aligned} \tag{3.13}$$

This is approximately 4×10^9 years ago, at redshift $z \approx 0.37$, when the universe had a temperature of 3.7 K, or 0.0003 eV.

3.3.2 Thermodynamics

Although the evolution of the universe as a whole can be described by its gravitational interactions, this picture is not sufficient to study the behaviour of realistic particle interactions at high temperatures. Here is where the thermodynamic description comes into play.

[4] $T(z) = T_0(1+z)$.

When studying the properties of the early universe one often faces the need of differentiating between different kind of equilibria. Thermal, kinetic and chemical equilibrium are commonly referred in the literature, but a clear definition is usually missing. This may be due to the subtle differences between them.

Thermal equilibrium. It is the state where all the species of the system share the same temperature. Then, the particles A of the system can be described by the distribution function

$$f_A = g_A \frac{1}{e^{(E_A-\mu_A)/T} \pm 1} \,, \tag{3.14}$$

where $(+)$ is for Fermi-Dirac statistics and $(-)$ for Bose-Einstein. In the non-relativistic limit the above expression tends to $f_A \approx \exp[-(E_A-\mu_A)/T]$, which is called the Maxwell-Boltzmann approximation, corresponding to the classical limit. Here μ_A is the corresponding chemical potential, to be defined below, E_A is the particle's energy, and g_A is the spin degeneracy.

The temperature T appearing in (3.14) is of course an essential ingredient in thermodynamics. For a system in thermal equilibrium, it is defined as $T \equiv (\partial U/\partial S)_X$, i.e. the change of internal energy U of the system when varying the entropy S, while keeping constant the rest of macroscopic properties, here collected in X. At the classical level, the Equipartition Theorem directly relates the temperature with the average kinetic energy of the ensemble. However at the quantum level this theorem looses its validity. Still, for practical purposes, it is very useful to think about temperature as an idea of what the kinetic energy of particles are.

Kinetic equilibrium. According to the tight correlation between temperature and average kinetic energy, kinetic equilibrium can be safely identified with thermal equilibrium. A system containing particles A and B is kept in kinetic (or thermal) equilibrium in elastic scatterings of the type $A+B \to A+B$. Once these reactions are not efficient enough, those species *kinetically* decouple. This usually happens for very low temperatures. In the very early universe on the contrary, where the temperature is very high, all existing particles are described by a *thermal bath*, in which thermal equilibrium is present.

Chemical equilibrium. Provided there exist interactions between different species in a system, the chemical equilibrium is present when the number density of reactants and products are constant in time. This kind of equilibrium is maintained by the detailed balance in the reaction $A+\bar{A} \leftrightarrow B+\bar{B}$, for example, where direct and inverse processes are occurring at equal rates. In terms of chemical potentials it implies that $\mu_A + \mu_{\bar{A}} = \mu_B + \mu_{\bar{B}}$. When, for example, the rate of the direct process becomes less than the rate of the inverse (B-annihilation) process, the particles B approaches a *chemical* decoupling.

A rule of thumb to evaluate whether a particle A is in chemical equilibrium with the thermal bath TB, provided the reactions $A+\bar{A} \leftrightarrow TB$ are present, is to compare the reaction rate Γ with the rate of expansion of the universe, given by H. Here $\Gamma = n_A \langle \sigma v \rangle_{A\bar{A}\to \mathrm{TB}}$, where n_A is the number density of the target particles, and $\langle \sigma v \rangle$ the thermally averaged cross-section of the reaction, to be defined in section (3.4). Indeed, $\Delta t = 1/\Gamma$ represents the mean time

between two reactions to occur. On the other hand, if the universe changes its size by Δa in precisely the time Δt, we have $\Delta a/a = H\Delta t$. Thus if the Hubble rate $H \sim \Gamma$, the universe doubles its size in exactly the time one particle finds another target particle. If $\Gamma >> H$, then these reactions can produce and maintain the chemical equilibrium at the plasma temperature T.

The chemical potential is a thermodynamic quantity that can be defined whenever there are conserved charges in the system. A classical example is that of a box containing N particles. There, N is the conserved number in the reaction within the system, thus it makes sense to study how much the energy U of the system changes when extracting or introducing a particle. This is the standard definition of the chemical potential: $\mu \equiv dU/dN$. At the quantum level, it is not the number of particles which can be conserved, but quantum numbers, for example, the Lepton Number L. Reactions like $e^+e^- \to \gamma\gamma$ conserve L, thus it makes sense to define a chemical potential μ_L, which characterises how much the energy of the system changes, when introducing (or extracting) a lepton. However, even if not in a rigorous sense, it is possible to work with assigned chemical potentials, e.g. μ_L, in the case of L-violation, which were defined before L-violation occurs.

In chemical equilibrium, the net chemical potential is locally conserved in a reaction $A + B + ... \leftrightarrow C + D + ...$, meaning that

$$\mu_A + \mu_B + ... = \mu_C + \mu_D + ...$$

This can be used to relate unknown chemical potentials to each other. For example since photons are not conserved (say, in the reaction $e^- + \gamma \to e^- + 2\gamma$), in chemical equilibrium $\mu_\gamma = 0$. This implies that if pair production or annihilation takes place, e.g. $e^+e^- \to 2\gamma$, we have $\mu_{e^+} = -\mu_{e^-}$.

Given the distribution function (3.14), the number density, energy density and pressure are given by

$$n_A = g_A \int \frac{d^3p}{(2\pi)^3} f_A(p), \;\; \rho_A = g_A \int \frac{d^3p}{(2\pi)^3} E_A(p) f_A(p), \;\; P_A = g_A \int \frac{d^3p}{(2\pi)^3} \frac{|p|^2}{3E_A(p)} f_A(p) \; . \tag{3.15}$$

From this we can see another consequence of the chemical potential. Indeed, it is straightforward to see that the particle asymmetry $n_A - n_{\bar{A}}$ of a species A, in presence of chemical equilibrium, ($\mu_{\bar{A}} = -\mu_A$), is such that the asymmetry is zero if $\mu_A = 0$, and vice-versa. This is closely related to the question of conserved charges discussed above. For example for leptons

$$\mu_L = \sum_{i=\mathrm{lep}} \mu_i \neq 0 \Rightarrow \mu_{\ell_1} + \mu_{\bar{\ell}_1} + \mu_{\ell_2} + \mu_{\bar{\ell}_2 + ...} \neq 0 \tag{3.16}$$

meaning that there is some lepton ℓ_i which is not compensated by its $\bar{\ell}_i$ counterpart, i.e. an asymmetry is present.

Coming back to expressions (3.15), it is useful to show their relativistic and non-relativistic limits for bosons B and fermions F.

Relativistic species, small chemical potential: $(m << T, \mu << T)$

$$n_B = \frac{g\zeta(3)}{\pi^2}T^3, \quad n_F = \frac{3}{4}n_B \tag{3.17}$$

$$\rho_B = \frac{g}{30}\pi^2 T^4, \quad \rho_F = \frac{7}{8}\rho_B \tag{3.18}$$

$$P_B = \frac{\rho_B}{3}, \quad P_F = \frac{\rho_F}{3} \tag{3.19}$$

Non-relativistic species: $(m >> T)$

In this case the fermionic and bosonic nature of the particles is irrelevant, and

$$n \approx g\left(\frac{mT}{2\pi}\right)^{3/2} e^{-(m-\mu)/T}, \quad \rho = mn, \quad P \approx nT \tag{3.20}$$

Let us now focus on the entropy. For a system in thermal equilibrium, assuming small chemical potentials, the second Law of thermodynamics can be written as:

$$dU = TdS - PdV \Rightarrow Vd\rho + \rho dV = TdS - PdV\ , \tag{3.21}$$

where the internal energy $U = \rho V$ and $V \propto a^3$ is the volume of the system. On the other hand, the 2nd Friedmann equation can be written in terms of the volume too:

$$\frac{d\rho}{dt} = -3\frac{\dot{a}}{a}(\rho + P) = -\frac{1}{V}\frac{dV}{dt}(\rho + P)\ . \tag{3.22}$$

Substituting this in the time-derivative of (3.21) gives

$$\begin{aligned} -(\rho + P)\frac{dV}{dt} + \rho\frac{dV}{dt} &= T\frac{dS}{dt} - P\frac{dV}{dt} \\ \frac{dS}{dt} &= 0\ . \end{aligned} \tag{3.23}$$

This means that in thermal equilibrium and in the absence of chemical potentials, the entropy is conserved. Consider then the entropy density $s \equiv S/V$. Substitution in (3.21) gives

$$d\rho - Tds = (Ts - \rho - P)\frac{dV}{V}\ ,$$

but since in thermal equilibrium the quantities ρ and s depend only on the temperature, they do not change with the volume, so for every T:

$$s = \frac{\rho + P}{T}\ . \tag{3.24}$$

Let us compute the entropy density due to photons. Using (3.18) and (3.19) we have

$$s_\gamma = \frac{2}{45}\pi^2 g_\gamma T_\gamma^3 \,. \tag{3.25}$$

In fact, from inspection of eqs.(3.17)-(3.20) we can see that the contribution to the total entropy density is strongly dominated by the relativistic species, so we can approximate the total entropy density as the contribution from just the relativistic degrees of freedom. Different species can indeed have different temperatures, if the mean energy differs from one species to other. However, in a state close to thermal equilibrium, those temperatures are expected to be quite similar. It is then useful to express the total entropy density as if it were only due to photons, but absorbing the difference between species in a global effective degeneracy factor g_*^s, instead of the known $g_\gamma = 2$:

$$\begin{aligned} s &= \frac{2\pi^2}{45} g_*^s T_\gamma^3 \\ g_*^s &\equiv \sum_{i=bosons} g_i \left(\frac{T_i}{T_\gamma}\right)^3 + \frac{7}{8}\sum_{i=fermions} g_i \left(\frac{T_i}{T_\gamma}\right)^3 \,. \end{aligned} \tag{3.26}$$

In the very same fashion, we can express the total energy density as:

$$\begin{aligned} \rho &= \frac{\pi^2}{30} g_* T_\gamma^4 \\ g_* &\equiv \sum_{i=bosons} g_i \left(\frac{T_i}{T_\gamma}\right)^4 + \frac{7}{8}\sum_{i=fermions} g_i \left(\frac{T_i}{T_\gamma}\right)^4 \,. \end{aligned} \tag{3.27}$$

In order to see how those ratios T_i/T_γ behave, we need to study the evolution of temperatures for different particles. Since the entropy is conserved:

$$T_\gamma \propto (g_*^s)^{-1/3} a^{-1} \,, \tag{3.28}$$

So in the very early universe, as long as no particle decouples from the plasma, g_*^s is constant and T_γ drops smoothly as $1/a$. However when a particle decouples, g_*^s decreases, and the temperature T_γ receives an extra contribution[5]. T_γ thus decreases less slowly (as compared to $1/a$) in the correspondent decoupling period. After a species is decoupled, its own temperature starts to depart from T_γ.

Physical distances, d_P, and comoving ones, d_c, are related by $d_P = a(t)d_c$. So the momentum p_1 of a particle at the time where the scale factor was a_1, gets red-shifted to $p_2 = \frac{a_1}{a_2} p_1$ in later times, where $a_2 > a_1$. Let us see thus how the temperature of a particle scales with $a(t)$, after being decoupled from the plasma, assuming the universe had a_D at time t_D:

[5] This contribution comes from the annihilation of the particle in the decoupling process, which heats the plasma while ensuring entropy conservation.

a) in the case of relativistic particles ($m << T$), the kinetic energy is basically the momentum ($E_K = p$), so the temperature of relativistic particles scales as $T(t) = [a_D/a(t)]T_D$; b) in the case of non-relativistic particles ($m >> T$), the kinetic energy goes as $E_K \propto p^2$, such that the temperature evolves as $T(t) = [a_D/a(t)]^2 T_D$.

Neutrino decoupling

Using this knowledge, we can study the neutrino decoupling. At high temperatures, neutrinos are kept in equilibrium with the plasma via weak interaction processes (e.g. $\bar{\nu}\nu \leftrightarrow e^+e^-$ mediated by a Z, or $e^-\bar{\nu} \leftrightarrow e^-\bar{\nu}$ through a W^-, etc), with a cross-section which goes essentially as $\sigma_F \simeq G_F^2 E^2 \simeq G_F^2 T^2$. Thus the total interaction rate turns out to be $\Gamma_F = n_\nu \langle \sigma v \rangle \simeq G_F^2 T^5$. Taking into account that in this radiation-dominated epoch $H \simeq 5.44\ T^2/M_{\rm Pl}$, we obtain a rough condition for neutrino decoupling as:

$$\frac{\Gamma_F}{H} \simeq \left(\frac{T}{1\text{MeV}}\right)^3 . \tag{3.29}$$

This means that neutrinos decouple when the temperature was around 1MeV, shortly before the temperature drops below the electron mass. When this happened, almost all the electrons and positrons annihilated into photons [6].

So before neutrino decoupling, when the universe had a scale factor a_1, all the temperatures where the same and the entropy density was $s(a_1) = \frac{43\pi^2}{90} T_1^3$. After annihilation, $T_\nu \neq T_\gamma$, and while $T_\nu \propto 1/a$, T_γ received an extra contribution, coming from the decreasing of g_*^s. The entropy density after annihilation, at time t_2 with $a = a_2$ is $s(a_2) = \frac{4\pi^2}{45}(T_\gamma^3 + 21/8 T_\nu^3)$. But since the entropy is conserved, $s(a_1)a_1^3 = s(a_2)a_2^3$. This leads to

$$\begin{aligned} \frac{43\pi^2}{90} T_1^3 a_1^3 &= \frac{4\pi^2}{45}\left(T_\gamma^3 + \frac{21}{8} T_\nu^3\right) a_2^3 \\ \frac{43\pi^2}{90} T_\nu^3 a_2^3 &= \frac{4\pi^2}{45}\left(\frac{T_\gamma^3}{T_\nu^3} + \frac{21}{8}\right) (T_\nu a_2)^3 \end{aligned} \tag{3.30}$$

where in the second line we have used the fact that $T_\nu a$ is constant. Solving for T_ν leads to

$$T_\nu = \left(\frac{4}{11}\right)^{1/3} T_\gamma \approx 0.7 T_\gamma . \tag{3.31}$$

Hence, neutrinos are an example of a particle whose decoupling occurs while still being relativistic. Actually nowadays the temperature of the universe is smaller than the heaviest neutrino species[7], so we can consider them as non-relativistic. However as they are

[6] Not all, because there is an excess of electrons to have charge neutrality with protons, $n_e = n_p$, but in any case $n_p << n_\gamma$.

[7] Even considering that the lightest neutrino is massless, the masses of the other two species are determined by the known experimental mass differences; and it turns out that the resulting masses are much larger than 2.7K$\sim \mathcal{O}(10^{-13})$GeV.

not in equilibrium since long time, its number density does not get Boltzmann-suppressed, but constant in a comoving volume. In any case, since the neutrino bath is out of equilibrium, it does not conserve entropy in general[8], and consequently the global (photons plus neutrino) bath does not conserve the entropy neither.

Below, we will see that in the case of thermally produced Dark Matter the decoupling occurs when the particle was already non-relativistic; so its number density is Boltzmann suppressed at the time of decoupling, and it essentially does not contribute to the entropy anymore. So in this case there is no entropy conservation issue.

3.4 Dark Matter abundance

The formalism to evaluate not only dark matter's, but all particle's abundances (for example, at BBN) is provided by the Boltzmann equation, which I describe in this section.

The Boltzmann equation generalises the 2nd Friedmann equation which describes how an abundance of a species of particles evolves with time. For matter-domination (dust approximation, $P = 0$) this becomes

$$\dot{\rho} + 3\rho\frac{\dot{a}}{a} = a^{-3}\frac{d}{dt}(\rho a^3) = 0 \Rightarrow a^{-3}\frac{d}{dt}(na^3) = 0\,, \tag{3.32}$$

where n is the abundance (number density) of a species. The Boltzmann equation relates the rate of change in the abundance of a given particle to the difference between the rates for producing and eliminating the species. For a process $1+2 \leftrightarrow 3+4$:

$$\begin{aligned} a^{-3}\frac{d(n_1 a)}{dt} &= \int \prod_{i=1}^{4} \frac{d^3 p_i}{(2\pi)^3 2E_i}(2\pi)^4 \delta^{(4)}(p_1+p_2-p_3-p_4)|\mathcal{M}|^2 \\ &\times \left[f_3 f_4(1\pm f_1)(1\pm f_2) - f_1 f_2(1\pm f_3)(1\pm f_4)\right]\,, \end{aligned} \tag{3.33}$$

where f_i is the distribution function of particle i. Here $+(-)$ refers to bosons (fermions). In the absence of interactions, this Boltzmann equation reduces to the 2nd Friedmann equation.

In the particular case of DM analyses, (3.33) is useful to study the abundance when DM is about to chemically decouple, because before decoupling, as usual, it is a very good approximation to take $n_{\rm DM} \approx n_\gamma$. We have seen with the neutrinos's example that one can have situations where the decoupling occurs when the particle is still relativistic. However, this possibility for DM is highly disfavoured by observations (see the comments about hot and warm relics in section 3.2.2). So, as a cold (non-relativistic) DM is favoured by data (although having some problems mentioned before), we can use this fact to simplify the DM distribution functions to be those of Maxwell-Boltzmann (MB):

$$f_X = \frac{1}{e^{(E_X-\mu_X)/T}\pm 1} \approx e^{-(E_X-\mu_X)/T}\,. \tag{3.34}$$

[8] Remember that the entropy conservation was obtained by assuming a system in thermal equilibrium

However, for the case of particles of the rest of the thermal bath, under the assumption of a cold relic, it means that $m_{\rm DM} > m_{\rm bath}$, so a priori one can not approximate the distribution functions of the bath particles to follow a MB law. It is straightforward to get that the limit for which $1+f_i \approx 1$ (in which case MB applies) is such that $m_{\rm bath} \gtrsim 2T$. This condition is not true in general for a thermal bath made of SM particles, at the time of DM decoupling. However, as shown in the appendix (A)[9], the energy conservation condition of the $b\bar{b} \leftrightarrow \chi\bar{\chi}$ process forces the energy of the bath particles b to be such, that the MB approximation works, even if in the large majority of cases it does not[10].

With this approximation, the last line in (3.33) then becomes

$$e^{-(E_1+E_2)/T}\left[e^{(\mu_3+\mu_4)/T} - e^{(\mu_1+\mu_2)/T}\right]$$

where conservation of energy $(E_1+E_2 = E_3+E_4)$ has been used. Now, since

$$n_i \equiv g_i \int \frac{d^3p}{(2\pi)^3} f_i \approx g_i e^{\mu_i/T} \int \frac{d^3p}{(2\pi)^3} e^{-E_i/T} \ , \tag{3.35}$$

it is useful to define the equilibrium number density $n_i^{\rm eq}$ such that $n_i = n_i^{\rm eq} e^{\mu_i/T}$. Then, we have

$$e^{-(E_1+E_2)/T}\left[e^{(\mu_3+\mu_4)/T} - e^{(\mu_1+\mu_2)/T}\right] = e^{-(E_1+E_2)/T}\left[\frac{n_3 n_4}{n_3^{\rm eq} n_4^{\rm eq}} - \frac{n_1 n_2}{n_1^{\rm eq} n_2^{\rm eq}}\right] .$$

On the other hand, the thermally averaged cross-section $\langle\sigma v\rangle$ can be defined as:

$$\langle\sigma v\rangle \equiv \frac{1}{n_1^{\rm eq} n_2^{\rm eq}} \int \prod_{i=1}^{4} \frac{d^3p_i}{(2\pi)^3 2E_i} (2\pi)^4 \delta^{(4)}(p_1+p_2-p_3-p_4) f_1 f_2 |\mathcal{M}|^2 \ . \tag{3.36}$$

which using the Maxwell approximation becomes

$$\langle\sigma v\rangle \simeq \frac{1}{n_1^{\rm eq} n_2^{\rm eq}} \int \prod_{i=1}^{4} \frac{d^3p_i}{(2\pi)^3 2E_i} (2\pi)^4 \delta^{(4)}(p_1+p_2-p_3-p_4) e^{-(E_1+E_2)/T} |\mathcal{M}|^2 \ . \tag{3.37}$$

Using (3.37), the Boltzmann equation finally simplifies to

$$a^{-3}\frac{d(n_1 a)}{dt} = n_1^{\rm eq} n_2^{\rm eq} \langle\sigma v\rangle \left[\frac{n_3 n_4}{n_3^{\rm eq} n_4^{\rm eq}} - \frac{n_1 n_2}{n_1^{\rm eq} n_2^{\rm eq}}\right] \ . \tag{3.38}$$

From (3.38), one can study all BBN processes, but also the abundances of a particular DM candidate.

[9] This result is not taken from any reference, since in all the literature at hand that approximation is made without a correct justification. However here I have arrived to the result by a proper treatment of the equations.

[10] In the large majority of cases, in the regime $m_{\rm bath} << T << m_{\rm DM}$, we have that $E_{\rm bath} \sim T$, but then nor the production nor the annihilation of DM occurs.

3.4.1 Freeze-out of cold Dark Matter

Had the DM been still in thermal equilibrium, its abundance would be negligible, as shown in eq.(3.20). However this is not what is observed, meaning that at some time, the DM "freezed-out", when the reaction rate became smaller than the expansion rate of the universe, such that it became too rare for a DM particle X to find its partner $\bar{X}$ to self-annihilate.

Consider a generic scenario in which two heavy WIMPs χ and $\bar{\chi}$ annihilate, producing two light (essentially massless) particles l. The light particles are assumed to be in thermal equilibrium with the cosmic plasma, so $n_l = n_l^{\rm eq}$. Then, the Boltzmann equation (3.38) simplifies to:

$$a^{-3}\frac{d(n_\chi a^3)}{dt} = \langle\sigma v\rangle\left[(n_\chi^{\rm eq})^2 - n_\chi^2\right] . \tag{3.39}$$

The LHS of this equation is further reduced to the yield $Y_\chi \equiv n_\chi/s$ as:

$$a^{-3}\frac{d(n_\chi a^3)}{dt} = s\frac{dY_\chi}{dt}$$

where we have used the fact that [11] $s \propto a^{-3}$. The Boltzmann equation can be expressed just in terms of the yield:

$$\frac{dY_\chi}{dt} = \langle\sigma v\rangle s\left[(Y_\chi^{\rm eq})^2 - Y_\chi^2\right] . \tag{3.40}$$

As a function of a new variable $x \equiv m_\chi/T$, this equation becomes:

$$\frac{dY_\chi}{dx} = \frac{\lambda}{x^2}\left[(Y_\chi^{\rm eq})^2 - Y_\chi^2\right] \tag{3.41}$$

where $\lambda \equiv g_*^s \frac{2\pi^2}{45} m_\chi^3 \langle\sigma v\rangle / H(x=1)$ is the ratio of annihilation rate to expansion rate, at the time where the temperature equals the DM mass.

The solution of (3.41) is found numerically and shown in fig. 3.2. There we clearly observe that DM departs from equilibrium at some x value, say $x_{\rm FO}$. The estimation of $x_{\rm FO}$ is done as follows. We consider that around $x_{\rm FO}$ there is a small deviation of $Y_\chi^{\rm eq}$, as $Y = Y_\chi^{\rm eq}(1+\delta)$. Substituting this into (3.41), and writing

$$Y_\chi^{\rm eq} = \frac{n_\chi^{\rm eq}}{s} = \frac{g_\chi}{g_*^s}\frac{45}{2\pi^2}x^{3/2}e^{-x} \tag{3.42}$$

we get

$$1+\delta \approx \frac{g_\chi}{g_*^s}\frac{45}{2\pi^2}\left(\frac{\lambda x e^{-x}}{\frac{3}{2}\sqrt{x} - x^{3/2}}\right)(-2\delta) \tag{3.43}$$

[11] T, taken as the temperature of photons T_γ, is such that $\rho_\gamma \propto T_\gamma^4$, and on the other hand, in radiation-dominated universe, $\rho \propto a^{-4}$.

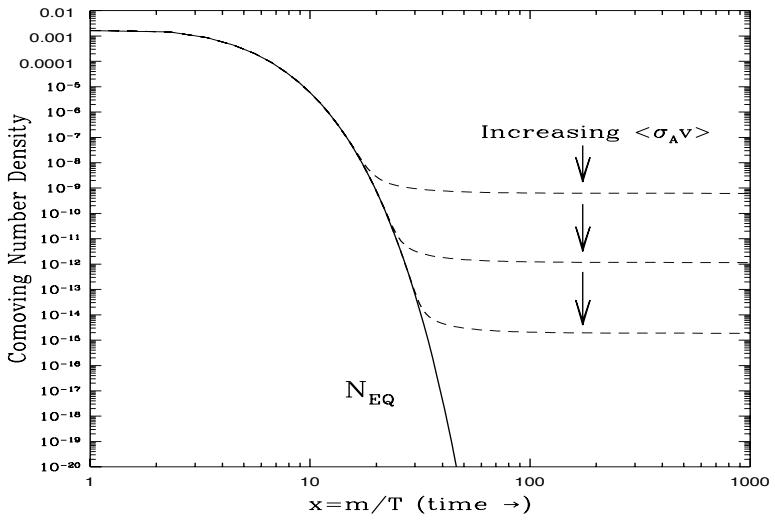

Figure 3.2: Evolution of the comoving number density of DM with temperature. (Taken from "TASI 2008 Lectures on Dark Matter". Dan Hooper, FERMILAB-CONF-09-025A.)

where we have neglected terms of $\mathcal{O}(\delta^2)$, and also the derivative $d\delta/dx$, which holds for sufficiently small δ. Besides, since the freeze-out starts at $T \sim m_\chi$, we have $x \geq 1$ and normally $x^{3/2} > 1.5\sqrt{x}$. The numerical equation for x becomes:

$$x \approx \log\left(\frac{g}{g_*^s}\frac{45}{\pi^2}\frac{\lambda}{\sqrt{x}}\frac{\delta}{1+\delta}\right) \tag{3.44}$$

which is typically, for many theories, around $x_{\rm FO} \sim \mathcal{O}(20)$.

An alternative way of expressing (3.40), which is useful to extract the different solution regimes and connects with the simpler decoupling criterion used before, is given in terms of the reaction rate:

$$\frac{d\log Y_\chi}{d\log a} = -\frac{\Gamma}{H}\left[1-\left(\frac{Y_\chi^{\rm eq}}{Y_\chi}\right)^2\right] \tag{3.45}$$

The qualitative behaviour of the solution of (3.45) can be estimated analytically in some limits. For $\Gamma >> H$ the reactions are occurring so fast that DM have enough time to thermalise, thus $Y_\chi \approx Y_\chi^{\rm eq}$:

$$Y_\chi^{\rm eq} \approx \frac{n_\chi^{\rm eq}}{T^3} = \frac{g_X T^3/\pi^2}{T^3} = \frac{g_X}{\pi^2}\,. \tag{3.46}$$

On the other hand when $\Gamma \approx H$, as soon as $T \lesssim m_\chi$, $Y_\chi^{\rm eq}$ becomes rapidly Boltzmann suppressed and the above equation becomes $\frac{d\log Y_\chi}{d\log a} \approx -\mathcal{O}(1)$. In this regime since DM is semi-decoupled, Y_χ goes down but not as fast as $Y_\chi^{\rm eq}$. Finally, at much later times when $\Gamma << H$,

we have $\frac{d\log Y_\chi}{d\log a} \approx 0$, implying that the comoving number density of DM remains approximately constant in time, thus getting "frozen". The yield today can be analytically estimated as:

$$Y_\chi^0 \simeq \frac{x_{\rm FO}}{\lambda} \,. \tag{3.47}$$

With the yield today, Y_χ^0, it is straightforward to compute the relic density of DM:

$$\Omega_\chi h^2 = \frac{2\rho_\chi}{\rho_{\rm crit}} = \frac{2m_\chi S(T_0) Y_\chi^0}{\rho_{\rm crit}} \simeq \frac{2m_\chi Y_\chi^0}{3.6\times 10^{-9}{\rm GeV}} \,; \tag{3.48}$$

where I have assumed there is no asymmetry in the population of χ with respect to $\bar{\chi}$, and $S(T_0)$ is the entropy today[12].

From eqs.(3.47) and (3.48), one can see that the stronger the annihilation cross-section, the less amount of DM remains until today. This is in general one of the strongest constraints on theories BSM, because for large portions of the parameter space of those theories, one commonly has a too small cross-section, which leads to too much relic density. On the other hand, it may happen that a model, for a particular choice of parameters, gives a too large cross-section. In that case, the contribution of the correspondent DM candidate to the relic density is too small; although the model is not ruled-out as long as one assumes that there exits other contributions which add to the previous one to obtain the correct $\Omega_\chi h^2$.

Finally, some words about the freeze-out of a possible hot relic, as a neutrino-like particle for example. In this case the freeze-out occurs while being relativistic, so when $\Gamma \approx H$, $Y \approx Y^{\rm eq}$, contrary to the cold relic case. Thus the comoving number density remains constant in time.

3.5 Dark Matter Detection

In this section I briefly summarise the idea behind different DM detection methods, and afterwards, I describe those methods for the most important DM detection experiments.

3.5.1 Indirect detection

The Milky Way, as happen with the rest of the galaxies we observe, requires a certain amount of DM to explain observations. This Dark Matter Halo has been the subject of many studies, including complex numerical simulations which are compatible with a DM density profile $\rho_{\rm DM}$ decreases exponentially from the centre to negligible amounts beyond 20 kpc or so. While different profiles differ significantly on the ρ value at the very centre of the galaxy

[12] In general, $S(T) = \frac{2\pi^2}{45} g_*^s(T) T^3$; with g_*^s being the effective number of degrees of freedom in the thermal bath for the entropy.

(some profiles produce divergent densities), the agreement on the local (Earth) value is very good, and presently the central value is $\rho_\odot \simeq 0.43$ GeV/cm^3.

The idea of indirect detection (ID) is that DM particles can annihilate or decay mostly at the Galactic Centre (GC), given that its number density is very high in this region. So even though the kinetic energy of DM particles is presently very suppressed[13], the high number density at the GC allows them to possibly find each other and annihilate. In the case of and unstable DM, even if its lifetime should be very long in order to avoid BBN problems, having that high number density makes it probable for a decay to happen from time to time. In either case, being annihilation or decay, the idea is to register the DM products, which could reach the Earth in the form of cosmic rays (CR). Then, the hope is to observe a cosmic ray signal coming from the GC which could not be explained by known standard astrophysical sources, thus opening the window for a DM interpretation.

The annihilation(decay) sub-products we can look for are photons (from low, radio frequencies to highly energetic gamma-rays), electrons and positrons, neutrinos, (anti)protons as well as (anti)deuterons, for example. They can of course be direct products (primary cosmic rays) of DM, or products of decays of those (secondary cosmic rays).

Balloons. Launching balloons to the sky is a technique which has been used since long time ago (around 1938) and, in spite of the development of satellites as ID experiments, they continue to be used because for some tasks they are very efficient, and very cheap.The CREAM (Cosmic Ray Energetics and Mass) experiment consists of a set of particle detectors (including Cherenkov, tungsten-scintillators, etc) which are able to measure energies between 10^{11}–10^{15} eV, working at a height of 40km. CREAM is presently the best experiment to measure the ratios of secondary to primary cosmic rays, thus being extremely important to constrain cosmic ray propagation. Another balloon experiment is ATIC (Advanced Thin Ionization Calorimeter), which is similar to CREAM but focused on low energies instead, in the range 10–300 GeV.

Satellites. The disadvantage of using balloons is that, as they can not get much higher than some tens of km, the cosmic rays which they detect are contaminated from the interaction with the atmosphere (whose thickness is around 800 km), which introduces important uncertainties. Satellites instead work at much higher altitudes. An example is PAMELA (Payload for Antimatter Matter Exploration and Light-nuclei Astrophysics). It is an italian particle detector installed on-board the russian Resurs-DK1 satellite. It flies at an altitude ranging from 350 to 610 km, and it is probably the best instrument looking at CR of energies lower than 1 TeV. Another satellite-like experiment is the Fermi Gamma-ray space telescope, which is the result of a worldwide collaboration. It works as a particle detector, which however is not able to distinguish particles from antiparticles, since it does not posses a magnet. Because its high altitude orbit (550 km) and its orientation, it can collect a lot of statistics without being affected by the variations of the Earth's magnetic field. They have already released data of electron/positron fluxes in the range of 7 to 870 GeV. A third experiment is called AMS (Alpha Magnetic Spectrometer). Its AMS-02 version is operating on the

[13] Remember than at freeze-out they were already non-relativistic, with kinetic energies $E_K \sim T \sim m_\chi/20$.

International Space Station since 2011, and presently is measuring CR with unprecedented accuracy. It is expected to have its first data release within the next months.

Ground-based experiments. Very high-energy cosmic rays have two important complications: the statistics is very poor because of the very low fluxes, and can not be efficiently studied in outer space because of size limitations. Indeed a typical spatial detector can have at maximum few squared meters, which is not sufficient to study CR beyond few TeV. The ground-based detectors are then useful: they do not observe the CR directly but their showering when passing through the atmosphere. As a typical CR shower is very extense, the probability for detection is high, since those experiments are not quite limited in size, being possible detections areas of several squared km. HESS (High Energy Stereoscopic System) is an example. It consists of four 12m Cherenkov telescopes in Namibia. It has been designed to measure gamma-rays from 100GeV to 100 TeV. KASCADE (The KArlsruhe Shower Core Array DEtector) in Germany is a 700 m $\times$ 700 m array made of almost 300 detectors. KASCADE aims to directly detect the particles of the extended air shower (instead of their Cherenkov light). Pierre Auger cosmic ray observatory, in Argentina, works similarly as KASCADE, but it is much larger (3000 km^2), and is composed by about 1600 detectors, which can jointly study CR energies of about 10^{18} eV, including the identification of their original direction. A final example is the LOFAR experiment (LOw Frequency ARray for radio astronomy), which is a huge array of radio antennas spanning over the Netherlands, the United Kingdom, Sweden, Germany and France. All of them are radio-interferometers listening in the 10–240 MHz frequency band.

3.5.2 Direct Detection

Direct detection (DD) experiments lie behind the idea that our solar system and our planet would be passing through a flux of DM particles. Then, assuming that DM can weakly interact with nucleons, it can deposit a measurable amount of recoil energy within an appropriate detector. This can occur through an elastic scattering between the incident WIMP and a nucleus in the fiducial volume of some detector material.

The effect of an interaction would depend on the DM velocity distribution, which is centred about a few hundred km/s, and of course on the DM mass. With this information the expected energy distribution of events from interacting DM can be calculated. As a result, for an $\mathcal{O}$(GeV) WIMP the typical transferred energy to a nucleus ranges in tens of keV, while the recoil energy of electrons is much more challenging instead (tens of eV). The main DD experiments searching for WIMPs are the following:

XENON. It is located in the Gran Sasso mountain, in Italy. Its new version XENON100 utilises 100kg of fiducial liquid xenon target, and it is expected to register 1 event per 100kg per year. They have recently released results from the last year run, after which two events where observed, consistent with the total background expectation. A profile likelihood analysis of these data leads to the upper limit on the spin-independent elastic WIMP-nucleon scattering cross section, which is minimal (2×10^{-45}cm^2) for a DM mass of 55 GeV at 90%

confidence level. It is presently the most constraining DD experiment among the existing ones. They will soon introduce more material (1ton), which is expected to reduce much more the parameter space of the WIMP models.

CDMS. The name stems for Cryogenic Dark Matter Search. This experiment, located in Minnesota, aims to measure the recoil energy of a nucleus due to collisions with WIMPs by using detectors which are highly sensitive to the ionisation and phonon signals that result from a collision. Its detectors represent the state-of-the-art superconducting films deposited on 600g germanium crystals to accurately measure information about the collisions. The experiment has now increased the experimental sensitivity by a factor 10 and operates at the deeper SNOLAB facility, now operating in Canada. This location provides significantly improved shielding from cosmic rays which are an important source of background in WIMP searches. They have recently reported limits on annual modulation of the low-energy event rate, finding no evidence consistent with nuclear recoils.

CoGeNT. This experiment is also located in Minnesota. It used a 440 gr high-purity germanium crystal cooled to liquid nitrogen temperatures to register nuclear recoils from WIMP collisions. The CoGeNT detector has the advantage of a very low energy threshold (0.5 keV) which allows it to search for events produced by light WIMPs, down to around 5GeV, with very good resolution. Last year, they released data of 145kg.day which show an excess of events at low recoil energies consistent with WIMP-nucleon scattering, pointing towards a 7–8GeV particle with a cross section of about 10^{-40}cm^2. More importantly, they were able to measure the annual modulation of the signal. Because the velocity of the Earth with respect to the dark matter sea changes during the year due to the orbital motion around the Sun, the event rate of dark matter scattering is expected to oscillate with a peak in June and a minimum in December.

DAMA. This experiment is, as XENON, located at Gran Sasso. Several low-background highly-pure scintillator materials have been used, for example, NaI (sodium iodine), with 100kg of material, 6.5kg of LXe (liquid xenon), and the new generation DAMA/LIBRA, with 250kg of NaI, in operation since 2003. Both DAMA/NaI and DAMA/LIBRA have found the presence of annual modulations, claiming a model independent evidence for the presence of DM particles in the galactic halo with 8 standard deviations. However, due to the lack of transparency in the conditions of which this experiment is made, the DAMA signal is up to now taken with some skepticism by the community.

3.5.3 Collider searches

Finally, a third branch of experiments looking for DM, but not exclusively, are the particle colliders. The idea is that profiting an interaction cross-section of electroweak order, WIMPs could be directly produced at those colliders by annihilation of SM particles, in quite the opposite way the DM annihilation works for ID experiments. WIMPs, being weakly interacting, of course escape from the detectors, so the hope is to observe associated final states which one can differentiate from SM background, opening the possibility for a DM interpre-

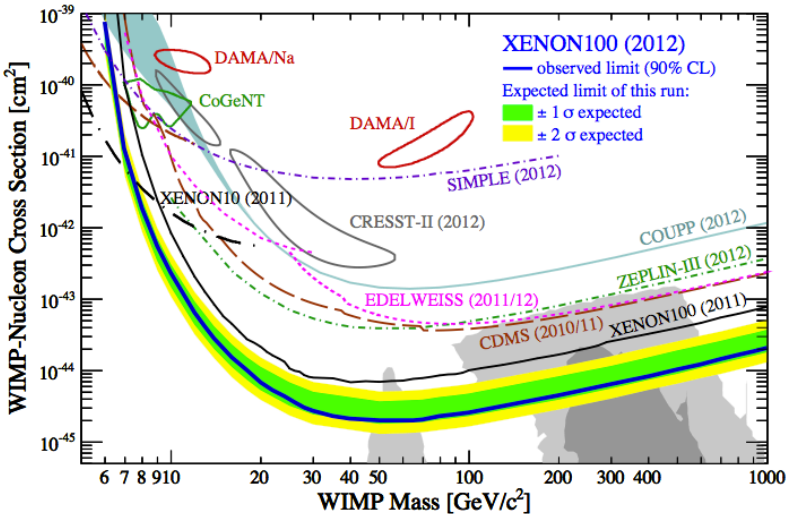

Figure 3.3: Different bounds to DM-nucleon elastic scattering cross-section, coming from direct detection searches. (Taken from "Direct Search for Dark Matter". Josef Jochum. Talk given at "IFT 2012 Xmas Workshop").

tation.

The minimal topology one can study associated to direct WIMP production, is a final state consisting of a single photon, or a single jet. However, there is plenty of studies (mainly in the framework of supersymmetry) which analyse multi-jets or multi-lepton final states associated with DM production. There are many efforts in this direction using LEP, Tevatron and LHC, and it turns out that the level of exclusion reached by collider experiments are complementary to those of DD experiments, being able to probe the very low mass regime quite efficiently, where DD looses all the sensitivity.

CHAPTER 4

FAIR SCANS OF THE SEESAW I

JHEP

Published for SISSA by Springer

Received: November 18, 2010
Revised: February 4, 2011
Accepted: February 13, 2011
Published: March 7, 2011

Fair scans of the seesaw. Consequences for predictions on LFV processes

J. Alberto Casas,[a] **Jesús M. Moreno,**[a] **Nuria Rius,**[b] **Roberto Ruiz de Austri**[b] **and Bryan Zaldívar**[a]

[a] *Instituto de Física Teórica, IFT-UAM/CSIC, Nicolas Cabrera 13, UAM, Cantoblanco, 28049 Madrid, Spain*
[b] *Instituto de Física Corpuscular, IFIC-UV/CSIC, Apartado de Correos 22085, 46071 Valencia, Spain*

E-mail: alberto.casas@uam.es, jesus.moreno@uam.es, nuria@ific.uv.es, rruiz@ific.uv.es, bryan.zaldivar@uam.es

Abstract: We give a straightforward procedure to scan the seesaw parameter-space, using the common "R-parametrization", in a complete way. This includes a very simple rule to incorporate the perturbativity requirement as a condition for the entries of the R-matrix. As a relevant application, we show that the somewhat propagated belief that $\mathrm{BR}(\mu \to e, \gamma)$ in supersymmetric seesaw models depends strongly on the value of θ_{13} is an "optical effect" produced by incomplete scans, and does not hold after a careful analytical and numerical study. When the complete scan is done, $\mathrm{BR}(\mu \to e, \gamma)$ gets very insensitive to θ_{13}. This holds even if the right-handed neutrino masses are kept constant or under control (as is required for succesful leptogenesis). In most cases the values of $\mathrm{BR}(\mu \to e, \gamma)$ are larger than the experimental upper bound. Including (unflavoured) leptogenesis does not introduce any further dependence on θ_{13}, although decreases the typical value of $\mathrm{BR}(\mu \to e, \gamma)$.

Keywords: Neutrino Physics, Supersymmetric Standard Model

ArXiv ePrint: 1010.5751

doi:10.1007/JHEP03(2011)034

JHEP03(2011)034

Contents

JHEP03(2011)034

1 Introduction

It has been claimed [1, 2] that, in the context of the supersymmetric (SUSY) seesaw scenario, the value of the neutrino mixing angle θ_{13} has a strong impact on Lepton Flavour Violation (LFV) processes, in particular on the branching ratio BR($\mu \to e, \gamma$). The basic idea is the following.

As is well known, starting with universal conditions for the soft mass matrices (and thus implementing minimal flavour violation), the renormalization group (RG) running induces non-vanishing off-diagonal entries in the (left-handed) slepton mass matrix, $\mathbf{m_L}^2$. Such entries are mainly generated by the matrix of neutrino Yukawa couplings, $\mathbf{Y}_\nu$; more precisely $(\mathbf{m_L}^2)_{ij} \sim (\mathbf{Y}_\nu^\dagger \mathbf{Y}_\nu)_{ij}$. Then these off-diagonal entries enable LFV processes through one-loop diagrams, as first noticed in [3, 4] and explored in later works (see, for example [1, 5–11]). On the other hand, for given low-energy observables (i.e. neutrino masses

and neutrino mixing matrix), the $\mathbf{Y}_\nu^\dagger \mathbf{Y}_\nu$ matrix has plenty of freedom. This is because in the standard seesaw scenario there are more initial high-energy parameters (18) than low-energy observables (9). Consequently, for given low-energy observables the rate of LFV processes can vary within a certain range. The claim of ref. [2] is that this range typically shifts to larger values as the θ_{13} mixing angle increases; furthermore, such behaviour is strengthened by leptogenesis constraints. The effect is apparently very important, producing increases of several orders of magnitude in $\mathrm{BR}(\mu \to e, \gamma)$ as θ_{13} grows within its experimental window. This remarkable behaviour has been shown up mainly by performing scans upon the seesaw parameters (with and without leptogenesis constraints). An analytical explanation for it has been offered in [12].

In this paper we will show that these results are essentially an optical effect produced by scanning only a part of the whole parameter space of the seesaw. More precisely, these results were obtained using the so-called R-parametrization of the see-saw (see section 3), which is pretty common and useful for studing some issues. However, an incomplete scan of the freedom allowed by the parametrization may lead to biased results. Here we will present easy rules to perform complete explorations in this parametrization, incorporating the perturbativity requirement. We will show that when such appropriate scan is implemented, the impact of θ_{13} is very small, even negligible.

The insensitivity to θ_{13} was already noticed in refs. [10, 13] using an alternative parametrization of the seesaw parameter space (called V_L-parametrization in the present paper, see details in section 3). We will show here that such insensitivity holds in the R-parametrization, even when the values of the right-handed neutrino masses are kept constant or under control (as is required for succesful leptogenesis), provided the remaining freedom is scanned in a complete way (something non-trivial to check in the V_L-parametrization). For related work see [14, 15].

In section 2 we present the framework and set the notation. Section 3 is devoted to describe the two parameterizations of the seesaw we are dealing with in this work. In section 4 we show and explain the apparent contradiction between the two approaches, concerning the dependence of $\mathrm{BR}(\mu \to e, \gamma)$ on the θ_{13} angle. In section 5 we give a procedure to scan the seesaw parameter space in a fair way, incorporating the constraint of perturbativity (details are given in appendix A). In the same section and section 6, we study both in an analytical and numerical way the dependence of $\mathrm{BR}(\mu \to e, \gamma)$ on θ_{13}, making use of the mentioned scan. Section 7 is devoted to the inclusion of leptogenesis constraints. Finally, in section 8 we present our main conclusions.

2 Framework and notation

From now on we use the conventions and notation of ref. [16].

In the standard SUSY seesaw the relevant superpotential is

$$W \supset e_R^{c\,T} \mathbf{Y_e} L \cdot H_1 + \nu_R^{c\,T} \mathbf{Y}_\nu L \cdot H_2 - \frac{1}{2} \nu_R^{c\,T} \mathbf{M} \nu_R^c \,, \tag{2.1}$$

where L (e_R^c) are the leptonic doublets (charged singlets), ν_R are the right-handed neutrinos and $H_{1,2}$ are the two supersymmetric Higgs doublets. $\mathbf{Y_e}$ and $\mathbf{Y}_\nu$ are Yukawa matrices

JHEP03(2011)034

in flavor space (flavor indices are dropped) and $\mathbf{M}$ is the Majorana mass matrix of right-handed neutrinos. Once right-handed neutrinos are decoupled (at the seesaw scale $\sim M$) a mass operator is left in the effective superpotential,

$$W_{\text{eff}} \supset {e_R^c}^T \mathbf{Y_e} L \cdot \bar{H}_1 + \frac{1}{2}(\mathbf{Y}_\nu L H_2)^T \mathbf{M^{-1}} (\mathbf{Y}_\nu L H_2) \,. \tag{2.2}$$

Then, the effective mass matrix for the light ($\sim$ left-handed) neutrinos is

$$\mathcal{M}_\nu = \langle H_2^0 \rangle^2 \kappa \,, \tag{2.3}$$

with

$$\kappa = {\mathbf{Y}_\nu}^T \mathbf{M}^{-1} \mathbf{Y}_\nu \,. \tag{2.4}$$

Note that the seesaw equations (2.2), (2.4) are valid at the seesaw scale. Besides, they are obtained using the (reasonable) approximation of decoupling at a unique threshold, instead of a (more accurate) decoupling in three steps (the three right-handed neutrino masses).

The neutrino mass-eigenvalues, $m_i = \langle H_2^0 \rangle^2 \kappa_i$, and the mixing matrix, U_{MNS}, are given by

$$D_\kappa = U_{\text{MNS}}^T \, \kappa \, U_{\text{MNS}}, \qquad D_\kappa \equiv \text{diag}(\kappa_1, \kappa_2, \kappa_3), \tag{2.5}$$

with $\kappa_1 \leq \kappa_2 \leq \kappa_3$. The standard parametrization of the MNS matrix is

$$U_{\text{MNS}} = \begin{pmatrix} c_{13}c_{12} & c_{13}s_{12} & s_{13}e^{-i\delta} \\ -c_{23}s_{12} - s_{23}s_{13}c_{12}e^{i\delta} & c_{23}c_{12} - s_{23}s_{13}s_{12}e^{i\delta} & s_{23}c_{13} \\ s_{23}s_{12} - c_{23}s_{13}c_{12}e^{i\delta} & -s_{23}c_{12} - c_{23}s_{13}s_{12}e^{i\delta} & c_{23}c_{13} \end{pmatrix} \begin{pmatrix} e^{-i\phi/2} & & \\ & e^{-i\phi'/2} & \\ & & 1 \end{pmatrix} \tag{2.6}$$

From now on, for the sake of notation clarity, we will drop labels in the neutrino mixing and Yukawa matrices: $U \equiv U_{\text{MNS}}$, $\mathbf{Y} \equiv \mathbf{Y}_\nu$.

3 Parameterizations of the seesaw

The high-energy seesaw Lagrangian, given by the superpotential (2.1), is determined by the entries of the $\mathbf{Y}$ and $\mathbf{M}$ matrices, which contain 18 independent parameters. On the other hand, there are 9 low-energy neutrino observables: the three neutrino masses, $\propto \kappa_i$, and the three mixing angles and the three phases contained in U. Hence, for given values of the low-energy observables, the freedom in the seesaw Lagrangian expands a 9-dimensional parameter space. There are two main ways of describing such space (or, in other words, of parametrizing our ignorance). We will call them the $R-$parametrization and the V_L-parametrization.

3.1 $R-$parametrization

It was shown in [16] that, for a given set of low-energy observables, κ_i and U, the neutrino Yukawa matrix (at the seesaw scale) has the form:

$$\mathbf{Y} = D_{\sqrt{M}} R D_{\sqrt{\kappa}} U^\dagger \,, \tag{3.1}$$

JHEP03(2011)034

where $D_{\sqrt{M}} = \mathrm{diag}\{\sqrt{M_i}\}$, $D_{\sqrt{\kappa}} = \mathrm{diag}\{\sqrt{\kappa_i}\}$, and R is a complex orthogonal (3×3) matrix. So, the 9 see-saw parameters that parametrize our ignorance are the three right-handed masses and the 3 complex angles defining R. A usual parametrization of R is

$$R = \begin{pmatrix} c_2c_3 & -c_1s_3 - s_1s_2c_3 & s_1s_3 - c_1s_2c_3 \\ c_2s_3 & c_1c_3 - s_1s_2s_3 & -s_1c_3 - c_1s_2s_3 \\ s_2 & s_1c_2 & c_1c_2 \end{pmatrix} , \tag{3.2}$$

where s_i (c_i) are the sine (cosine) of the three complex angles θ_i. Eq. (3.2) is general up to reflections changing the sign of $\det R$.

3.2 V_L-parametrization

An alternative to the $R-$parametrization is the so-called V_L-parametrization, see ref. [13, 17]. For a given set of low-energy observables, κ_i and U, the neutrino Yukawa matrix (at the seesaw scale) can be written as

$$\mathbf{Y} = V_R D_Y V_L^\dagger \, . \tag{3.3}$$

Here D_Y is the diagonal matrix containing the three (real and positive) neutrino Yukawa couplings, y_i; V_L is a unitary matrix with identical structure as the MNS matrix [eq. (2.6)], but, of course, with three different mixing angles and three different phases; and V_R has also identical structure but with the diagonal matrix of phases acting from the left (for more details see e.g. [18]). Here, the 9 independent parameters that parametrize our ignorance are the three Yukawa couplings, y_i, and the three angles and three phases contained in V_L. The V_R-matrix and the three right-handed neutrino masses are obtained by substituting eq. (3.3) in the seesaw expression (2.4), namely

$$V_R^\dagger D_M V_R^* \;=\; D_Y V_L^\dagger U D_\kappa^{-1} U^T V_L^* D_Y \, , \tag{3.4}$$

i.e. V_R is the unitary matrix that diagonalizes the symmetric matrix in the right hand side of (3.4) and D_M is the corresponding diagonal matrix, which contains the three right-handed masses.

4 The impact of θ_{13}

As mentioned in the introduction, even starting with diagonal and universal soft masses, the RG running generates off-diagonal entries in them. In particular, the (left) slepton mass matrix gets off-diagonal entries $(\mathbf{m_L}^2)_{ij}$, $i \neq j$, proportional (in the leading-log approximation) to the $(\mathbf{Y}^\dagger\mathbf{Y})_{ij}$ matrix element. On the other hand, at first order in the mass-insertion expansion, the branching ratio of the LFV process $l_i \to l_j, \gamma$ (with $l_{i,j}$ charged leptons of the i, j families) is non-vanishing and proportional to the squared of the corresponding off-diagonal entry, $|(\mathbf{m_L}^2)_{ij}|^2$.

Consequently, the dependence of, say $\mathrm{BR}(\mu \to e, \gamma)$, on the MNS matrix (and in particular on θ_{13}) occurs mainly via the dependence of $(\mathbf{Y}^\dagger\mathbf{Y})_{21}$ on it. This becomes more

JHEP03(2011)034

clear from the following approximate formula for the branching ratio, which will be useful later for qualitative discussions,

$$\mathrm{BR}(\mu \to e,\gamma) \sim \frac{\alpha^3}{G_F^2 m_S^8} \left| -\frac{1}{8\pi^2}(3m_0^2 + A_0^2)\log\frac{M_X}{M} \right|^2 \left| (\mathbf{Y}^\dagger \mathbf{Y})_{21} \right|^2 \tan^2\beta \ . \tag{4.1}$$

Here m_S represents a typical supersymmetric leptonic mass, and m_0, A_0 are the universal scalar mass and the universal trilinear coupling at the unification scale M_X.

Next, we analyze the dependence of $(\mathbf{Y}^\dagger\mathbf{Y})_{21}$ on θ_{13} using the two parametrizations of the seesaw discussed in section 3. We will find first a kind of "paradox", then we will discuss its explanation.

4.1 A "paradox"

In the $R-$parametrization the $\mathbf{Y}^\dagger\mathbf{Y}$ matrix can be easily obtained from eq. (3.1):

$$\mathbf{Y}^\dagger\mathbf{Y} = U D_{\sqrt{\kappa}} R^\dagger D_M R D_{\sqrt{\kappa}} U^\dagger \ . \tag{4.2}$$

This equation tells us that, for given right-handed masses (D_M) and a given $R-$matrix, $\mathbf{Y}^\dagger\mathbf{Y}$ (and thus LFV processes) has a non-trivial dependence on U. Let us concentrate for the moment on the $(\mathbf{Y}^\dagger\mathbf{Y})_{21}$ matrix element, which is the relevant one for $\mu \to e,\gamma$. Assuming a hierarchical spectrum of neutrinos, $\kappa_1 \ll \kappa_2 \ll \kappa_3$, we can expand $(\mathbf{Y}^\dagger\mathbf{Y})_{21}$ in powers of $\sqrt{\kappa_i}$. The first term of such expansion is

$$(\mathbf{Y}^\dagger\mathbf{Y})_{21} \ = \ \kappa_3 U_{23} \left[R^\dagger D_M R\right]_{33} U_{13}^* \ + \ \cdots \tag{4.3}$$

Since $|U_{13}| = |s_{13}|$ and $|U_{23}| \sim 1/\sqrt{2}$, we see that, in this approximation,

$$(\mathbf{Y}^\dagger\mathbf{Y})_{21} \ \propto \ s_{13} \ . \tag{4.4}$$

This dependence on s_{13} is quite strong, and is really the source of the dependence of $\mathrm{BR}(\mu \to e,\gamma)$ on $\sim s_{13}^2$ observed in the literature (this was also noticed in [12]). An analogous argument shows that $\mathrm{BR}(\tau \to e,\gamma)$ has a similar dependence on s_{13}, while $\mathrm{BR}(\tau \to \mu\gamma)$ is almost independent of θ_{13}. We will discuss soon the validity of the previous expansion, and thus of these results.

Let us now turn to the V_L-parametrization. From (3.3)

$$\mathbf{Y}^\dagger\mathbf{Y} = V_L D_Y^2 V_L^\dagger \ . \tag{4.5}$$

Clearly, now $\mathbf{Y}^\dagger\mathbf{Y}$ does not depend at all on U. For given Yukawa couplings (D_Y) any choice of V_L is compatible with any choice of U and thus of θ_{13}. So, varying θ_{13} does not affect $\mathbf{Y}^\dagger\mathbf{Y}$ at all. This result seems to be in contradiction with the one obtained using the $R-$parametrization.

One might argue that changing θ_{13} in the V_L-parametrization means moving along a line of constant y_i and V_L in the seesaw parameter space; while changing θ_{13} in the $R-$parametrization means moving along a line of constant M_i and R. It may happen that

JHEP03(2011)034

$(\mathbf{Y}^\dagger\mathbf{Y})_{21}$ keeps constant along the first line but it increases along the second one. This is true, but even assuming this possibility there remains a conflict, as we are about to see.

Let us work first in the V_L-parametrization. Assuming hierarchical neutrino Yukawa couplings, $y_1^2 \ll y_2^2 \ll y_3^2$, it is obvious that the choice of V_L that maximizes $(\mathbf{Y}^\dagger\mathbf{Y})_{21}$ in eq. (4.5) is $|(V_L)_{13}| = |(V_L)_{23}| = 1/\sqrt{2}$. Then

$$\left(\mathbf{Y}^\dagger\mathbf{Y}\right)_{21}^{\max} = \frac{1}{2}y_3^2 \ . \tag{4.6}$$

As mentioned above, this value is available for any choice of U. Let us keep fixed all mixings and phases in U, except θ_{13}. For each value of θ_{13}, the $\mathbf{Y}^\dagger\mathbf{Y}$ matrix remains the same, but D_M and V_R change according to eq. (3.4). The corresponding $\mathbf{Y}$ matrix is given by (3.3). Suppose we choose $\theta_{13} = 3^o$ and then calculate D_M and V_R, and write $\mathbf{Y}$. This matrix can be easily expressed in the $R-$parametrization. Namely, in eq. (3.1) we can straightforwardly solve R in terms of $\mathbf{Y}$, U, D_M and D_κ, which are known. We can wonder now what happens if we keep these values of D_M and R fixed, and vary θ_{13}. The $\mathbf{Y}$ matrix will change according to (3.1), but the Yukawa eigenvalues, y_i^2 will not change, as it is obvious from eq. (4.2). From the point of view of the V_L-parametrization the change in $\mathbf{Y}$ is due to a change in V_R *and* V_L. Therefore $\left(\mathbf{Y}^\dagger\mathbf{Y}\right)_{21}$ departs necessarily from its maximum value (4.6) and can only decrease in magnitude. However, from the point of view of the $R-$parametrization, the approximate expression eq. (4.3) tells us that an increase of s_{13} should reflect in an increase in the magnitude of $\left(\mathbf{Y}^\dagger\mathbf{Y}\right)_{21}$! So, at least we have found a choice of R for which the impact of θ_{13} on $\left(\mathbf{Y}^\dagger\mathbf{Y}\right)_{21}$ [and thus of BR$(\mu \to e, \gamma)$] goes exactly opposite that claimed in the literature.

4.2 The reason behind

The solution to the previous conflict can be found by doing the above steps explicit. We start with a choice for the Yukawa eigenvalues, D_Y, and a V_L matrix that maximizes $\left(\mathbf{Y}^\dagger\mathbf{Y}\right)_{21}$ in eq. (4.5). The corresponding D_M, V_R can be obtained from eq. (3.4). One can construct now the $\mathbf{Y}$ matrix from (3.3). Then, using the $R-$parametrization (3.1), it is straightforward to derive the $R-$matrix (say $\hat{R}$) that corresponds to this optimal choice:

$$\hat{R} \ = \ D^{-1}_{\sqrt{M}} V_R D_Y V_L^\dagger U D^{-1}_{\sqrt{\kappa}} \ , \tag{4.7}$$

(it is funny to check that $\hat{R}$ is orthogonal indeed). If we keep now $\hat{R}$ and D_M constant but change the MNS matrix, $U \to U'$ (e.g. by varying θ_{13}), it is straightforward from eq. (4.2) that the new $\mathbf{Y}'^\dagger\mathbf{Y}'$ matrix reads

$$\mathbf{Y}'^\dagger\mathbf{Y}' = U'U^\dagger V_L D_Y^2 V_L^\dagger \, UU'^\dagger = U'U^\dagger \mathbf{Y}^\dagger\mathbf{Y} UU'^\dagger \ . \tag{4.8}$$

Obviously, $\left|(\mathbf{Y}'^\dagger\mathbf{Y}')_{21}\right| \ \leq \ \left|(\mathbf{Y}^\dagger\mathbf{Y})_{21}\right|$ (recall that V_L was "designed" to maximize this quantity in eq. (4.5)). So something goes wrong with the argument used to obtain eqs. (4.3), (4.4). To see what, we construct the $\hat{R}^\dagger D_M \hat{R}$ matrix that appears in the expansion (4.3):

$$\hat{R}^\dagger D_M \hat{R} \ = \ D^{-1}_{\sqrt{\kappa}} \, U^\dagger Y^\dagger Y U \, D^{-1}_{\sqrt{\kappa}} \ . \tag{4.9}$$

JHEP03(2011)034

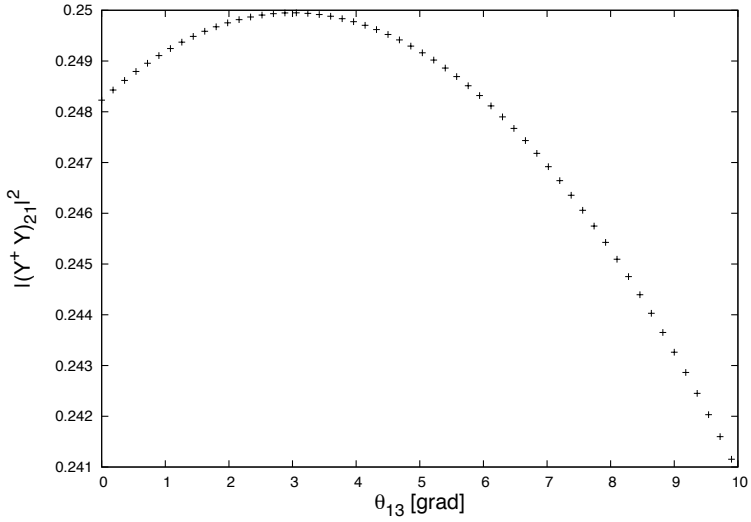

Figure 1. $(|\mathbf{Y}^\dagger\mathbf{Y})_{21}|^2$ vs. θ_{13} for a given $\hat{R}-$matrix, correspondent the expression (4.7). Here $D_M = (10^{10}, 10^{11}, 10^{12})\,\text{GeV}$.

Hence

$$\left(\hat{R}^\dagger D_M \hat{R}\right)_{ij} \propto \frac{1}{\sqrt{\kappa_i \kappa_j}}\,. \tag{4.10}$$

The consequence is that all terms neglected in (4.3) are in principle as large as the first term: the expansion is not sensible. In figure 1 we have plotted $(|\mathbf{Y}^\dagger\mathbf{Y})_{21}|^2$ against θ_{13}, keeping $\hat{R}$, D_M constant, for this particular example. As expected, the maximum occurs at $\theta_{13} = 3^o$ and for larger θ_{13} the matrix element decreases.

Thus we have constructed an explicit counter-example, where the dependence of $(\mathbf{Y}^\dagger\mathbf{Y})_{21}$ on θ_{13} goes opposite that naively expected. This raises the question: Is this "wrong" behaviour a consequence of the special choice of the seesaw parameters ($\hat{R}$ and D_M) taken above or it is more general? What can we expect for a generic choice of R and D_M?

5 Fair scans in the $R-$matrix and the perturbativity condition

The final questions of the previous section pose an interesting issue: how can we perform a truly generic scan in the $R-$matrix? In the literature one can find several approaches. Sometimes the $R-$matrix is simply frozen, as in [11, 19]. Sometimes the real and imaginary parts of the θ_i angles appearing in the parametrization (3.2) are separated. Then the real part is varied as an ordinary angle, say $0 \leq \text{Re}\ \theta_i \leq 2\pi$, which is really general, and the imaginary part is fixed to zero (see e.g. [20]), or scanned within a range similar to the real part (as in refs. [1, 2]). This is not general, since Im θ_i can in principle take any value in the $\{-\infty, \infty\}$ range. Of course a too-large value of Im θ_i is not realistic, since it leads to non-perturbative Yukawa couplings, making the whole approach inconsistent. We will

JHEP03(2011)034

come back soon to this point. Other different, but still incomplete, scans of the $R-$matrix can be found in [14] or [21]. On the other hand, in some cases it has been argued that for certain physical problems a particular (incomplete but suitable) scan was fair enough, as in [22]. In ocassions a truly general scan has been attempted, as in [23].

In this section we address the issue of performing a complete scan of the $R-$matrix, examining the restrictions that the perturbativity criterion imposes on the magnitude of the R_{ij} entries. We will see that they are quite simple, but very different from just choosing a certain range for Im θ_i.

The perturbativity requirement has to do with the Yukawa eigenvalues, D_Y. Since, for a given D_M and R, these do not depend on the $U-$matrix [see eqs. (3.1) or (4.2)], the perturbativity criterion cannot depend on U either. A simple and sensible approach is to impose a constraint on the trace of Yukawa couplings, say

$$\text{tr } \mathbf{Y}^\dagger \mathbf{Y} \;=\; \sum_i y_i^2 \;\lesssim 3\,, \tag{5.1}$$

(of course, any $\mathcal{O}(1)$ number is as good as 3 here). Now, from eq. (4.2),

$$\text{tr } \mathbf{Y}^\dagger \mathbf{Y} = \sum_{j=1,2,3} \kappa_j \left[R^\dagger D_M R\right]_{jj}\,, \tag{5.2}$$

so the perturbativity constraint (5.1) translates into

$$|R_{ij}|^2 \;\lesssim\; \frac{1}{M_i \kappa_j}\,. \tag{5.3}$$

This condition is very handy and easy-to-use. Besides, it clearly applies whether or not we consider a supersymmetric version of the seesaw. An important remark is that the perturbativity requirement does not affect equally the magnitude of the various R_{ij} entries. Actually, they can be easily different by orders of magnitude. This is clearly in contrast with typical scans of the $R-$matrix in the literature. It also explains the structure of the $\hat{R}$-matrix [eq. (4.7)]. Recall that $\hat{R}$ was constructed to maximize $\left(\mathbf{Y}^\dagger \mathbf{Y}\right)_{21}$ at a certain value of θ_{13}. Then $\left(\mathbf{Y}^\dagger \mathbf{Y}\right)_{21}$ decreases for increasing θ_{13}, in contrast to the usual behaviour observed in the literature. But $\hat{R}$ is not a usual matrix considered in the literature. Actually, it "exploits" the perturbativity condition (5.3) to the extreme, as is clear from eq. (4.7). But it still corresponds to a perfectly sensible $\mathbf{Y}$ matrix.

Now, we can pose the following question: For a given D_M, once R is scanned in all its generality (respecting perturbativity and orthogonality conditions), what is the corresponding range for $\left(\mathbf{Y}^\dagger \mathbf{Y}\right)_{21}$ *and* how does it change when θ_{13} is varied?[1] Intuitively, since $y_3^2 \leq \text{tr}\mathbf{Y}^\dagger \mathbf{Y}$, we can expect a global range (see eq. (4.6))

$$0 \lesssim \left|(\mathbf{Y}^\dagger \mathbf{Y})_{21}\right| \lesssim \frac{1}{2}\text{tr}\mathbf{Y}^\dagger \mathbf{Y}\,. \tag{5.4}$$

[1]This is not just an academic problem, since a similar one arises typically when leptogenesis constraints are incorporated, as we will see soon. Such a task is more naturally addressed in the $R-$parametrization (which can keep M_i fixed) than in the V_L-one.

JHEP03(2011)034

But still we do not know how feasible or natural is to reach these bounds depending on the value of θ_{13}, or how $\left(\mathbf{Y}^\dagger\mathbf{Y}\right)_{21}$ changes with θ_{13} for a fixed vanilla R. We have studied this in a numerical way (more details in short), but we can get insight into these issues by examining the expression of $\left(\mathbf{Y}^\dagger\mathbf{Y}\right)_{21}$ in the $R-$parametrization [eq. (4.2)] more closely. This expression can be written as

$$\left(\mathbf{Y}^\dagger\mathbf{Y}\right)_{21} = \sum_{j,k=1}^{3} U_{2k}\sqrt{\kappa_k}R^*_{jk}M_j\left(R_{j3}\sqrt{\kappa_3}U^*_{13} + \sum_{i=1}^{2} R_{ji}\sqrt{\kappa_i}U^*_{1i}\right) . \tag{5.5}$$

Since $|U_{13}| = |s_{13}|$, the first term within the brackets is the responsible for the $\theta_{13}-$dependence observed in the literature. However, the other two terms within the brackets can be easily as big as the first one. Note first that $\sqrt{\kappa_2}$ is only a factor $\sim 1/\sqrt{6}$ smaller than $\sqrt{\kappa_3}$, a difference that is easily compensated by the fact that $|U_{13}| < |U_{12}|$. Besides, the perturbativity condition (5.3) implies that typically all the $\sqrt{\kappa}$ factors in (5.5) are compensated by the typical sizes of the $R-$matrix elements. In consequence, changing θ_{13} is not likely to have a noticeable impact on $\left(\mathbf{Y}^\dagger\mathbf{Y}\right)_{21}$, certainly not orders of magnitude for vanilla $R-$matrices. This simple argument can be made more rigorous (and cumbersome) once the orthogonality conditions on the R entries are imposed. But the basic result, that the range of $\left(\mathbf{Y}^\dagger\mathbf{Y}\right)_{21}$ cannot depend much on the value of θ_{13}, remains. This contradicts the common lore in the literature, and it is much more consistent with the result obtained using the V_L-parametrization.

Let us now show the results of the numeric scan. First of all, we need a systematic procedure to scan the whole range of $R-$matrices, consistent with the perturbativity condition (5.3) and the orthogonality condition, $R^T R = \mathbf{1}$. A simple way to do it is explained in appendix A. Then, for each $R-$matrix considered, we scan θ_{13} in the 0^o-10^o range. Besides, for the numerical example we have taken the following values for the other parameters:

$$\begin{aligned}
&m_1 = 10^{-12}\,\text{GeV}, && m_2 = 9\times 10^{-12}\,\text{GeV}, && m_3 = 5\times 10^{-11}\,\text{GeV},\\
&\theta_{12} = \pi/6, && \theta_{23} = \pi/4, && \delta = \phi_1 = \phi_2 = 0,\\
&M_1 = 10^{10}\,\text{GeV}, && M_2 = 10^{11}\,\text{GeV}, && M_3 = 10^{12}\,\text{GeV}\,.
\end{aligned} \tag{5.6}$$

Furthermore, we have used $\tan\beta \gtrsim 10$, so that $\langle H_2^0\rangle \simeq v/\sqrt{2}$, with $v = 246\,\text{GeV}$. The results of the scan in R and θ_{13} are shown in figure 2. As expected, the dependence of $\left(\mathbf{Y}^\dagger\mathbf{Y}\right)_{21}$ on θ_{13} is very small, almost negligible. Note that, indeed, there are cases for which the dependence is stronger, corresponding to $R-$matrices which are far below the perturbativity limit (5.3), but those are statistically rare exceptions.

6 The branching ratio BR($\mu \to e, \gamma$)

In oder to translate these results about $\left(\mathbf{Y}^\dagger\mathbf{Y}\right)_{21}$ into predictions for the branching ratio $\text{BR}(\mu \to e, \gamma)$, we have to assume first a supersymmetric model. We have chosen a minimal supergravity (mSUGRA) model defined by

$$m_0 = 500\,\text{GeV},\ M_{1/2} = 250\,\text{GeV},\ A_0 = -100\,\text{GeV},\ \tan\beta = 10, \tag{6.1}$$

JHEP03(2011)034

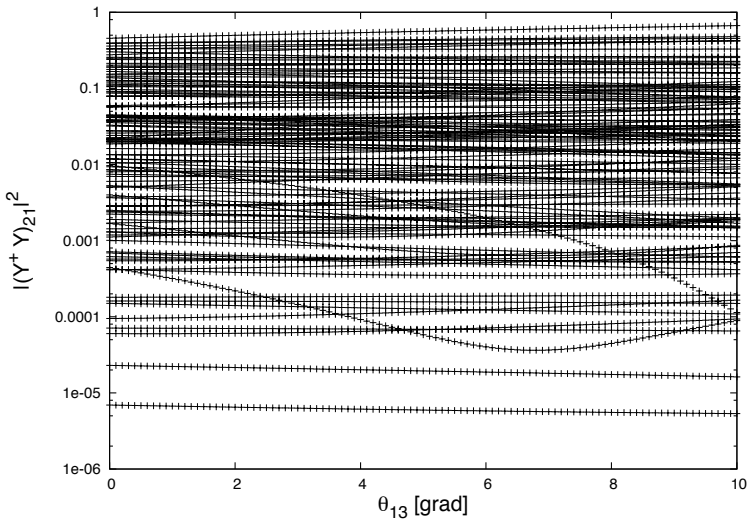

Figure 2. Scatter plot of $(|\mathbf{Y}^\dagger\mathbf{Y})_{21}|^2$ vs. θ_{13} for different $R-$matrices obeying the perturbativity condition (5.3).

where m_0, $M_{1/2}$ and A_0 are the universal scalar mass, gaugino mass and trilinear coupling at the unification scale M_X. Then we have calculated BR($\mu \to e, \gamma$) for the same random set of $R-$matrices used for figure 2. The computation was made by means of our own modified version of the SPheno code [24], which uses the full one-loop expressions of ref. [25]. The results are shown in figure 3 (left panel). As expected, the dependence of BR($\mu \to e, \gamma$) on θ_{13} follows closely the one of $\left|(\mathbf{Y}^\dagger\mathbf{Y})_{21}\right|^2$, shown in figure 2. Concerning the size of BR($\mu \to e, \gamma$), we see that in general is very large, quite above the experimental upper bound. This is in fact not surprising: using the approximate general range (5.4) and the approximate formula (4.1), one can check that the expected branching ratio is very large. Some comments are in order here. First, although it is common lore that BR($\mu \to e, \gamma$) can be large for an ordinary minimal SUGRA model, we see here that, after performing a complete scan, the value of the branching ratio is typically quite above the experimental upper bound, which is a very suggesting result. Second, although it is not visible in figure 3, there are of course choices of R leading to branching ratios well below the experimental limit. What happens is that, scanning the space of the $R-$matrices in the way we did it, the number of those "good" $R-$matrices is relatively very small. However, one has to keep in mind that scanning the $R-$parameter space in a different way (in Bayesian language, using a different prior for that space), the abundance of those "good" $R-$matrices will change. The dependence of these results on the prior is out of the scope of this paper. Nevertheless it is worth noticing that the same prior dependence was implicit in the scatter plots shown in the previous literature. Let us finally remark that by changing the parameters (6.1) of the mSUGRA model, the branching ratio changes parametrically, as indicated in the approximate formula (4.1).

For the sake of comparison between parametrizations, we have also shown in figure 3 (right panel) a similar survey using the V_L-parametrization. In this case we have to

JHEP03(2011)034

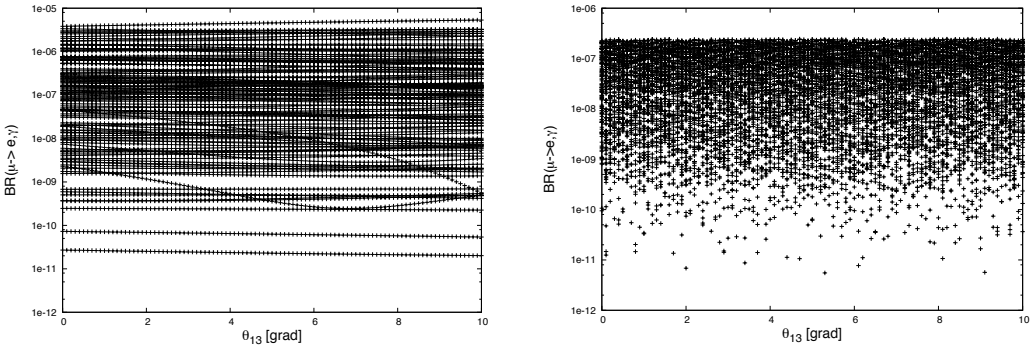

Figure 3. BR($\mu \to e, \gamma$) vs. θ_{13}. (left) $R-$parametrization; (right) V_L-parametrization.

choose the values of the three neutrino Yukawa couplings. We have taken $y_1 = 0.0011$, $y_2 = 0.03$, $y_3 = 1$. Besides, we have chosen the same mSUGRA model defined in eq. (6.1). Recall that in this parametrization $\left(\mathbf{Y}^\dagger \mathbf{Y}\right)_{21}$ does not depend at all on θ_{13}. The branching ratio does, but in a marginal way. All this is apparent from figure 3. Now, comparing the surveys with the $R-$ and V_L-parametrizations (left and right panels) we note a similar insensitivity to θ_{13}, which is one of our main results. Besides, in the figure we see that the branching ratios in the $R-$parametrization can be more than one order of magnitude larger than in the V_L one. This is mainly due to the choice $y_3 = 1$ in the latter. Note that in the $R-$parametrization we have imposed $\mathrm{tr}\mathbf{Y}^\dagger\mathbf{Y} \leq 3$, which allows $y_3^2 \lesssim 3$. Therefore the upper limit of $\left|(\mathbf{Y}^\dagger\mathbf{Y})_{21}\right|^2$ can be almost one order of magnitude bigger than in this V_L survey, see equation (5.4). Furthermore, in the V_L-parametrization the righthanded neutrino masses are an output. In the example chosen they come out typically bigger (and less degenerate) than the choice made for the $R-$parametrization, eq. (5.6). This pushes downwards further the branching ratio through the log factor, see eq. (4.1). Hence, the two surveys are perfectly consistent.

Of course, the results of this section could be different if the set of $R-$matrices (or V_L and V_R matrices for the V_L-parametrization) is constrained by additional considerations. This is the case of GUT models (as those studied in [26]), where non-trivial correlations can indeed occur.

The last point raises a final question: what happens if leptogenesis constraints are imposed in the scenario? Actually, the impact of θ_{13} on LFV processes was reported to get reinforced once successful leptogenesis is incorporated in the analysis. In the next section, we re-visit the leptogenesis issue.

7 Constraints from leptogenesis

The baryon asymmetry of the universe (BAU) is usually defined as the ratio of the number density of baryons n_B to the number density of photons n_γ. Its present experimental

JHEP03(2011)034

value is [27]

$$\frac{n_B}{n_\gamma} = (6.19 \pm 0.15) \times 10^{-10}. \tag{7.1}$$

Perhaps the most popular mechanism to generate such BAU is nowadays thermal leptogenesis [28], in which a net lepton number is produced by the out-of-equilibrium decay of the (seesaw) right-handed neutrinos (see [29] for a recent review). Then the lepton number is converted into baryon number by sphaleron-mediated processes [30]. Note here that the relevant Lagrangian, defined by the superpotential (2.1), contains the required lepton number and CP violating-terms (the latter are provided by appropriate phases in the $\mathbf{Y}$ matrix).

The final value for the BAU is given by:

$$\frac{n_B}{n_\gamma} = \frac{n_1}{n_\gamma}\, C_{\rm sphal}\, \epsilon\, \eta\,, \tag{7.2}$$

where n_1 is the equilibrium number density of the lightest righthanded neutrino, which is the main responsible for the asymmetry for hierarchical righthanded masses, $M_1 \ll M_2 \ll M_3$; $C_{\rm sphal}$ contains the sphaleron effect, ϵ is the CP-violating contribution to the asymmetry, and η is the efficiency factor, which takes into account the partial erasure of the CP asymmetry by inverse decays and scattering processes. In the minimal supersymmetric standard model eq. (7.2) can be written as [31]

$$\frac{n_B}{n_\gamma} \simeq -1.04 \times 10^{-2}\, \epsilon\, \eta\,. \tag{7.3}$$

The thermal production of righthanded neutrinos is suppressed unless $M_1 \lesssim T_R$, where T_R is the reheating temperature after inflation. On the other hand, T_R cannot be much larger than $10^{10}\,$GeV, to avoid the gravitino problem. In the following we will assume $M_1 \simeq T_R \simeq 10^{10}\,$GeV. In this temperature regime, one or more charged-lepton mass-eigenstates ℓ ($\ell = e, \mu, \tau$) are in equilibrium in the thermal bath, and flavour effects can be significant because the corresponding lepton asymmetries follow an independent evolution [32–34]. However we will not consider flavour effects here, since our main goal in this paper is to examine the dependence of the results on θ_{13}, and to compare the results with the previous literature (where flavor effects were not considered).[2]

In the unflavored case, the efficiency factor, η, is given by [36]

$$\eta = \left[\left(\frac{2(\tilde{m}_e + \tilde{m}_\mu + \tilde{m}_\tau)}{m_*} \right)^{1.16} + \left(\frac{2m_*}{\tilde{m}_e + \tilde{m}_\mu + \tilde{m}_\tau} \right) \right]^{-1}, \tag{7.4}$$

where

$$\tilde{m}_i = |\mathbf{Y}_{1i}|^2 v_u^2 / M_1 \qquad\qquad i = e, \mu, \tau$$
$$m_* = 4\pi v_u^2 H_1 / M_1^2 \sim 10^{-3} eV$$

[2] It is worth mentioning here that in [35] it was shown that successful leptogenesis is possible within the SUSY seesaw for any value of the still unmeasured low energy neutrino parameters (including θ_{13}), taking into account flavour effects and using the V_L - parametrization. This may be an indication that flavour effects are not going to introduce any dramatic dependence on θ_{13}.

JHEP03(2011)034

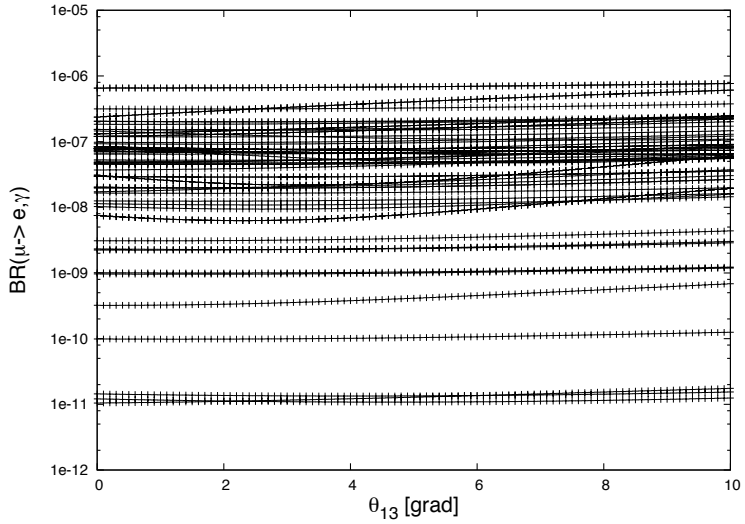

Figure 4. BR($\mu \to e, \gamma$) vs. θ_{13} in $R-$parametrization; including leptogenesis constraint.

$$H_1 = H(T = M_1) = 1.66\sqrt{g_*} M_1^2 / M_{\text{Planck}} \,, \tag{7.5}$$
$$g_*|_{\text{MSSM}} = 228.75 \ ,$$

with H denoting the Hubble parameter. The CP factor, ϵ, is given by [37]:

$$\epsilon = \frac{1}{8\pi} \frac{\sum_{j=\mu,\tau} \text{Im}\{[(\mathbf{Y}\mathbf{Y}^\dagger)_{1j}]^2\} \; g(M_j^2/M_1^2)}{(\mathbf{Y}\mathbf{Y}^\dagger)_{11}} \,, \tag{7.6}$$

where $g(x) = \sqrt{x}\left[\dfrac{2}{1-x} - \ln\dfrac{x+1}{x}\right]$.

Note that both η and ϵ depend on the Yukawa couplings through the combination $\mathbf{Y}\mathbf{Y}^\dagger$, which, in the $R-$parametrization — eq. (3.1) — is independent of U

$$\mathbf{Y}\mathbf{Y}^\dagger = D_{\sqrt{M}} R D_\kappa R^\dagger D_{\sqrt{M}} \ . \tag{7.7}$$

Hence, the BAU, given by (7.3), does not depend on θ_{13}.

Still, it could happen that leptogenesis constraints strengthened the dependence of BR($\mu \to e, \gamma$) on θ_{13}. As we have seen in the previous section, there are some $R-$matrices for which the dependence of $\left(\mathbf{Y}^\dagger\mathbf{Y}\right)_{21}$ (and thus of the branching ratio) on θ_{13} is important. If (in an extreme case) those $R-$matrices were precisely those selected by successful leptogenesis, we would find a strong dependence of the branching ratio on θ_{13} in the complete scenario. To analyze whether this possibility (or a more moderate one) takes really place, it is important to perform a complete scan of the $R-$matrix space. Performing partial scans in this space can be useful to show particular features, but it may introduce unwanted biases: one could artificially select $R-$matrices that lead to strong dependences of BR($\mu \to e, \gamma$) on θ_{13}.

Figure 4 shows the dependence of the BR($\mu \to e, \gamma$) on θ_{13} after imposing successful leptogenesis and scanning R in its whole parameter space. Clearly, no important

JHEP03(2011)034

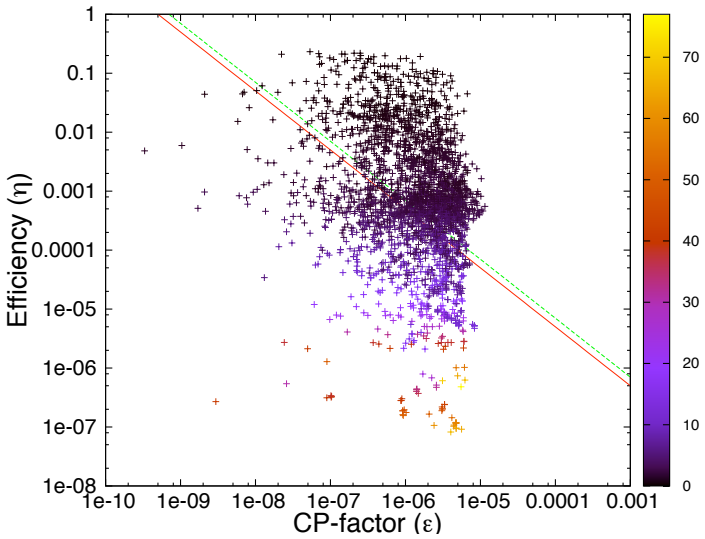

Figure 5. Scatter plot of ϵ and η for random R-matrices, every point represents a different $R-$matrix. The color coordinate represents the average absolute-value of the elements in the first row of R. The red and green lines denote the lower and upper BAU limits, respectively. For clarity in the plot, we have relaxed the allowed BAU window to be $[5-7]\times 10^{-10}$.

dependence on θ_{13} is observed. The trend is very similar to the one with no leptogenesis constraints (figure 3). The conclusion is that leptogenesis constraints do not enhance (or create) any dependence on θ_{13}.

Note that when the leptogenesis constraint is imposed, the values $\mathrm{BR}(\mu \to e,\gamma)$ decrease at least one order of magnitude with respect to the case without leptogenesis, figure 3 (left). This behaviour can be understood from eqs. (7.3), (7.4) and (7.6). The baryon asymmetry depends on the neutrino Yukawa matrix $\mathbf{Y}$ both through the CP asymmetry ϵ and the efficiency factor η. Note from eq. (7.6) that the CP asymmetry is mainly driven by the ν_{R2} and ν_{R3} Yukawa couplings (that is, the second and third rows of R), since the dependence on the ν_{R1} Yukawas approximately cancels out due to the $(\mathbf{Y}\mathbf{Y}^\dagger)_{11}$ factor in the denominator. As a consequence, we find a mild dependence of ϵ on the elements in the first row of R (see figure 4).

The efficiency factor, η, in eq. (7.4) smoothly interpolates between the weak ($\sum_i \tilde{m}_i \ll m_*$) and strong ($\sum_i \tilde{m}_i \gg m_*$) washout regimes. However for all the points in our scans we find that $\sum_i \tilde{m}_i \gg m_*$, thus the efficiency factor is given by

$$\eta \approx \left[\frac{2\sum_i \tilde{m}_i}{m_*}\right]^{-1.16}, \qquad i=e,\mu,\tau\,, \tag{7.8}$$

and it becomes clear that η decreases for larger $\mathbf{Y}_{1i}$, and thus for larger $R-$matrix elements, see eq. (3.1). So, after imposing enough BAU, only those $R-$matrices which are sufficiently small in order to optimize η are selected, thus reducing the final value of the branching ratio.

In figure 5 we have performed a scatter plot showing the values of η and ϵ. The experimental window is also shown for reference. From the figure it is clear that enough

JHEP03(2011)034

BAU is only produced if the elements of the first row in R are smaller than their perturbative bound, in agreement with our previous analytical estimations. This is the reason for the decrease of the branching ratio. Besides, there is no color gradient in the $\epsilon-$direction, which means that the same values of ϵ can be reached for any value of the first row entries of the $R-$matrix. This is in contrast with the case of η, which changes dramatically when varying the typical size of the first row $R-$matrix elements.

8 Conclusions

The main results and conclusions of this paper are the following:

- The somewhat propagated belief that the branching ratio $\mathrm{BR}(\mu \to e, \gamma)$ in supersymmetric seesaw models depends strongly on the value of θ_{13} does not hold after a careful analytical and numerical study. We have analyzed this issue using two alternative parametrizations of the 9 degrees of freedom that, besides the 9 low-energy observables (neutrino masses, mixings and phases), expand the parameter space of the seesaw scenario. This amounts to two alternative ways of traveling across this 9-dimensional space or, in other words, of parametrizing our ignorance. These are called the R-parametrization (section 3.1) and the V_L-parametrization (section 3.2)

- The main potential dependence of $\mathrm{BR}(\mu \to e, \gamma)$ on θ_{13} occurs through the $\mathbf{Y}_\nu^\dagger \mathbf{Y}_\nu$ matrix, where $\mathbf{Y}_\nu$ is the neutrino Yukawa matrix. In the V_L-parametrization, this quantity is trivially insensitive to θ_{13} (or to any observable parameter), so $\mathrm{BR}(\mu \to e, \gamma)$ is. This was already noticed in early papers, as ref. [13]. In the R-parametrization $(\mathbf{Y}_\nu^\dagger \mathbf{Y}_\nu)_{ij}$ seems to have a dependence on θ_{13}, which essentially disappears once the 9-dimensional parameter space is fairly covered. This holds even if the right-handed neutrino masses are kept constant or under control (as is required for succesful leptogenesis), a result which is non-trivial in either parametrization.

- In the R-parametrization (which is the most common in the literature) a fair scan implies to allow all the complex R-matrices compatible with orthogonality and perturbativity of the Yukawa couplings. We give a very simple rule to incorporate the perturbativity of Yukawa couplings as a condition in the entries of the orthogonal R-matrix. It is given by eq. (5.3). We also give (in appendix A) an straightforward procedure to completely scan the space of complex R-matrices in a consistent way with this requirement and the orthogonality one. This procedure can be very useful to avoid possible biases produced by incomplete scans of the seesaw parameter space in the $R-$parametrization.

- Once such scan is performed the branching ratio $\mathrm{BR}(\mu \to e, \gamma)$ gets very insensitive to θ_{13}, as already mentioned. Moreover, the values of the branching ratio are typically larger than the experimental upper bound, which is a very suggesting result. However, one has to keep in mind that if we scanned the $R-$parameter space in a different way (though still covering the whole space) the relative abundance of points with large $\mathrm{BR}(\mu \to e, \gamma)$ might change. In Bayesian language, this is equivalent to use a different

JHEP03(2011)034

prior for the parameter space. The dependence of the typical size of $\mathrm{BR}(\mu \to e, \gamma)$ on the prior is out of the scope of this paper. Nevertheless it is worth noticing that the same prior dependence was implicit in the scatter plots shown in previous literature.

- Including leptogenesis constraints (disregarding flavour effects) in the analysis does not introduce any further dependence of $\mathrm{BR}(\mu \to e, \gamma)$ on θ_{13}. The main impact of leptogenesis, besides remarkably reducing the acceptable volume of the R-parameter-space, is a decrease of $\mathrm{BR}(\mu \to e, \gamma)$ by more than one order of magnitude. This comes from the fact that the efficiency factor, η, decreases for large R-matrix entries. Hence, successful leptogenesis prefers smaller ones, and thus smaller $\mathrm{BR}(\mu \to e, \gamma)$.

As a concluding remark, scanning the parameter space of the $R-$matrix in the full allowed range is necessary in order to make general statements about predictions of the seesaw scenario. This has not been always properly incorporated in former works. In this sense, the procedure exposed in this paper is very easy to implement and can be applied to other physical questions.

Acknowledgments

We thank A. Ibarra for very useful discussions. This work has been partially supported by the MICINN, Spain, under contracts FPA-2007-60252 and FPA-2007-60323; Consolider-Ingenio PAU CSD2007-00060 and MULTIDARK CSD2009-00064. We thank as well the Generalitat Valenciana grants PROMETEO/2009/116 and PROMETEO/2008/069; the Comunidad de Madrid through Proyecto HEPHACOS ESP-1473 and the European Commission under contract PITN-GA-2009-237920. B. Zaldívar acknowledges the financial support of a FPI (MICINN) grant, with reference BES-2008-004688. Also acknowledged is the use of the IFT computation cluster.

A General scan of the $R-$matrix

In this section we explain the details of the scan made on the $R-$matrices, to cover all possibilities compatible with orthogonality, $R^T R = \mathbf{1}$, and the perturbativity condition (5.1), (5.3), which for convenience we repeat here:

$$|R_{ij}|^2 \lesssim \frac{1}{M_i \kappa_j} \ . \tag{A.1}$$

The algorithm presented below has been designed to be easily modified if one considers also leptogenesis constraints.

In general, given a normal hierarchy among neutrinos, $\kappa_1 \ll \kappa_2 \ll \kappa_3$, condition (A.1) tells us that the $R-$matrix elements are allowed to be larger (in absolute value) when you move from bottom-right to top-left in the matrix. Thus, the element R_{33} (R_{11}) presents the smallest (largest) upper bound. On the other hand, orthogonality implies that, in practice, not all the elements of $R-$matrix can reach their corresponding perturbativity limit. Normally, if one sets any entry of the first row (column), at its maximum magnitude, then the

JHEP03(2011)034

corresponding entries in the same column (row) cannot satisfy orthogonality without violating the perturbativity bound (A.1). Conversely, if the matrix elements $R_{22}, R_{23}, R_{32}, R_{33}$, satisfy their perturbativity constraints, then normally the entries of the first row and column would do it as well. Hence, it makes sense to start imposing perturbativity in the bottom-right part of the $R-$matrix. Then the rest is constructed automatically from orthogonality, requiring a final cross-check of the perturbativity condition.

More in detail, using the parametrization (3.2), we see that

$$R_{32}^2 + R_{33}^2 = c_2^2\,,$$

but the perturbativity condition tells us that R_{32}^2 is allowed to be much larger than R_{33}^2, up to phases. So, we can use the perturbativity upper bound on R_{32} to scan c_2

$$c_2 = |c_2|e^{i\phi_2}, \qquad |c_2| \leq \frac{1}{\sqrt{M_3\kappa_2}}, \quad \phi_2 \in [0, 2\pi]. \tag{A.2}$$

Here the phase ϕ_2 (and those appearing below) is assumed to be a random number within its interval. Now, for each value of c_2 we derive s_2 (obviously, up to the sign) and exploit the perturbativity condition on R_{33} to scan c_1:

$$c_1 = |c_1|e^{i\phi_1}, \qquad |c_1| \leq \frac{1}{|c_2|\sqrt{M_3\kappa_3}}, \quad \phi_1 \in [0, 2\pi] \tag{A.3}$$

(again, for each value of c_1 there are two values of s_1). At this point we have used the bounds on R_{32}, R_{33}, and the orthogonality condition, to scan θ_1, θ_2.

Now, we have to scan the third complex angle, θ_3. A convenient way to do it is by using the R_{23} element (recall we prefer to impose perturbativity in the bottom-right part of R). Thus we scan

$$R_{23} = |R_{23}|e^{i\phi_{23}}, \qquad |R_{23}| \leq \frac{1}{\sqrt{M_2\kappa_3}}, \quad \phi_{23} \in [0, 2\pi]\ . \tag{A.4}$$

For each value of R_{23} we derive the two possible values of s_3:

$$s_3 = \frac{s_2 R_{23} c_1 \pm \sqrt{s_1^2(-R_{23}^2 + s_1^2 + c_1^2 s_2^2)}}{c_1^2 s_2^2 + s_1^2}\ . \tag{A.5}$$

Once again, for each value of s_3 there are two of c_3. Finally, we cross-check for each of these values that the corresponding $R-$matrix is indeed consistent with the perturbativity condition. One can do that directly by using equation (5.1) or by checking eq. (A.1) for the remaining entries.

When leptogenesis constraints are included, most of the initially-allowed values for the first-row entries of R become too big, since they lead to a small efficiency factor, η (see section 7). In this case, it pays to constrain from the beginning any of the entries in the first row, e.g. R_{13}. Then, instead of the previous scan in R_{23}, one scans R_{13} as:

$$R_{13} = |R_{13}|e^{i\phi_{13}}, \qquad |R_{13}| \lesssim 1, \quad \phi_{13} \in [0, 2\pi]\ . \tag{A.6}$$

JHEP03(2011)034

Note that this upper bound on $|R_{13}|$ is normally much lower than its perturbativity bound ($\sim 10^2$ in our case), but still is way larger than required by leptogenesis constraints. Now, for each value of R_{13} the value of s_3 is given by

$$s_3 = \frac{R_{13}s_1 \pm \sqrt{c_1^2 s_2^2(-R_{13}^2 + s_1^2 + c_1^2 s_2^2)}}{s_1^2 + c_1^2 s_2 2}\,, \tag{A.7}$$

which replaces eq. (A.5).

As a final comment, recall that the parametrization of R given by eq. (3.2) is completely general up to reflections changing the sign of $\det R$. In our case, however, the scan is completely general since all the relevant physical quantities are invariant under global changes of the sign of R.

B Details of the numerical computations

B.1 $R-$parametrization

In this section we explain the strategy for computing the branching ratio $\mathrm{BR}(\mu \to e, \gamma)$ for each point in the scan of the $R-$matrices (see appendix A).

We have adopted an mSUGRA framework, with universal soft terms at the GUT scale, M_X,

$$(\mathbf{m_L^2})_{ij} = (\mathbf{m_{e_R}^2})_{ij} = m_0 \mathbf{1}, \qquad (\mathbf{A_e})_{ij} = A_0 (\mathbf{Y_e})_{ij}, \tag{B.1}$$

where $\mathbf{m_L^2}$, $\mathbf{m_{e_R}^2}$ and $\mathbf{A_e}$ are the left- and right-handed slepton mass-squared matrices, and the matrix of slepton trilinear couplings. At M_X all the soft terms are diagonal in the basis in which $\mathbf{Y_e}$ is diagonal. Below M_X, the RG running of $\mathbf{m_L^2}$ produces off-diagonal entries, due, essentially, to the contribution proportional to $\mathbf{Y_\nu^\dagger Y_\nu}$. This constitutes the main source of flavor violation.

We work with our own modified version of the SPheno [24] code. The $\mathbf{m_L^2}$ matrix is of special interest since, among the slepton mass matrices it is by far the one that develops larger off-diagonal terms. At the seesaw scale, M, we evaluate $\mathbf{m_L^2}$ as

$$\mathbf{m_L^2} = \mathbf{D_{m_L^2}} - \frac{1}{8\pi^2}(3m_0^2 + A_0^2)\mathbf{Y_\nu^\dagger D_L Y_\nu}\,. \tag{B.2}$$

Here $\mathbf{D_{m_L^2}}$ is the result of running $\mathbf{m_L^2}$ from M_X down to M, switching off the contribution from neutrino Yukawa couplings. The second term in (B.2) is the contribution coming from the neutrino Yukawas, evaluated at the leading-log approximation. This contribution contains the off-diagonal entries of $\mathbf{m_L^2}$. The value of $\mathbf{Y_\nu}$ at the $M-$scale is obtained from the $R-$parametrization formula (3.1) for each point in the scan of the $R-$matrices. Finally, $\mathbf{m_L^2}$ is run down to low-energy (neutrino Yukawas do not play any role in this RG-interval since right-handed neutrinos are decoupled).

The rest of physical quantities (charged slepton mass matrices, gauge couplings, GUT scale, charged lepton yukawas, etc.) are taken directly from SPheno, which imposes the M_X scale to be the one where gauge couplings unify. We also extracted from SPheno the parameters of the neutralinos and charginos. Finally, we followed ref. [3] (implemented in SPheno) to calculate the branching ratio at 1-loop level.

JHEP03(2011)034

B.2 V_L-parametrization

For the V_L-parametrization, we have used the SPheno code as well. However, the original code is not prepared to introduce the initial parameters according to this parametrization. In particular, the original version works with given values of right-handed neutrinos masses, M_i, from the beginning. But in the V_L-parametrization, M_i (and V_R) are obtained at the seesaw scale, M (a suitable average of M_i), from eq. (3.4). On the other hand, the neutrino Yukawa eigenvalues, D_Y and the V_L matrix are indeed initial parameters, defined at the high-scale (and these are the ones in which we perform our scan of the parameter space).

Consequently, we modified the code, incorporating an iterative procedure to determine M_i in a consistent way with all the boundary conditions (at low- and high-scale). In this way, the full $\mathbf{m_L^2}$ matrix is obtained directly from SPheno, and can be used for the computation of BR($\mu \to e, \gamma$).

References

[1] M. Raidal et al., *Flavour physics of leptons and dipole moments*, *Eur. Phys. J.* **C 57** (2008) 13 [arXiv:0801.1826] [SPIRES].

[2] S. Antusch, E. Arganda, M.J. Herrero and A.M. Teixeira, *Impact of θ_{13} on lepton flavour violating processes within SUSY seesaw*, *JHEP* **11** (2006) 090 [hep-ph/0607263] [SPIRES].

[3] J. Hisano, T. Moroi, K. Tobe and M. Yamaguchi, *Lepton-flavor violation via right-handed neutrino Yukawa couplings in supersymmetric standard model*, *Phys. Rev.* **D 53** (1996) 2442 [hep-ph/9510309] [SPIRES].

[4] F. Borzumati and A. Masiero, *Large muon and electron number violations in supergravity theories*, *Phys. Rev. Lett.* **57** (1986) 961 [SPIRES].

[5] J. Hisano and D. Nomura, *Solar and atmospheric neutrino oscillations and lepton flavor violation in supersymmetric models with the right-handed neutrinos*, *Phys. Rev.* **D 59** (1999) 116005 [hep-ph/9810479] [SPIRES].

[6] S. Lavignac, I. Masina and C.A. Savoy, *$\tau \to \mu\gamma$ and $\mu \to e\gamma$ as probes of neutrino mass models*, *Phys. Lett.* **B 520** (2001) 269 [hep-ph/0106245] [SPIRES].

[7] S.T. Petcov and T. Shindou, *Charged lepton decays $l_i \to l_j + \gamma$, leptogenesis CP-violating parameters and Majorana phases*, *Phys. Rev.* **D 74** (2006) 073006 [hep-ph/0605151] [SPIRES].

[8] J. Hisano, M. Nagai, P. Paradisi and Y. Shimizu, *Waiting for $\mu \to e\gamma$ from the MEG experiment*, *JHEP* **12** (2009) 030 [arXiv:0904.2080] [SPIRES].

[9] A. Kageyama, S. Kaneko, N. Shimoyama and M. Tanimoto, *Lepton flavor violating process in degenerate and inverse-hierarchical neutrino models*, *Phys. Lett.* **B 527** (2002) 206 [hep-ph/0110283] [SPIRES].

[10] J.R. Ellis, J. Hisano, M. Raidal and Y. Shimizu, *A new parametrization of the seesaw mechanism and applications in supersymmetric models*, *Phys. Rev.* **D 66** (2002) 115013 [hep-ph/0206110] [SPIRES].

[11] J. Girrbach, S. Mertens, U. Nierste and S. Wiesenfeldt, *Lepton flavour violation in the MSSM*, *JHEP* **05** (2010) 026 [arXiv:0910.2663] [SPIRES].

JHEP03(2011)034

[12] E. Arganda, *Lepton flavour violation in supersymmetric models with seesaw mechanism*, Ph.D. thesis in physics, Universidad Autónoma de Madrid, Madrid Spain (2008).

[13] J.R. Ellis and M. Raidal, *Leptogenesis and the violation of lepton number and CP at low energies*, *Nucl. Phys.* **B 643** (2002) 229 [hep-ph/0206174] [SPIRES].

[14] S.T. Petcov, W. Rodejohann, T. Shindou and Y. Takanishi, *The see-saw mechanism, neutrino Yukawa couplings, LFV decays $l_i \to l_j + \gamma$ and leptogenesis*, *Nucl. Phys.* **B 739** (2006) 208 [hep-ph/0510404] [SPIRES].

[15] A. de Gouvêa, W.-C. Huang and S. Shalgar, *Parameterizing Majorana neutrino couplings in the Higgs sector*, arXiv:1007.3664 [SPIRES].

[16] J.A. Casas and A. Ibarra, *Oscillating neutrinos and $\mu \to e, \gamma$*, *Nucl. Phys.* **B 618** (2001) 171 [hep-ph/0103065] [SPIRES].

[17] S. Davidson and A. Ibarra, *Determining seesaw parameters from weak scale measurements?*, *JHEP* **09** (2001) 013 [hep-ph/0104076] [SPIRES].

[18] J.A. Casas, A. Ibarra and F. Jimenez-Alburquerque, *Hints on the high-energy seesaw mechanism from the low-energy neutrino spectrum*, *JHEP* **04** (2007) 064 [hep-ph/0612289] [SPIRES].

[19] J.N. Esteves et al., *Flavour violation at the LHC: type-I versus type-II seesaw in minimal supergravity*, *JHEP* **05** (2009) 003 [arXiv:0903.1408] [SPIRES].

[20] N. Haba, S. Matsumoto and K. Yoshioka, *Observable seesaw and its collider signatures*, *Phys. Lett.* **B 677** (2009) 291 [arXiv:0901.4596] [SPIRES].

[21] S. Pascoli, S.T. Petcov and C.E. Yaguna, *Quasi-degenerate neutrino mass spectrum, $\mu \to e + \gamma$ decay and leptogenesis*, *Phys. Lett.* **B 564** (2003) 241 [hep-ph/0301095] [SPIRES].

[22] W. Buchmüller, P. Di Bari and M. Plümacher, *The neutrino mass window for baryogenesis*, *Nucl. Phys.* **B 665** (2003) 445 [hep-ph/0302092] [SPIRES].

[23] F. Deppisch, H. Pas, A. Redelbach and R. Ruckl, *Constraints on SUSY seesaw parameters from leptogenesis and lepton flavor violation*, *Phys. Rev.* **D 73** (2006) 033004 [hep-ph/0511062] [SPIRES].

[24] W. Porod, *SPheno, a program for calculating supersymmetric spectra, SUSY particle decays and SUSY particle production at e^+e^- colliders*, *Comput. Phys. Commun.* **153** (2003) 275 [hep-ph/0301101] [SPIRES].

[25] D.M. Pierce, J.A. Bagger, K.T. Matchev and R.-j. Zhang, *Precision corrections in the minimal supersymmetric standard model*, *Nucl. Phys.* **B 491** (1997) 3 [hep-ph/9606211] [SPIRES].

[26] A. Masiero, S.K. Vempati and O. Vives, *Massive neutrinos and flavour violation*, *New J. Phys.* **6** (2004) 202 [hep-ph/0407325] [SPIRES].

[27] WMAP collaboration, E. Komatsu et al., *Seven-year Wilkinson Microwave Anisotropy Probe (WMAP) observations: cosmological interpretation*, *Astrophys. J. Suppl.* **192** (2011) 18 [arXiv:1001.4538] [SPIRES].

[28] M. Fukugita and T. Yanagida, *Baryogenesis without grand unification*, *Phys. Lett.* **B 174** (1986) 45 [SPIRES].

[29] S. Davidson, E. Nardi and Y. Nir, *Leptogenesis*, *Phys. Rept.* **466** (2008) 105 [arXiv:0802.2962] [SPIRES].

JHEP03(2011)034

[30] V.A. Kuzmin, V.A. Rubakov and M.E. Shaposhnikov, *On the anomalous electroweak baryon number nonconservation in the early universe*, *Phys. Lett.* **B 155** (1985) 36 [SPIRES].

[31] G.F. Giudice, A. Notari, M. Raidal, A. Riotto and A. Strumia, *Towards a complete theory of thermal leptogenesis in the SM and MSSM*, *Nucl. Phys.* **B 685** (2004) 89 [hep-ph/0310123] [SPIRES].

[32] A. Abada, S. Davidson, F.-X. Josse-Michaux, M. Losada and A. Riotto, *Flavour issues in leptogenesis*, *JCAP* **04** (2006) 004 [hep-ph/0601083] [SPIRES].

[33] E. Nardi, Y. Nir, E. Roulet and J. Racker, *The importance of flavor in leptogenesis*, *JHEP* **01** (2006) 164 [hep-ph/0601084] [SPIRES].

[34] A. Abada et al., *Flavour matters in leptogenesis*, *JHEP* **09** (2006) 010 [hep-ph/0605281] [SPIRES].

[35] S. Davidson, J. Garayoa, F. Palorini and N. Rius, *CP violation in the SUSY seesaw: leptogenesis and low energy*, *JHEP* **09** (2008) 053 [arXiv:0806.2832] [SPIRES].

[36] W. Buchmüller, P. Di Bari and M. Plümacher, *Leptogenesis for pedestrians*, *Ann. Phys.* **315** (2005) 305 [hep-ph/0401240] [SPIRES].

[37] L. Covi, E. Roulet and F. Vissani, *CP violating decays in leptogenesis scenarios*, *Phys. Lett.* **B 384** (1996) 169 [hep-ph/9605319] [SPIRES].

JHEP03(2011)034

CHAPTER 5

COLLIDER BOUNDS ON DARK MATTER

Journal of Cosmology and Astroparticle Physics
An IOP and SISSA journal

When LEP and Tevatron combined with WMAP and XENON100 shed light on the nature of dark matter

Yann Mambrini[a] **and Bryan Zaldívar**[b]

[a]Laboratoire de Physique Théorique, Université Paris-Sud, F-91405 Orsay, France
[b]Instituto de Fisica Teorica, IFT-UAM/CSIC, Nicolas Cabrera 15, UAM Cantoblanco, 28049 Madrid, Spain

E-mail: Yann.Mambrini@th.u-psud.fr, Bryan.Zaldivar@uam.es

Received July 18, 2011
Accepted October 2, 2011
Published October 18, 2011

Abstract. Recently, several astrophysical data or would-be signals has been observed in different dark-matter oriented experiments. In each case, one could fit the data at the price of specific nature of the coupling between the Standard Model (SM) particles and a light Dark Matter candidate: hadrophobic (INTEGRAL, PAMELA) or leptophobic (WMAP Haze, dijet anomalies of CDF, FERMI Galactic Center observation). In this work, we show that when one takes into account the more recent LEP and Tevatron analysis, a light thermal fermionic Dark Matter ($\lesssim 10\,\mathrm{GeV}$) that couples to electrons is mainly ruled out if one combines the analysis with WMAP constraints. We also study the special case of scalar dark matter, using a single-photon events simulation to constrain the coupling of dark matter to electron.

Keywords: dark matter theory, dark matter experiments, cosmology of theories beyond the SM

JCAP10(2011)023

doi:10.1088/1475-7516/2011/10/023

Contents

JCAP10(2011)023

1 Introduction

Very recently, the CDF collaboration announced the observation of an excess of events which include a lepton (electron or muon), missing transverse energy, and two jets [1]. Many studies have been done since then motivating the existence of light dark matter candidates (see e.g., [2]). Some authors [3] interpreted this excess by the introduction of a new gauge boson with sizable couplings to quarks, but with no or highly suppressed couplings to leptons (a *leptophobic* dark boson). Dark matter experiments had also given some hints for signals in direct or indirect detection modes. On one hand, some hadrophobic dark matter candidates were proposed in [4–6] to explain the DAMA [7] and CoGENT [8] signals even if contradicted by the authors of [9, 10]. On the other hand, some authors showed that a light dark matter could at the same time explain these direct detection signals and the excess of emission observed by the Fermi Gamma Ray Space telescope [11] and the CDF signal if it annihilate predominantly into hadronic states. There was also cosmic rays excess measured in PAMELA or INTEGRAL [12] which needed hadrophobic dark matter.[1] In each case the nature of the couplings of the dark matter with the Standard Model particles is fundamental in any kind of discoveries. Recently, the authors of [14] used the single-photon events at LEP to constraint the nature of the dark matter couplings, concluding that a dark matter with mass $\lesssim 10\,\mathrm{GeV}$ with charged-leptonic couplings generates a too low annihilation rate to avoid the over-closure of the Universe. In this work, we compute the rate of hadronic coupling needed to reconciliate the LEP analysis with a thermal dark matter hypothesis and respect WMAP upper bound constraint. In section II, we will review the models and type of couplings we have studied. We give our result in the case of contact operator for a fermionic candidate in section IIIA, and consider a scalar case in section IIIB. For the later, we ran a simulation of events at DELPHI experiment [15] in order to constraint the operator suppression scale, in the same fashion as is done in the literature for the fermionic DM. We then implement the constraints

[1] A recent alternative explanation for these signals are given in [13], in which composite dark matter (dark atoms) is considered.

from the mono-jet event of Tevatron and XENON100 in the analysis in section IV before concluding in section V.

2 The models

We begin with the case of a fermionic WIMP, and study the 4 types of interactions consistent with the requirement of Lorentz invariance and strongly constrained by LEP analysis. This enables us to describe the interaction between WIMPs and standard model fermions in terms of an effective field theory, in which we keep only the first term in the expansion of the heavy propagator. However, contrarily to the description in [14] which was concerned by the leptonic constraints, we generalize the analysis taking into account 1) the neutrino couplings and 2) the possibility of hadronic tree level couplings. This implies the introduction of a second effective scale, Λ_h. Indeed there is no reason for the effective hadronic breaking scale to be the same than the leptonic one Λ_l. We will thus introduce hadronic and leptonic coupling constants g_h and g_l, such as

$$\frac{1}{\Lambda_l} \equiv \frac{\sqrt{g_l}}{\Lambda}; \qquad \frac{1}{\Lambda_h} \equiv \frac{\sqrt{g_h}}{\Lambda} \tag{2.1}$$

We will then consider the set of operators

$$\begin{aligned}
\text{Vector}: \quad & \mathcal{L}_V = \sum_i \frac{g_l^i}{\Lambda^2}(\bar{l}^i\gamma^\mu l^i)(\bar{\chi}\gamma_\mu\chi) + \sum_i \frac{g_h^i}{\Lambda^2}(\bar{q}^i\gamma^\mu q^i)(\bar{\chi}\gamma_\mu\chi) \\
\text{Scalar, s}-\text{channel}: \quad & \mathcal{L}_S = \sum_i \frac{g_l^i}{\Lambda^2}(\bar{l}^i l^i)(\bar{\chi}\chi) + \sum_i \frac{g_h^i}{\Lambda^2}(\bar{q}^i q^i)(\bar{\chi}\chi) \\
\text{Axial}: \quad & \mathcal{L}_A = \sum_i \frac{g_l^i}{\Lambda^2}(\bar{l}^i\gamma^\mu\gamma^5 l^i)(\bar{\chi}\gamma_\mu\gamma^5\chi) + \sum_i \frac{g_h^i}{\Lambda^2}(\bar{q}^i\gamma^\mu\gamma^5 q^i)(\bar{\chi}\gamma_\mu\gamma^5\chi) \\
\text{Scalar, t}-\text{channel}: \quad & \mathcal{L}_t = \sum_i \frac{g_l^i}{\Lambda^2}(\bar{l}^i\chi)(\bar{\chi}l^i) + \sum_i \frac{g_h^i}{\Lambda^2}(\bar{q}^i\chi)(\bar{\chi}q^i)
\end{aligned} \tag{2.2}$$

χ being the DM candidate. Throughout this paper, we will assume that the dark matter particle χ is a Dirac fermion (except in section IIIB, where we consider a real scalar DM candidate). A vectorial interaction is motivated by the exchange of a Z'_μ [16] whereas scalar interaction is motivated by Higgs-portal like models [17].

We will consider 3 kinds of models which could be representative of UV completion:

- Electrophilic couplings (model A): $g_l^e = g_e$, $g_l^{i=\mu,\tau,\nu_i} = 0$
- Charged lepton couplings (model B) : $g_l^{i=e,\mu,\tau} = g_l$, $g_l^{i=\nu_i} = 0$
- Universal lepton couplings (model C) : $g_l^{i=e,\mu,\tau,\nu_i} = g_l$

As we are interested in the ratio of the hadronic to the leptonic final states in the DM annihilation, we will consider without loss of generality an universal generation/family coupling in the hadronic sector: $g_h^{i=u,d,c,s,b,t} = g_h$. Note that we assumed lepton flavor to be conserved in the dark matter interaction.

Recently, the authors of [14] made an analysis with relatively little model dependance, by pair production of pair of dark matter particles in association with a hard photon. The

JCAP10(2011)023

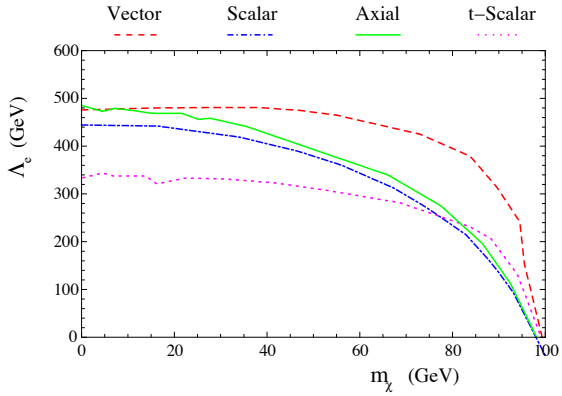

Figure 1. DELPHI lower limit on $\Lambda_e \equiv \Lambda/\sqrt{g_e}$ as a function of the dark matter mass for the different types of couplings: vector (red dashed), scalar (blue dashed-dotted), axial (green full-line) and t-channel scalar (magenta dotted).

LEP experiments have searched for anomalous single-photon events in their data sets, but have found no discrepancy from the prediction of the standard model. They used the single-photon spectrum from the DELPHI experiment to place upper bound to $1/\Lambda_e^2 = g_e/\Lambda^2$. We reproduce interpolated functions of this result in figure (1). We then translated this limit on Λ_e to a limit on the ratio of hadronic to leptonic channel, $\mathrm{Br_h}/\mathrm{Br_l}$, taking into account the relic density constraints.

3 Constraints from the thermal relic to the hadronic branching ratio

3.1 The fermionic case

The LEP lower bound on the scale $\Lambda_e = \Lambda/\sqrt{g_e}$ can be converted in a upper bound to the dark matter annihilation into e^+e^- (case A), into charged leptons pair (case B) or into general leptons pair (case C). Moreover, if dark matter is a thermal relic, asking for the density to respect the upper bound given by WMAP [19] $\Omega_\chi h^2 \lesssim 0.1$, one needs to impose[2] $\langle\sigma v\rangle \gtrsim 3\times10^{-26}\mathrm{cm^3 s^{-1}} \simeq 1$ pb to avoid an overclosed universe (but letting for the possibility of having another dark matter candidate). We computed the annihilation cross section which is given for a final state with particles masses m_3, m_4 by

$$\frac{d\sigma_\mathrm{I}}{d\Omega} = \frac{|\mathcal{M}_\mathrm{I}|^2}{64\pi^2 s}\frac{\sqrt{s-2m_3^2-2m_4^2+\frac{(m_3^2-m_4^2)^2}{s}}}{\sqrt{s-4m_\chi^2}} \tag{3.1}$$

with I=V, S, A, t. We then substitute $s = 4m^2/(1-v^2/4) \simeq 4m_\chi^4 + m_\chi^2 v^2$ in eq. (3.1) and expanding in powers of the relative velocity between two annihilating WIMPs up to order v^2 for each type of couplings. We find

$$\sigma_I^J v = g_l^2 \sum_{l=e,\mu,\tau,\nu} \sigma_{I,l}^J v + c\, g_h^2 \sum_{h=u,d,c,s,t,b} \sigma_{I,h}^J v \tag{3.2}$$

where I=V, S, A, t represents the nature of the coupling (vectorial, scalar, axial or t-scalar) and J=A, B, C the type of coupling (electronic, charged leptonic or universal leptonic), c the

[2]In the absence of resonances or coannihilation.

JCAP10(2011)023

color factor and

$$\begin{aligned}
\sigma^J_{Ik} v &= \sigma_{I,k} v \times \theta^J_k(m_\chi) \\
\theta^{J=A,B,C}_{h=u,d,c,s,t,b}(m_\chi) &= \Theta_H(m_\chi - m_h) \\
\theta^A_e(m_\chi) &= \Theta_H(m_\chi - m_e), \qquad & \theta^A_{l=\mu,\tau,\nu}(m_\chi) &= 0 \\
\theta^B_{l=e,\mu,\tau}(m_\chi) &= \Theta_H(m_\chi - m_l), \qquad & \theta^B_{l=\nu}(m_{m_\chi}) &= 0 \\
\theta^C_{l=e,\mu,\tau,\nu}(m_\chi) &= \Theta_H(m_\chi - m_l)
\end{aligned} \tag{3.3}$$

Θ_H being the classical heaviside function ($\Theta_H(x) = 1$ if $x > 0$, and 0 otherwise) and $\sigma_{I,k}$ is given by:

$$\begin{aligned}
\sigma_{V,k} v &= 4 g_\Lambda \left(24(2m_\chi^2 + m_k^2) + \frac{8m_\chi^4 - 4m_\chi^2 m_k^2 + 5m_k^4}{m_\chi^2 - m_l^2} v^2 \right) \\
\sigma_{S,k} v &= 24 g_\Lambda (m_\chi^2 - m_k^2) v^2 \\
\sigma_{A,k} v &= 4 g_\Lambda \left(24 m_k^2 + \frac{8m_\chi^4 - 22 m_\chi^2 m_k^2 + 17 m_k^4}{m_\chi^2 - m_k^2} v^2 \right) \\
\sigma_{t,k} v &= g_\Lambda \left(24(m_\chi + m_k)^2 + \frac{(m_\chi + m_k)^2 (8m_\chi^2 - 16 m_\chi m_k + 11 m_k^2)}{m_\chi^2 - m_k^2} v^2 \right)
\end{aligned} \tag{3.4}$$

with $g_\Lambda = \frac{\sqrt{1 - m_k^2/m_\chi^2}}{192\pi\Lambda^4}$.

The LEP constraint on $\Lambda_e = \Lambda/\sqrt{g_e}$ gives a maximum value for the leptonic annihilation cross section $\sigma_l^{\max}$ for each type of couplings we considered (A, B and C, see figure 1). This maximum value of the leptonic cross-section give a lower bound on $\Omega_\chi h^2$: one thus can calculate the hadronic contribution needed to satisfy WMAP upper bound limit ($\Omega_\chi h^2 \lesssim 0.1$) corresponding to the thermal condition $\sigma v \gtrsim 3 \times 10^{-26} \mathrm{cm}^3/\mathrm{s}$. This can be summarize by:

$$\sigma_l^{\max} v + \sigma_h^{\max} v \gtrsim 3 \times 10^{-26} \mathrm{cm}^3 \mathrm{s}^{-1} \simeq 2.5 \times 10^{-9}\ \mathrm{GeV}^{-2} \tag{3.5}$$

As an example, we can analytically evaluate the order of magnitude for the hadronic branching ratio Br_h/Br_l we expect for a dark matter mass $m_\chi \simeq 5\,\mathrm{GeV}$ in the case of an electronic (case A) vector-like coupling ($\mathcal{L}_V$). We combined the condition given in eq. (3.5) to the value of $\sigma_V v$ computed through eq. (3.4) with the value of Λ_e obtained by LEP (see figure 1): $\Lambda_{eV}^{\max} \simeq 480\,\mathrm{GeV}$ for $m_\chi \simeq 5\,\mathrm{GeV}$. Neglecting $m_{l,h} \ll m_\chi$, in the electronic-type coupling, one can simplify $\sigma_V v \simeq \frac{m_\chi^2}{\pi\Lambda_e^4}(1 + Br_h/Br_l) \gtrsim 2.5 \times 10^{-9}$ which gives $Br_h/Br_l \gtrsim \frac{(\Lambda_e^{\max})^4 \pi}{m_\chi^2} 2.5 \times 10^{-9} \simeq 16$. This corresponds to a 94% annihilation rate to hadronic states. Of course, we ran the analysis with the complete formulation for the cross sections and the results are shown in figure 2. One can see that whatever is the nature of the coupling (electronic, charged-leptonic or universal leptonic), a dark matter of mass $m_\chi \simeq 10\,\mathrm{GeV}$ has a very strong hadronic component in its annihilation final state, in the case of scalar and axial interactions (above 90%). On the other hand, for vector and t-scalar interactions, the nature of the coupling plays an important role, being an hadronic component as large as 80% in one case (electronic coupling), or a 0% (i.e. no need of hadronic channel) in other case (universal leptonic), for a vector interaction for example. These behaviors can be understood

JCAP10(2011)023

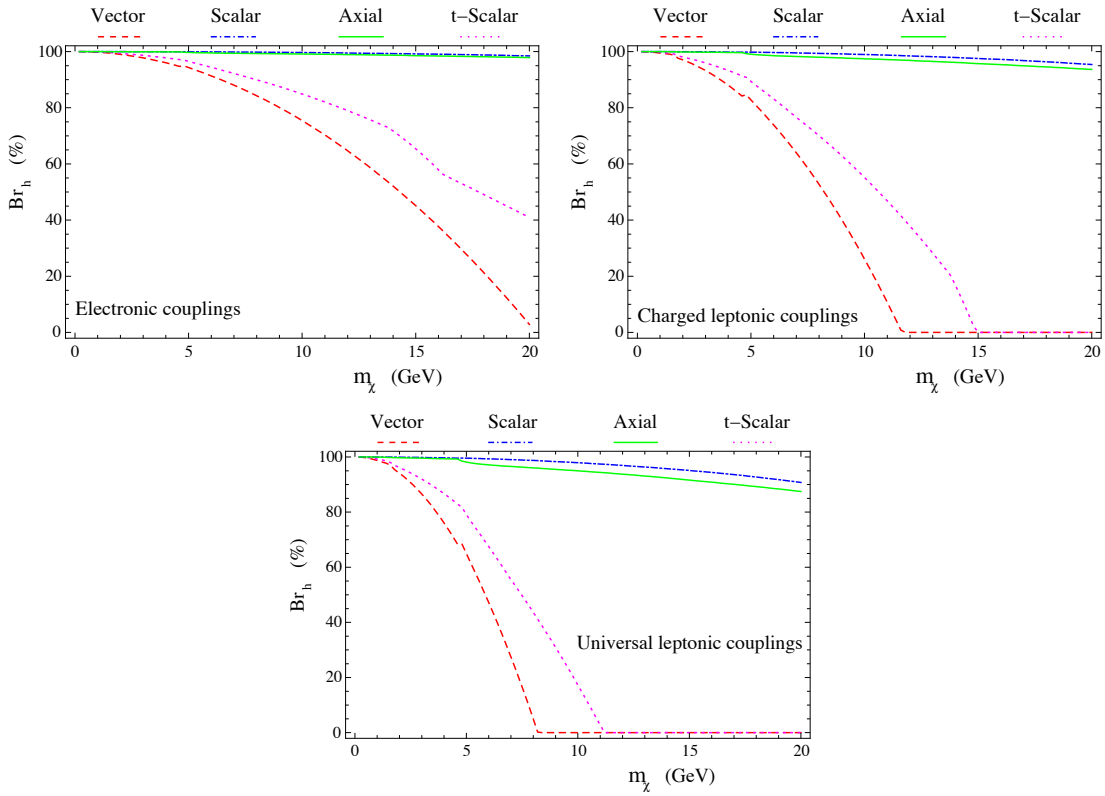

Figure 2. Minimum hadronic branching ratio needed to respect WMAP upper bound in the case of electronic couplings (model A, top left), charged-leptonic couplings (model B, top right) and universal-leptonic couplings (model C, bottom) with 4 different types of interactions: vector (red dashed), scalar (blue dashed-dotted), axial (green full-line) and t-channel scalar (magenta dotted). Bounds coming from LEP constraints on leptonic couplings.

JCAP10(2011)023

from expressions (3.4), where the scalar and axial interactions are suppressed by the velocity and the leptonic masses, respectively. As a consequence one needs a much larger hadronic contribution to ensure a relic abundance below the WMAP limit and avoid the over-closure of the Universe. However for the vector and t-scalar interactions there is no such suppression, so leading to possible large contributions coming only from the leptonic couplings. One can notice the presence of small "kinks" in the branching fraction corresponding to the kinetic opening/closing of the different annihilation channels.

We also observe that, paradoxically, the more electrophilic are the dark matter couplings (model A), the more hadrophilic it should also be. Indeed, because there are no possibility to fulfill the relic abundance constraints with charged lepton or neutrino channels and the hadronic final states become thus the dominant ones. In the charged leptonic and universal leptonic models (B and C), there exists a threshold mass with a null hadronic branching ratio: this corresponds to the mass for which the hadronic components of the annihilation rate are not anymore necessary (but can be present) to fulfill the relic density constraints. The leptonic channels are sufficient to avoid the relic overabundance for a DM mass above this threshold.

3.2 Scalar case

We also checked the case of a scalar dark matter. It could not be obvious at the first sight that we can apply the same analysis. In fact, we need to introduce a new scale Λ_S. We will consider a real scalar dark matter, which is produced via the following scalar-type effective operator:

$$\mathcal{L}_e^S = \frac{g_e}{\Lambda_S}\chi\chi\bar{e}e \ . \tag{3.6}$$

In an analogous procedure as the one done above for a fermionic candidate, we derive limits on the suppression scale Λ_S/g_e from single-photon signals in the DELPHI experiment at LEP. We assumed for simplicity that all data was taken at an energy of 100 GeV per beam. We used MadGraph/MadEvent [20] to simulate the distribution of number of events with photon energy E_γ. The background process $e^+e^- \to \gamma\nu\bar{\nu}$ was taken directly from the simulation done by [14]. On the other hand, the signal process $e^+e^- \to \gamma\chi\chi$ was studied assuming the following kinematical cuts: $E_\gamma > 6\,\text{GeV}$, and a photon rapidity $\eta_\gamma > 2.5$. We realize that these constraints are less restrictive than in the fermionic case, so in principle the bounds on Λ_S could be different if using those more rigorous cuts. To quantify this difference, we reproduced the bounds on Λ_e coming from a signal due to a fermionic dark matter, and a vector-like effective operator, and compare it directly with the result shown in figure 1. The result, shown in figure 3-top, is a $\chi^2/\text{d.o.f.} = 5.12/8$, which means a small difference of our case with respect to the more correct result of [14]. We include as an example of a scalar dark matter signal, the simulation of a $m_\chi = 10\,\text{GeV}$ case, with a suppression scale $\Lambda_S/g_e = 300\,\text{GeV}$, using the DELPHI luminosity of 650 pb^{-1}, shown in figure 3-bottom. We can extract from the above analysis that, for example, a scalar dark matter of $m_X = 10\,\text{GeV}$ needs a suppression scale $\Lambda_S \gtrsim 520\,\text{GeV}$, in order to be compatible with LEP bounds.

After computing the production cross section for the fermionic dark matter (σ_f^P) and bosonic one (σ_s^P) one can show that, in the limit of $s \gg m_\chi$ (which is the case in our analysis) we obtained

$$\sigma_f^P \sim \frac{g_e^2}{\Lambda^4}\frac{s}{16\pi} \qquad \text{and} \qquad \sigma_s^P \sim \frac{g_e^2}{\Lambda_S^2}\frac{1}{32\pi} \tag{3.7}$$

We thus observe that if we define $\Lambda_S \equiv \Lambda^2/\sqrt{2s}$ we can deduce the lower limit on Λ_S from the lower limit on Λ (see figure 1). If imposing $\sigma_f^P \approx \sigma_s^P$, taking a dark matter candidate with mass of 10 GeV, we deduce from the above expressions the lower bound $\Lambda_S \gtrsim 815\,\text{GeV}$. However from figure (3) we obtained $\Lambda_S \gtrsim 520\,\text{GeV}$, which implies that in fact $\sigma_s^P \approx 2.45\sigma_f^P$.

With this bounds on Λ_S, one could in principle try to deduce bounds on the amount of hadronic channel from DM annihilation, as we did above for the fermionic case. The expression for the annihilation cross-section $\sigma_S^s v$ of a scalar DM with a scalar interaction, into an electron-positron pair is:

$$\sigma_{S,e}^s v \equiv g_e^2\tilde{\sigma}_{S,e}^s v \simeq \frac{g_e^2}{4\pi\Lambda_S^2}\left(1-\frac{m_e^2}{m_\chi^2}\right)^{3/2} + \frac{g_e^2}{32\pi\Lambda_S^2}v^2 \ . \tag{3.8}$$

Unfortunately, this single channel already gives, for $510 \lesssim \Lambda_S/g_e \lesssim 520\text{GeV}$ and $1 \lesssim m_\chi \lesssim 20\text{GeV}$ (as in figure 3) a cross-section $\sigma_S^s v \simeq 10^{-24}\text{cm}^3/\text{s}$, with negligible dependence on m_χ. Being $\sigma_S^s v \gg 3\times 10^{-26}$, there is in principle no need for hadronic channel. We conclude that LEP bounds are insufficient to constrain the nature of couplings in the case of scalar DM. A

JCAP10(2011)023

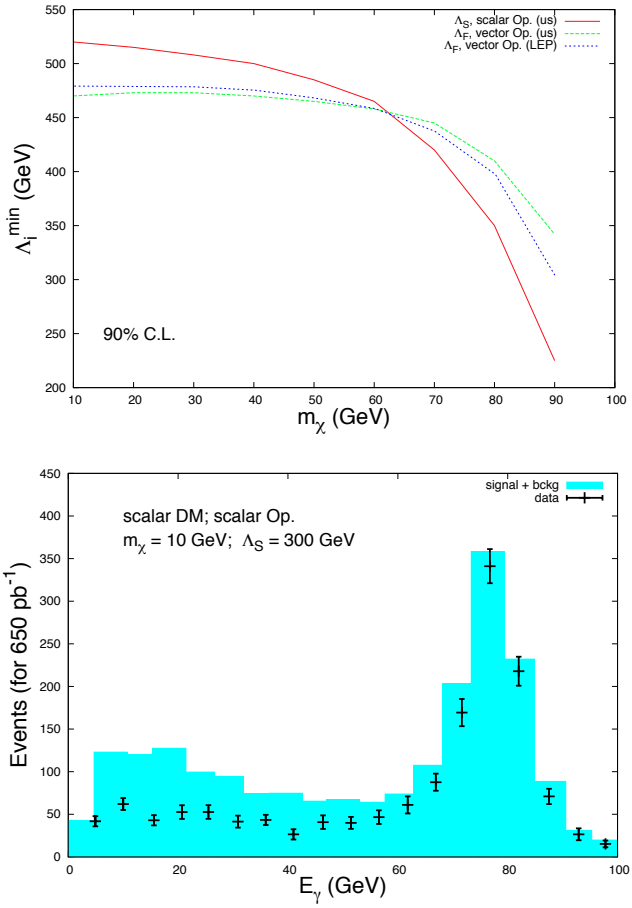

Figure 3. (top). Lower limits on Λ_S/g_e (solid-red) coming from DELPHI experiment [15], at a 90% C.L. For reference, the resulting limits on $\Lambda/\sqrt{g_e}$ (fermionic dark matter) coming from a vector-like effective operator, using the same cuts as before, are shown (dashed-green), to be compared with the correspondent result shown in figure 1, here in (dotted-blue). (bottom) Distribution of photon energies in single-photon events at DELPHI. The histogram shows the signal+background coming from a hypothetical scalar dark matter, as in (3.6), with mass $m_\chi = 10\,\text{GeV}$, and a suppression scale $\Lambda_S/g_e = 300\,\text{GeV}$. See body text.

similar conclusion holds for the Tevatron bounds, if considering the total cross-section

$$\sigma_S^s v = g_l^2 \sum_{l=e,\mu,\tau,\nu} \tilde{\sigma}_{S,l}^s v + c g_h^2 \sum_{h=u,d,c,s,t,b} \tilde{\sigma}_{S,h}^s v \tag{3.9}$$

and the lower limits shown in figure 4. It turns out that the scale Λ_S/g_e above which $\sigma_S^s v$ starts to be of the order of the thermal relic one, is around 5 TeV. So in principle the LHC would be able to constrain the nature of couplings and interactions of a scalar DM candidate.

4 Complementarity with other experiments

4.1 Fitting with WMAP

To run a more precise analysis, we decided to implement the contact coupling lagrangian into CompHEP and micromegas [21] for the different type of interactions (vectorial, scalar and

JCAP10(2011)023

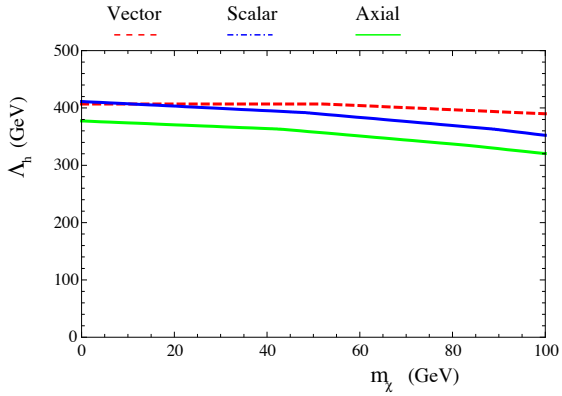

Figure 4. CDF lower limit on $\Lambda_h \equiv \Lambda/\sqrt{g_h}$ as a function of the dark matter mass for the different types of couplings: vector (red dashed), scalar (blue dashed-dotted) and axial (green full-line).

axial) in the fermionic DM case. We then applied the last 5σ constraint on the relic density from WMAP experiment [19], $\Omega_{\rm WMAP}h^2 = 0.1123 \pm 0.0175$ and ran a scan on the parameter space of the model (Λ_l, Λ_h, m_χ) keeping only the points respecting both astrophysical and accelerator constraints. We can understand easily that in order to respect WMAP upper bounds, the hadronic contribution depends on the type of interactions. After a look at figure 2, we decided to consider the most and the less conservative cases, which are the universal-leptonic coupling for vector-like interaction, and the electronic coupling for scalar-like interaction, respectively. The results are shown in figures 5 and 6. We see that WMAP forbids a dark matter with hadrophilic couplings ($g_h/g_e \gtrsim 10$) of $m_\chi \gtrsim 5\,\text{GeV}$ for a vector interaction, and $m_\chi \gtrsim 10\,\text{GeV}$ for a scalar interaction. For such values of hadronic couplings, $\Omega h^2 \lesssim \Omega_{\rm WMAP}h^2$. When combined with LEP analysis, a large part of the parameter space with small g_h/g_e is excluded because of the non-observation of mono-photon events at LEP (which implies an upper bound on g_e). Whereas it excludes a broad region of the parameter space for a dark matter mass $m_\chi \lesssim 11\,\text{GeV}$ in the vectorial case (in total agreement with figure6 of [14]) it completely exclude leptophilic ($g_h/g_e \lesssim 0.1$) dark matter with the scalar-like interaction. Combining these limits with the recent Tevatron analysis restricted even further the parameter space.

4.2 Tevatron constraints

Last year, the authors of [22, 23] made a similar analysis searching for mono-jet events for the Tevatron. These non-discovery of any events of this kind can be translated into a lower bound on $\Lambda_h \equiv \Lambda/\sqrt{g_h}$ which depend on the nature of the coupling and is represented in figure 4.

Contrarily to the LEP analysis, the center of mass energy does not limit the lower bound on Λ_h for $m_\chi \lesssim 100\,\text{GeV}$. We have only plotted the limit on the up-type coupling, which is the one we used through the paper to stay as conservative as possible (limits of down or charm-type couplings on Λ_h are a factor 3 and 10 lower respectively [22]). We can easily understand how the Tevatron constraint imply some strong tensions when combined with WMAP and LEP analysis. Indeed, to reconciliate LEP constraints with WMAP we needed to increase the hadronic contribution (and thus, the coupling to quarks) in the annihilation process. This then enters in conflict with the limit from the non-observation of mono-jet excess at Tevatron. To keep the logic of the work and keep a conservative analysis, we considered universal leptonic couplings (implying a smaller hadronic contribution to respect WMAP

JCAP10(2011)023

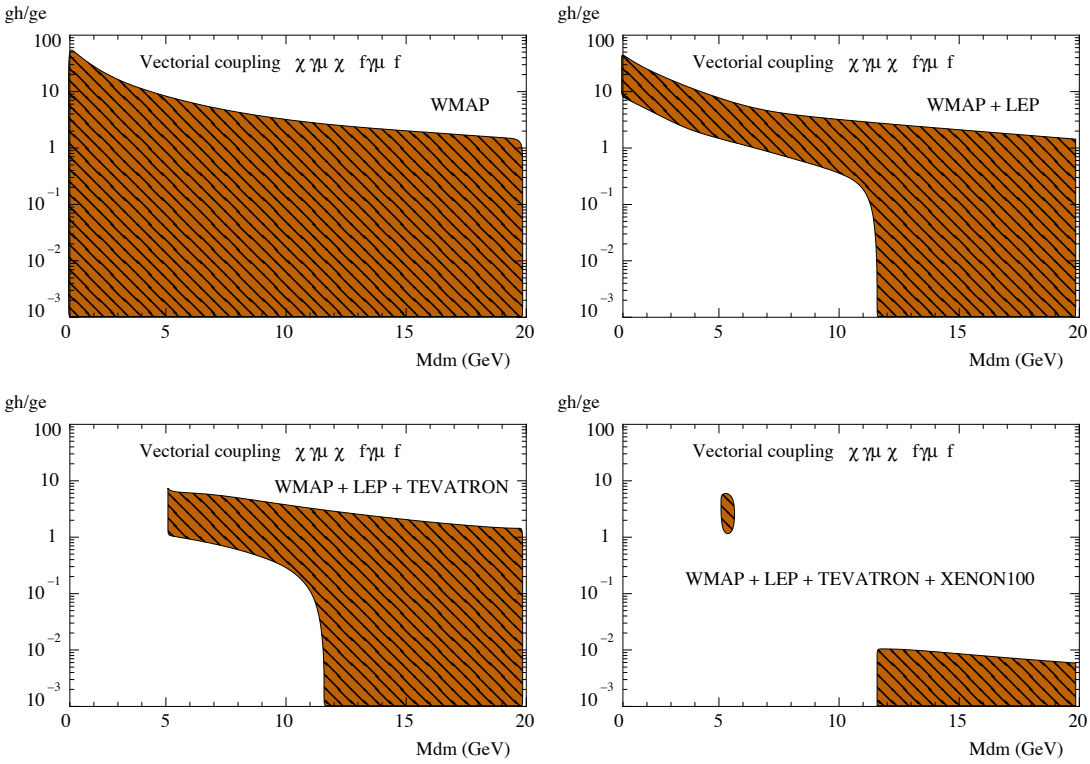

Figure 5. Hadronic ratio coupling for the annihilation of dark matter as function of the dark matter mass in the case of universal-leptonic couplings for a vector-like interaction after a scan on Λ_e and Λ_h. After applying the constraint of WMAP (top left) mono-jet events from LEP, Tevatron and XENON100 constraint (bottom right). See the text for details.

upper bound). The results are shown in figures 5 and 6. Confirming the conclusions of [22]: for a vector-like coupling the Tevatron bound is the more stringent for dark matter mass below 5 GeV. Indeed, for such low mass, the hadronic branching ratio needed to respect in the meantime WMAP and LEP would produce a clear excess in mono-jet events at Tevatron and would have been observed. The Tevatron constraints are even more impressive for a scalar-like couplings, where all the parameter space allowed by the combined WMAP and LEP analysis is excluded by Tevatron data (figure 6).

4.3 XENON100 constraint

Recently, the XENON100 collaboration has released several analysis claiming for no detection signal of dark matter [24]. Their results are by far the more constraining one in the field of direct detection experiments. One can easily understand that XENON100 is adding new tensions when combined with WMAP, LEP and Tevatron bounds. Indeed, the hadronic branching fraction required to avoid the overproduction of dark matter in the early universe could enter in conflict not only with Tevatron results but also with XENON100 exclusion limits. Indeed, whereas the s-channel dark matter production $qq \to \chi\chi g$ is the process constraining Λ_h at Tevatron, the nuclear recoil gives bound to Λ_h (and thus g_h/g_e) through the t-channel process $\chi q \to \chi q$. As we can see in figure 5, XENON100 restrict even a larger part of the parameter space for $m_\chi \gtrsim 6\,\mathrm{GeV}$ (which would not have been the case if we took

JCAP10(2011)023

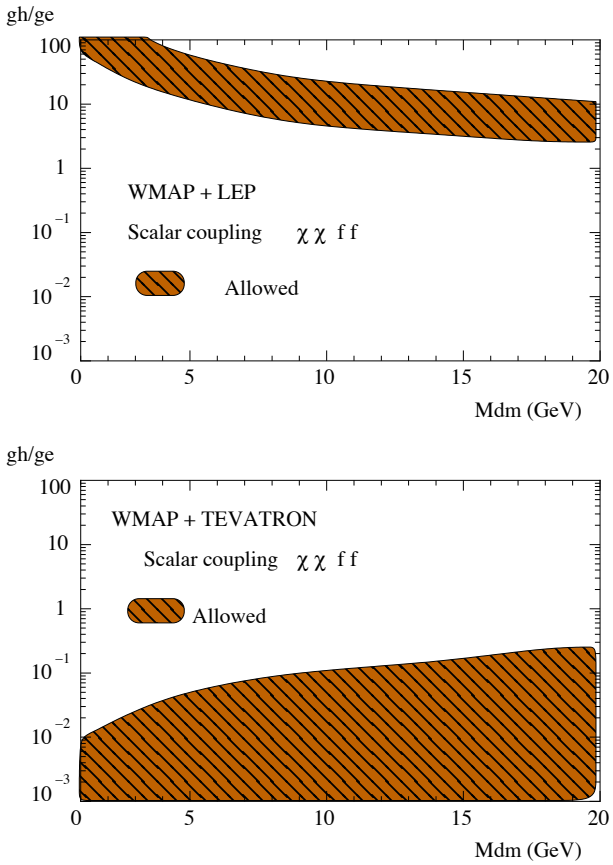

Figure 6. Hadronic ratio coupling for the annihilation of dark matter as function of the dark matter mass in the case of electronic couplings for a scalar-like interaction after a scan on Λ_e and Λ_h. After applying the constraint of mono-jet events from LEP (top) and Tevatron (bottom) we observe that no point of the parameter space respects both constraints (see the text for details).

into account the previous XENON100 analysis [25]). Whereas the scalar-like interaction is already excluded without the XENON100 data, dark matter with vector-like coupling to the SM still survives in a narrow hadrophilic region of the parameter space with light dark matter,[3] and another region definitively hadrophobic for $m_\chi \gtrsim 12\,\mathrm{GeV}$.

5 Conclusion and prospect

Recently, several astrophysical data or would-be signals has been observed in different dark-matter oriented experiments. In each case, one could fit the data at the price of specific nature of the coupling between the Standard Model (SM) particles and a light Dark Matter candidate: hadrophilic or leptophilic. We computed the rate of hadronic coupling needed to respect WMAP combined with the LEP and Tevatron constraints from mono-jet events. We showed that a light fermionic dark matter ($\lesssim 10\,\mathrm{GeV}$) is mainly excluded whatever is its type of interaction, whereas heavier candidates ($\gtrsim 20\,\mathrm{GeV}$) should be largely hadrophobic for vectorial interaction, but excluded for scalar one. We also studied the special case of scalar

[3] Which strangely coincides with the CoGENT excess signal [26]

JCAP10(2011)023

dark matter, using the single-photon events to constraint the coupling of dark matter to electron with a complete simulation of DELPHI events and showed that LEP and Tevatron are not able to restrict the couplings. One of the main consequences is that models with light electrophilic couplings, explaining INTEGRAL data or constraints from synchrotron radiations are excluded by Tevatron/LEP analysis. One possibility to escape such strong conclusion would be to suppose that DM has no electronic coupling. In this case, LEP limits do not apply. Moreover, if at the same time the hadronic coupling is only to the bottom or charm quark, Tevatron XENON100 bounds are not applicable too. However such unnatural construction should be excluded by FERMI last analysis of dwarf galaxies [28].

Acknowledgments

The authors want to thank particularly T. Schwetz, E. Dudas, A. Falkowski, G. Zaharijas and F. Bonnet for very useful discussions, adding special thanks for JB De Vivie and M. Kado for enlightening us with the LEP analysis. Acknowledgements also to the LPT "Magic Monday Journal Club" participants for enthusiastic and interesting debates. The work was supported by the french ANR TAPDMS *ANR-09-JCJC-0146* and the spanish MICINNs Consolider-Ingenio 2010 Programme under grant Multi- Dark *CSD2009-00064*. B. Zaldívar acknowledges as well the financial support of the FPI (MICINN) grant BES-2008-004688, under the contract *FPA-2007-60252*.

References

[1] CDF collaboration, T. Aaltonen et al., *Invariant mass distribution of jet pairs produced in association with a W boson in $p\bar{p}$ collisions at $\sqrt{s} = 1.96$ TeV*, *Phys. Rev. Lett.* **106** (2011) 171801 [arXiv:1104.0699] [SPIRES];
V. Cavaliere, *Measurement of $WW + WZ$ production cross section and study of the dijet mass spectrum in the $\ell\nu$ + jets final state at CDF*, Ph.D. thesis, Università degli studi di Siena, Siena, Italy (2010), FERMILAB-THESIS-2010-51.

[2] D. Hooper, J. Collar, J. Hall, D. McKinsey and C. Kelso, *A consistent dark matter interpretation for CoGeNT and DAMA/LIBRA*, *Phys. Rev.* **D 82** (2010) 123509 [arXiv:1007.1005] [SPIRES];
A. Fitzpatrick, D. Hooper and K.M. Zurek, *Implications of CoGeNT and DAMA for light WIMP dark matter*, *Phys. Rev.* **D 81** (2010) 115005 [arXiv:1003.0014] [SPIRES];
S. Andreas, C. Arina, T. Hambye, F.-S. Ling and M.H. Tytgat, *A light scalar WIMP through the Higgs portal and CoGeNT*, *Phys. Rev.* **D 82** (2010) 043522 [arXiv:1003.2595] [SPIRES];
Y. Mambrini, *The Kinetic dark-mixing in the light of CoGENT and XENON*100, *JCAP* **09** (2010) 022 [arXiv:1006.3318] [SPIRES];
J.M. Cline, A.R. Frey and F. Chen, *Metastable dark matter mechanisms for INTEGRAL* 511 *keV γ rays and DAMA/CoGeNT events*, *Phys. Rev.* **D 83** (2011) 083511 [arXiv:1008.1784] [SPIRES];
M.T. Frandsen, F. Kahlhoefer, J. March-Russell, C. McCabe, M. McCullough, et al., *On the DAMA and CoGeNT Modulations*, *Phys. Rev.* **D 84** (2011) 041301 [arXiv:1105.3734] [SPIRES];
D. Hooper and C. Kelso, *Implications of CoGeNT's new results for dark matter*, arXiv:1106.1066 [SPIRES].

[3] K. Cheung and J. Song, *Baryonic Z' explanation for the CDF W_{jj} excess*, *Phys. Rev. Lett.* **106** (2011) 211803 [arXiv:1104.1375] [SPIRES];
M. Buckley, P. Fileviez Perez, D. Hooper and E. Neil, *Dark forces at the Tevatron*, *Phys. Lett.* **B 702** (2011) 256 [arXiv:1104.3145] [SPIRES].

JCAP10(2011)023

[4] R. Bernabei, P. Belli, F. Montecchia, F. Nozzoli, F. Cappella, et al., *Investigating electron interacting dark matter*, *Phys. Rev.* **D 77** (2008) 023506 [arXiv:0712.0562] [SPIRES].

[5] P.J. Fox and E. Poppitz, *Leptophilic dark matter*, *Phys. Rev.* **D 79** (2009) 083528 [arXiv:0811.0399] [SPIRES].

[6] A. Dedes, I. Giomataris, K. Suxho and J. Vergados, *Searching for secluded dark matter via direct detection of recoiling nuclei as well as low energy electrons*, *Nucl. Phys.* **B 826** (2010) 148 [arXiv:0907.0758] [SPIRES].

[7] R. Bernabei, P. Belli, F. Cappella, R. Cerulli, F. Montecchia, et al., *Dark matter search*, *Riv. Nuovo Cim.* **26N1** (2003) 1 [astro-ph/0307403] [SPIRES];
DAMA collaboration, R. Bernabei et al., *First results from DAMA/LIBRA and the combined results with DAMA/NaI*, *Eur. Phys. J.* **C 56** (2008) 333 [arXiv:0804.2741] [SPIRES].

[8] CoGeNT collaboration, C. Aalseth et al., *Results from a search for light-mass dark matter with a P-type point contact germanium detector*, *Phys. Rev. Lett.* **106** (2011) 131301 [arXiv:1002.4703] [SPIRES].

[9] J. Kopp, V. Niro, T. Schwetz and J. Zupan, *DAMA/LIBRA and leptonically interacting dark matter*, *Phys. Rev.* **D 80** (2009) 083502 [arXiv:0907.3159] [SPIRES].

[10] J. Kopp, V. Niro, T. Schwetz and J. Zupan, *Leptophilic dark matter in direct detection experiments and in the Sun*, arXiv:1011.1398 [SPIRES].

[11] D. Hooper and L. Goodenough, *Dark matter annihilation in the galactic center as seen by the Fermi Gamma Ray Space Telescope*, *Phys. Lett.* **B 697** (2011) 412 [arXiv:1010.2752] [SPIRES].

[12] C. Boehm, D. Hooper, J. Silk, M. Casse and J. Paul, *MeV dark matter: Has it been detected?*, *Phys. Rev. Lett.* **92** (2004) 101301 [astro-ph/0309686] [SPIRES].

[13] M.Y. Khlopov, *Composite dark matter from stable charged constituents*, arXiv:0806.3581 [SPIRES]; *Dark Atoms of Dark Matter from New Stable Quarks and Leptons*, arXiv:1012.5756 [SPIRES].

[14] P.J. Fox, R. Harnik, J. Kopp and Y. Tsai, *LEP shines light on dark matter*, *Phys. Rev.* **D 84** (2011) 014028 [arXiv:1103.0240] [SPIRES].

[15] DELPHI collaboration, J. Abdallah et al., *Photon events with missing energy in e^+e^- collisions at $\sqrt{s} = 130$ GeV to 209 GeV*, *Eur. Phys. J.* **C 38** (2005) 395 [hep-ex/0406019] [SPIRES].

[16] D. Feldman, Z. Liu and P. Nath, *The Stückelberg Z' extension with kinetic mixing and milli-charged dark matter from the hidden sector*, *Phys. Rev.* **D 75** (2007) 115001 [hep-ph/0702123] [SPIRES];
P. Langacker, *The physics of heavy Z' gauge bosons*, *Rev. Mod. Phys.* **81** (2009) 1199 [arXiv:0801.1345] [SPIRES];
S. Cassel, D. Ghilencea and G. Ross, *Electroweak and dark matter constraints on a Z' in models with a hidden valley*, *Nucl. Phys.* **B 827** (2010) 256 [arXiv:0903.1118] [SPIRES];
E.J. Chun, J.-C. Park and S. Scopel, *Dark matter and a new gauge boson through kinetic mixing*, *JHEP* **02** (2011) 100 [arXiv:1011.3300] [SPIRES]; *The ZZ' kinetic mixing in the light of the recent direct and indirect dark matter searches*, *JCAP* **07** (2011) 009 [arXiv:1104.4799] [SPIRES];
Y. Mambrini, *Specific dark matter signatures from hidden* U(1), PoS(QFTHEP2010)027 [arXiv:1012.0447] [SPIRES];
Y. Mambrini, *A clear dark matter gamma ray line generated by the Green-Schwarz mechanism*, *JCAP* **12** (2009) 005 [arXiv:0907.2918] [SPIRES];
E. Dudas, Y. Mambrini, S. Pokorski and A. Romagnoni, *(In)visible Z' and dark matter*, *JHEP* **08** (2009) 014 [arXiv:0904.1745] [SPIRES];
P. Gondolo, P. Ko and Y. Omura, *Light dark matter in leptophobic Z' models*, arXiv:1106.0885 [SPIRES].

JCAP10(2011)023

[17] S. Andreas, C. Arina, T. Hambye, F.-S. Ling and M.H. Tytgat, *A light scalar WIMP through the Higgs portal and CoGeNT*, *Phys. Rev.* **D 82** (2010) 043522 [arXiv:1003.2595] [SPIRES];
T. Hambye, F.-S. Ling, L. Lopez Honorez and J. Rocher, *Scalar multiplet dark matter*, *JHEP* **07** (2009) 090 [*Erratum ibid.* **05** (2010) 066] [arXiv:0903.4010] [SPIRES];
C.E. Yaguna, *Gamma rays from the annihilation of singlet scalar dark matter*, *JCAP* **03** (2009) 003 [arXiv:0810.4267] [SPIRES];
L. Lopez Honorez and C.E. Yaguna, *The inert doublet model of dark matter revisited*, *JHEP* **09** (2010) 046 [arXiv:1003.3125] [SPIRES];
A. Goudelis, Y. Mambrini and C. Yaguna, *Antimatter signals of singlet scalar dark matter*, *JCAP* **12** (2009) 008 [arXiv:0909.2799] [SPIRES].

[18] M. Beltrán, D. Hooper, E.W. Kolb and Z.C. Krusberg, *Deducing the nature of dark matter from direct and indirect detection experiments in the absence of collider signatures of new physics*, *Phys. Rev.* **D 80** (2009) 043509 [arXiv:0808.3384] [SPIRES].

[19] WMAP collaboration, D. Spergel et al., *Wilkinson Microwave Anisotropy Probe (WMAP) three year results: implications for cosmology*, *Astrophys. J. Suppl.* **170** (2007) 377 [astro-ph/0603449] [SPIRES];
WMAP collaboration, E. Komatsu et al., *Five-year Wilkinson Microwave Anisotropy Probe (WMAP) observations: cosmological interpretation*, *Astrophys. J. Suppl.* **180** (2009) 330 [arXiv:0803.0547] [SPIRES].

[20] J. Alwall, P. Demin, S. de Visscher, R. Frederix, M. Herquet, et al., *MadGraph/MadEvent v4: The New Web Generation*, *JHEP* **09** (2007) 028 [arXiv:0706.2334] [SPIRES].

[21] G. Bélanger, F. Boudjema, A. Pukhov and A. Semenov, *MicrOMEGAs: a tool for dark matter studies*, arXiv:1005.4133 [SPIRES]; *Dark matter direct detection rate in a generic model with MicrOMEGAs* 2.2, *Comput. Phys. Commun.* **180** (2009) 747 [arXiv:0803.2360] [SPIRES]; *MicrOMEGAs* 2.0.7*: a program to calculate the relic density of dark matter in a generic model*, *Comput. Phys. Commun.* **177** (2007) 894 [SPIRES].

[22] Y. Bai, P.J. Fox and R. Harnik, *The Tevatron at the frontier of dark matter direct detection*, *JHEP* **12** (2010) 048 [arXiv:1005.3797] [SPIRES].

[23] J. Goodman, M. Ibe, A. Rajaraman, W. Shepherd, T.M. Tait, et al., *Constraints on Dark Matter from Colliders*, *Phys. Rev.* **D 82** (2010) 116010 [arXiv:1008.1783] [SPIRES].

[24] XENON100 collaboration, E. Aprile et al., *Implications on inelastic dark matter from* 100 *live days of XENON*100 *data*, *Phys. Rev.* **D 84** (2011) 061101 [arXiv:1104.3121] [SPIRES].

[25] XENON100 collaboration, E. Aprile et al., *Dark matter results from* 100 *live days of XENON*100 *data*, to be publlished in *Phys. Rev. Lett.*, arXiv:1104.2549 [SPIRES].

[26] M.R. Buckley, D. Hooper and T.M. Tait, *Particle physics implications for CoGeNT, DAMA and Fermi*, *Phys. Lett.* **B 702** (2011) 216 [arXiv:1011.1499] [SPIRES].

[27] G. Bertone, G. Sigl and J. Silk, *Astrophysical limits on massive dark matter*, *Mon. Not. Roy. Astron. Soc.* **326** (2001) 799 [astro-ph/0101134] [SPIRES];
K. Ishiwata, S. Matsumoto and T. Moroi, *Synchrotron radiation from the galactic center in decaying dark matter scenario*, *Phys. Rev.* **D 79** (2009) 043527 [arXiv:0811.4492] [SPIRES];
G. Bertone, M. Cirelli, A. Strumia and M. Taoso, *Gamma-ray and radio tests of the e^+e^- excess from DM annihilations*, *JCAP* **03** (2009) 009 [arXiv:0811.3744] [SPIRES];
C. Boehm, J. Silk and T. Ensslin, *Radio observations of the galactic centre and the Coma cluster as a probe of light dark matter self-annihilations and decay*, arXiv:1008.5175 [SPIRES];
T. Delahaye, C. Boehm and J. Silk, *Can Planck constrain indirect detection of dark matter in our galaxy?*, arXiv:1105.4689 [SPIRES].

[28] M.L. Garde, *Constraining dark matter signal from a combined analysis of Milky Way satellites using the Fermi-LAT*, arXiv:1102.5701 [SPIRES].

CHAPTER 6

COMPLEMENTARITY AMONG DIFFERENT STRATEGIES OF DARK MATTER SEARCHES

Journal of Cosmology and Astroparticle Physics
An IOP and SISSA journal

Complementarity of Galactic radio and collider data in constraining WIMP dark matter models

Yann Mambrini,[a] **Michel H.G. Tytgat,**[b] **Gabrijela Zaharijas**[c,d] **and Bryan Zaldívar**[e]

[a]Laboratoire de Physique Théorique, Université Paris-Sud, F-91405 Orsay, France
[b]Service de Physique Théorique, Université Libre de Bruxelles, CP225, Bld du Triomphe, 1050 Brussels, Belgium
[c]The Abdus Salam International Centre for Theoretical Physics, Strada Costiera 11, I-34014 Trieste, Italy
[d]Institut de Physique Théorique, CEA/Saclay, F-91191 Gif sur Yvette, France
[e]Instituto de Fisica Teorica, IFT-UAM/CSIC, Nicolas Cabrera 15, UAM, Cantoblanco, 28049 Madrid, Spain

E-mail: yann.mambrini@th.u-psud.fr, mtytgat@ulb.ac.be, gzaharij@ictp.it, bryan.zaldivar@uam.es

Received June 26, 2012
Revised October 6, 2012
Accepted October 10, 2012
Published November 20, 2012

Abstract. In this work we confront dark matter models to constraints that may be derived from radio synchrotron radiation from the Galaxy, taking into account the astrophysical uncertainties and we compare these to bounds set by accelerator and complementary indirect dark matter searches. Specifically we apply our analysis to three popular particle physics models. First, a generic effective operator approach, in which case we set bounds on the corresponding mass scale, and then, two specific UV completions, the Z' and Higgs portals. We show that for many candidates, the radio synchrotron limits are competitive with the other searches, and could even give the strongest constraints (as of today) with some reasonable assumptions regarding the astrophysical uncertainties.

Keywords: dark matter theory, dark matter experiments, absorption and radiation processes

ArXiv ePrint: 1206.2352

doi:10.1088/1475-7516/2012/11/038

JCAP11(2012)038

Contents

JCAP11(2012)038

1 Introduction

Dark Matter (DM) is one of the most important issues in particle physics and cosmology and understanding its nature will likely play an essential rôle in our comprehension of both fundamental interactions and the structure of the Universe. Over the years, a Weakly Interacting Massive Particle (WIMP) has emerged as one of the favourite candidates, in part due to the natural explanation of its cosmological abundance through thermal freeze-out (see e.g. [1–3]). While, as of today, we have no other evidence for DM than through its gravitational manifestations, the alleged weak interaction of WIMPs have open the possibility to actually observe DM experimentally. Several strategies have been proposed, and are actively pursued, to search for WIMPs. Direct detection experiments, such as CDMS [4] and XENON100 [5], are dedicated to the search of DM in the Earth. These are supplemented by multi-purpose

particle physics experiments at colliders, most notably the LHC, where DM is expected to be produced, and to manifest itself as missing energy, in collisions. In particular, analysis of single-photon or mono-jet events with missing energy have recently proved to give very pertinent constraints on WIMP mass and interactions [6–10]. A radically different, and a complementary approach is to search for indirect detection of WIMPs, through the remnants of their annihilation (or decays) in astrophysical environments, like the Galactic Centre (GC) of the Milky Way, nearby dwarf spheroidal galaxies (dSphs) or in general any dense region of the Universe. The possible remnants, or messengers, are high energy neutrinos, anti-matter in cosmic rays (CR), and gamma-rays, or more generally an injection of energy of charged particles in the early universe.

In [11] some of us analysed bounds on effective couplings between dark matter and SM particles from single-photon and mono-jet signals, at LEP and the LHC respectively. Such studies are usually compared to exclusion limits set by direct detection experiments (see also e.g. [7, 9, 10]). In general terms, the colliders data are comparatively more constraining for low mass dark matter candidates, in particular below the threshold of direct detection experiments, while the latter are more constraining at higher masses, where dark matter production at colliders is impeded. Interestingly, indirect searches tend also to be most constraining for low mass dark matter candidates. This is essentially because the flux of particles produced by dark matter annihilation (gamma-rays, etc.) is proportional to the inverse DM mass to the square. In particular, interesting constraints have been set on the annihilation cross section of DM based on the measured synchrotron radiation from the inner regions of the Milky Way. While synchrotron radiation constraints on DM have already been much studied in the literature (e.g. in [14–18]), to our knowledge no analysis of specific particle physics models implications have been made so far. Concretely in the present work we confront the constraints from synchrotron radiation in the Galaxy at radio frequencies to those set by colliders data. In particular we study to which extend they are complementary. Our analysis is based both on an effective operator approach (so we put limits on energy scales) and on two specific DM models, the so-called Z' and Higgs portals. We also show how colliders and radio synchrotron radiation limits compare to bounds set by *Fermi* LAT based on dSphs [19], and to constraints imposed on DM annihilations from the effect on the CMB anisotropies [20].

The constraints from colliders and those from indirect searches do not quite stand on the same footing. In particular, although the radio data are potentially strongly constraining for rather light DM candidates — as we show also in this work — the modelling of DM induced radio fluxes suffers from several sources of astrophysical uncertainties. We explore those by using both a semi-analytic approach, which allows to control, for instance, the dependence of the radio flux on the magnitude of the magnetic fields in our region of interest, and a full numerical calculation as implemented in the `GALPROP`[1] code [21, 22] which allows to explore the full set of CR propagation parameters and up-to-date energy losses, thus cross checking the semi-analytic method and calibrating its parameters. To gauge the impact of CR propagation parameters on synchrotron signals, we sample a range of CR propagation parameters sets using both those derived to probe uncertainty in the local CR fluxes, and used traditionally to bracket this type of uncertainty (MIN, MED, MAX set of parameters [23]), and CR propagation sets which were recently shown to give a good description of the gamma-ray [24, 25] and radio [26] data and which are therefore suited to test electron propagation parameters in the inner regions of our galaxy.

[1] http://galprop.stanford.edu/webrun.php.

JCAP11(2012)038

We present our results as a function of the systematic uncertainties on the modelling of the backgrounds due to standard astrophysics, illustrating potential future improvements of the limits based on radio data.

The paper is organised as follows. In section 2 we review the formalism of the semi-analytical approach used in this work, and also present the setup for the full numerical study. In section 3 we discuss at lengths the astrophysical framework. In part 3.1 we discuss the astrophysical uncertainties, while in part 3.2 we discuss our cross-check between semi-analytical and numerical approaches. In part 3.3 we show the dependence of the synchrotron flux with different choices of Dark Matter profile, and Part 3.4 is devoted to study, numerically, the impact of different choices of CR diffusion and propagation parameters to the synchrotron signal. Part 3.5 is a semi-analytical (cross-checked by numerical) study of the dependence of the synchrotron flux on the magnetic field normalisation. Then, section 5 is devoted to the discussion of synchrotron constraints on particle physics models. In part 5.1 we adopt a generic, also known as model-independent, approach based on effective operators. There we confront the synchrotron constraints we derive with other indirect searches and colliders constraints. In parts 5.2 and 5.3 we consider two specific UV completions, the Higgs and Z′ portal, to which we apply the synchrotron constraints. While the conclusions bear some resemblance, the constraints are quite distinct for the two models. Finally we give our conclusion and prospects in 6.

2 Synchrotron radio emission in the Milky Way

In the very high frequency radio (VHF) to microwave frequency range (i.e. 10 MHz − 300 GHz), various astrophysical processes contribute to the observed diffuse emission. The radio sky at frequencies below ~ 20 GHz is dominated by synchrotron emission of CR electrons (accelerated in e.g. supernovae shocks) on Galactic magnetic fields. However thermal bremsstrahlung (free-free emission) of electrons on the galactic ionised gas also contributes in this range. At higher frequencies the Cosmic Microwave Background (CMB) and its anisotropies represent the main signal. Emission by small grains of vibrating or spinning dust becomes relevant at even higher frequencies, starting approximately at $\gtrsim 60$ GHz.

Synchrotron signal of electron by-products of dark matter WIMP self-annihilation is generally expected to fall in the 100 MHz −100 GHz range (see for example [16]). However, it has been noted in [17, 18] that for light dark matter candidates it is beneficial to consider lower frequencies. For instance, for a magnetic field of μG strength, as typical for the Galaxy, electrons with energies $\lesssim 10$ GeV generate synchrotron emission which peaks at tens of MHz (see figure 4 in [18] or eq. (2.16) below), and following [18] we focus on a 45 MHz survey [27].[2]

Additional motivation to consider the 45 MHz survey is that it covers a large region of the sky (for a visual representation of the coverage of this and other radio surveys, see [28]). In the past, observations of the Galactic Centre compact radio source (SgrA*) with high angular resolution surveys have been used to constrain a possible DM signal (but at higher frequencies, for example a 408 MHz survey [29] was used in [12–15, 38] and a 330 MHz observation of the SgrA* [30] in [17]). Indeed the synchrotron flux is expected to be strongly enhanced close to the Galactic centre, as cusps in a DM density are generically found in DM simulations

[2] To constrain heavier DM candidates it is beneficial to consider higher frequency surveys. For example in figure 6 of [18], authors show that the DM limits, for the $\mu^+\mu^-$ channel improve by a factor of $\lesssim 2$ at DM mass of $\lesssim$ TeV when considering 408 MHz, with respect to the limits derived using the 45 MHz data.

JCAP11(2012)038

in central regions of DM halos, and therefore strong constraints on DM annihilation cross section may be placed by considering radio emission from SgrA*. However, the mass in the inner regions of the Galaxy is baryon dominated and it is possible that baryonic feedback processes might erase the putative dark matter cusp [1–3]. On top of that, the very presence of a black hole might disrupt the DM profile, both by making it steeper, through adiabatic contraction [31] or cored through scattering of dark matter particles by stars in the dense stellar cusp observed in the vicinity of the SgrA* [32]. Having these uncertainties in mind, we take advantage of the fact that 45 MHz [27] is a large scale survey and we test its data for a DM contribution farther away from the Galactic Centre, where the DM density is more robustly determined.

In order to compute the synchrotron signal, the propagation and energy losses of a Galactic electron population need to be modelled.

The propagation of electrons[3] in the galactic medium is governed by a transport equation, which can be written as [33]

$$\begin{aligned}\frac{\partial n(x,E)}{\partial t} &= q(x,E) + \nabla\cdot\left[K_{xx}\,\nabla n(x,E) - V_c\,n(x,E)\right] \\ &+\frac{\partial}{\partial p}\,p^2\,K_{pp}\,\frac{\partial}{\partial p}\,\frac{1}{p^2}\,n(x,E) \\ &-\frac{\partial}{\partial p}\left(\dot{p}\,n(x,E) - \frac{p}{3}\,(\nabla\,V_c)\right),\end{aligned} \tag{2.1}$$

where $n(x,E)$ is the number density of electron per unit energy, and $q(x,E)$ is the electron source term. The transport through magnetic turbulence can be described by the diffusion coefficient K_{xx}. In the following we will assume, as customary in literature, that the diffusion coefficient is spatially independent and has an energy dependence of the form $K_{xx} = K_0 E^\delta$. V_c is the convection velocity and re-acceleration is described as diffusion in momentum space and is determined by the coefficient K_{pp}, which is usually expressed using Alfven speed v_a, defined as

$$K_{pp}\,K_{xx} = \frac{4\,p^2\,v_a^2}{3\,\delta\,(4-\delta^2)\,(4-\delta)} \tag{2.2}$$

Cosmic rays propagate in the diffusive halo which is usually approximated to have a cylindrical shape with radius R_h around 20 kpc and half-thickness L_h which could lie in the range of 1 to 15 kpc. The spatial boundary conditions assume free particle escape, i.e. $n(R_h,z,p) = n(r,\pm L_h,p) = 0$.

We dedicate the next two sections to describe a semi-analytical and, briefly, fully numerical approach used to derive synchrotron flux. While semi-analytical approach allows in some cases for more physical insight (for instance, we use it to find the analytical dependence of synchrotron flux on the strength of the magnetic field, see 3.5), we have checked the robustness of that approach against a full numerical computation, as implemented in the `GALPROP` code [21, 22].

[3]DM annihilation produce the same amount of electrons and positrons, so we refer collectively to these particles as 'electrons'.

JCAP11(2012)038

2.1 Semi-analytical approach

For the semi-analytical calculations of the synchrotron signal, following [34, 35] we neglect re-acceleration and convection terms, which we have checked it is a safe assumption for our particular study,[4] and rewrite eq. (2.1) as

$$\frac{\partial n(x,E)}{\partial t} - \nabla \cdot [K(x,E)\ \nabla n(x,E)] - \frac{\partial}{\partial E}[b(x,E)n(x,E)] = q(x,E)\,, \tag{2.3}$$

where $b(x,E)$ encodes the energy loss rate. Cosmic ray electrons loose energy mainly through synchrotron radiation and Inverse Compton scattering (IC), with a rate $b(x,E)$ which at the galactic medium is typically of the order $10^{-16}\,\mathrm{GeV{\cdot}s^{-1}}$. Additional bremsstrahlung losses of electron energies on the interstellar medium are neglected in this semi-analytical approach, although they may have a very small effect (see for example figure 1), since for the synchrotron frequency we work with, the electron energies of interest are around 1 GeV.

Assuming a steady state, eq. (2.3) can be re-expressed as

$$\frac{\partial \tilde{n}(x,E)}{\partial \tilde{t}} - K_0\ \Delta \tilde{n}(x,E) = \tilde{q}(x,E) \tag{2.4}$$

in which the derivative with respect to energy has been parametrized in terms of the parameter $\tilde{t} \equiv -\int dE(E^\delta/b(x,E))$. If at the level of propagation one considers that energy losses have an average value over all the diffusion region, i.e. $b(x,E) \approx b(E) = E^2/\tau\,\mathrm{GeV{\cdot}s^{-1}}$ (see eq. (2.19)), then in (2.4) $\tilde{n}(x,E) = E^2 n(x,E)$ and $\tilde{q}(x,E) = E^{2-\delta} q(x,E)$. The solution of this equation can be found in the Green function formalism to be

$$n(x,E) = \frac{1}{b(E)} \int_E^\infty dE_s \times \int_{\mathrm{DZ}} d^3x G(x, E \leftarrow x_s, E_s) q(x_s, E_s) \tag{2.5}$$

where the volume integral is over the diffusion zone (DZ). The Green function $G(x, E \leftarrow x_s, E_s)$ gives the probability for an electron injected at x_s with energy E_s to reach x with energy $E < E_s$, and has a general solution of the form

$$G(x, E \leftarrow x_s, E_s) = \frac{\tau}{E^2} G(x, \tilde{t} \leftarrow x_s, \tilde{t}_s) \tag{2.6}$$

$$G(x, \tilde{t} \leftarrow x_s, \tilde{t}_s) = \left(\frac{1}{4\pi K_0 \Delta\tilde{t}}\right)^{3/2} e^{-\frac{(\Delta x)^2}{4K_0\Delta\tilde{t}}}\,, \tag{2.7}$$

where $\Delta\tilde{t} = \tilde{t} - \tilde{t}_s$ and $(\Delta x)^2 = (\mathbf{x} - \mathbf{x}_s)^2$. The unique argument of the Green function is actually the diffusion length $\lambda = 4K_0\Delta\tilde{t}$, because the energy dependence enters only in this combination. This is the characteristic length of an electron traveling during its propagation. Here we are going to focus on diffusion models for which the half-thickness $L_h \sim 4$ kpc is small compared to the radius of the disk R_h, such that in practice the radial boundary has negligible effect on propagation [35]. The Green function for which $n(x,E)$ vanishes at $z = \pm L_h$ may be expressed as [34]

$$\tilde{G}(\lambda, L) = \frac{1}{(\sqrt{\pi}\lambda)^3} \sum_{n=-\infty}^{n=\infty} (-1)^n\ \exp^{-(2nL + (-1)^n z_s)^2/\lambda^2}\,. \tag{2.8}$$

[4] However, these two parameters are by default included in the numerical calculation, see the next section.

JCAP11(2012)038

As for the source term, in the case of production from DM annihilation with cross-section $\langle\sigma v\rangle$, it can be expressed as

$$q(x,E) = \eta\ \langle\sigma v\rangle \left\{\frac{\rho(x)}{m_{DM}}\right\}^2 \frac{dN}{dE}\ . \tag{2.9}$$

Here $\rho(x)$ is the DM profile, given in units of GeV/cm^3, and $\eta = 1/4$ or $\eta = 1/2$ depending on the Dirac or Majorana nature of DM. The injection spectrum of electrons is given by dN/dE.

With all these ingredients we can express the electron number density as

$$n(x,E) = \eta\ \langle\sigma v\rangle \left(\frac{\rho_\odot}{m_{DM}}\right)^2 \frac{1}{b(E)} \int_E^{m_{DM}} dE_s \frac{dN}{dE_s} I_{\rm halo}\ . \tag{2.10}$$

Here $I(\lambda)$ is the so-called halo function, which is defined has

$$I_{\rm halo} = \int_{\rm DZ} d^3x_s \tilde{G}(x, E \leftarrow x_s, E_s) \left\{\frac{\rho(x_s)}{\rho_\odot}\right\}^2 . \tag{2.11}$$

When electrons (and positrons) are created in the Galaxy, they are accelerated by the local magnetic field and produce synchrotron radiation with an energy flux per unit frequency ν per solid angle (or spectral energy distribution) given by

$$F_\nu = \frac{1}{4\pi} \int_{\rm los} dl \int_{m_e}^{m_{DM}} dE\ P(x,\nu,E)\ n(x,E) \tag{2.12}$$

where the integrations are performed along the line of sight (los) and on the electron energies. In this relation $P(x,\nu,E)$ is the synchrotron power (per unit frequency) emitted at ν by an electron of energy E which, for an energy distribution of electrons $n(x,E)$, must be integrated over all the electron energies E which lead to synchrotron radiation at the same frequency ν. In practice it can be shown (see e.g. [36]) that the radiation power as a function of ν is strongly peaked near a so-called critical frequency ν_c, defined as

$$\nu_c = \frac{3eBE^2}{4\pi m_e^3} \equiv 16{\rm MHz} \left(\frac{E}{\rm GeV}\right)^2 \left(\frac{B}{\mu G}\right) \tag{2.13}$$

in natural units, so that there is a near one-to-one correspondence between ν and E which, following [37], we take to be such that

$$P(\nu,E) \approx \frac{4}{27} \frac{e^3 B}{m_e} \delta\left(\frac{\nu}{\nu_c(E)} - 0.29\right). \tag{2.14}$$

Using this handy approximation which, in one form or another, is often adopted in the literature (see also [17, 38]), the flux of eq. (2.12) takes a simple form,

$$F_\nu = \frac{1}{4\pi} \int_{\rm los} dl\, \frac{E}{2\nu}\, P_{\rm sync}(E)\, n(x,E) \tag{2.15}$$

where

$$E \equiv E(\nu) \approx \left(\frac{\nu}{4.7{\rm MHz}}\right)^{1/2} \left(\frac{\mu G}{B}\right)^{1/2} {\rm GeV} \tag{2.16}$$

JCAP11(2012)038

which stems from $\nu = 0.29\,\nu_c(E)$, and where $P_{\rm sync}$ is the total synchrotron energy loss rate of an electron of energy E,[5]

$$P_{sync}(E) \hat{=} \int d\nu P(\nu, E) = \frac{e^4 B^2 E^2}{9\pi m_e^4}$$
$$\simeq 2.5 \cdot 10^{-18} \left(\frac{E}{\rm GeV}\right)^2 \left(\frac{B}{\mu\rm G}\right)^2 \ {\rm GeV \cdot s^{-1}} \tag{2.17}$$

Finally, we may express the synchrotron energy flux as

$$F_\nu = 1.21 \times 10^8 \frac{\rm Jy}{\rm sr} \left\{ \frac{\eta}{2} \left(\frac{\langle\sigma v\rangle}{3.1 \times 10^{-26} {\rm cm}^3/s}\right) \right. \tag{2.18}$$
$$\times \left(\frac{1{\rm GeV}}{m_{DM}}\right)^2 \left(\frac{\rho_\odot}{\rm GeV/cm^3}\right)^2 \left(\frac{\mu\rm G}{B}\right)^{1/2}$$
$$\left. \times \left(\frac{\rm GHz}{\nu}\right)^{1/2} \frac{P_{\rm sync}(E)}{b(E)} \frac{1}{4\pi} \int \frac{dl}{\rm kpc} \int_E^{m_{DM}} dE_s \frac{dN}{dE_s} I_{\rm halo} \right. .$$

using jansky flux units (Jy), 1 Jy $= 10^{-26}$ W·m^{-2}·Hz^{-1}.[6] The total energy loss assumed here is given by

$$b(E) = P_{\rm sync}(E)(1 + r_{\rm IC/sync}) \tag{2.19}$$

where

$$r_{\rm IC/sync} = \frac{2}{3} \frac{U_{\rm rad}}{B^2/2} \simeq 2 \left(\frac{U_{\rm rad}}{8\ {\rm eV/cm^3}}\right) \left(\frac{B}{10\ \mu\rm G}\right)^{-2} \tag{2.20}$$

is the ratio between IC and synchrotron energy loss and $U_{\rm rad}$ is the total radiation density.

2.2 Numerical approach

In parallel to the semi-analytic expressions, we have determined the synchrotron flux using a fully numerical approach as implemented in the GALPROP v54 code [21, 22]. We ran GALPROP in 2D in galacto-centric cylindrical coordinates (R, z), solving the CR transport equation on a grid and assuming cylindrical boundary conditions. Both re-acceleration and convection are included in GALPROP, though we set V_c to zero in our calculations for simplicity. The energy losses include also bremsstrahlung losses, based on up-to-date whole sky maps of the interstellar gas (for details on generation of gas maps see [24]). For IC losses GALPROP uses 2D+1 maps[7] of the interstellar radiation field, computed based on a model of the radiation emission of stellar populations and further reprocessing in the Galactic dust [21].

The spectrum and distribution of the synchrotron emissivity as seen by an observer at the solar position depends on the form of the magnetic field, and the spectrum and distribution of CR leptons and is computed as a function of $(R, z,\ \nu)$. The emissivity is then integrated over the line-of-sight to get the synchrotron intensity. We chose the form of the magnetic field consistently with the semi-analytic approach, as detailed below.

[5] In these expressions, we are a bit loose regarding the definition of the magnetic field. In principle B should be the effective magnetic field felt by the electron, $B_\perp$. In practice, assuming an isotropic distribution of electron velocities, $\langle B_\perp^2 \rangle = 2/3 B^2$. This is explicit in eq. (2.17) (see for instance eq. (6.7) in ref.([36])). For convenience, this factor of 2/3 has been included in the definition of eq. (2.14), as in [37].

[6] In the following, we will express the flux F_ν in terms of the brightness temperature of the radiation, T, $F_\nu = 2\nu^2 T / \exp(2\pi\nu/T) - 1$, using the blackbody relation.

[7] Two spatial and the frequency dimension.

JCAP11(2012)038

3 General astrophysical setup

3.1 Astrophysical uncertainties

Studies coming from N-body simulations have led to popular expressions for the distribution of DM in the Galactic halo, like the Navarro-Frenk-White (NFW) density profile [39]

$$\rho_{\rm NFW}(r) = \frac{\rho_s}{\frac{r}{r_s}\left(1+\frac{r}{r_s}\right)^2}\,, \tag{3.1}$$

or the Einasto profile [40, 41]

$$\rho_{\rm EIN}(r) = \rho_s \exp\left\{-\frac{2}{\alpha}\left(\left(\frac{r}{r_s}\right)^{\alpha}-1\right)\right\}\,, \tag{3.2}$$

where r the radial distance from the centre of the DM halo. On the other hand, observations of galactic rotation curves as well some of the simulations which include also baryonic feedback on DM density (for a recent example see [42]) find DM density profiles which are more cored towards the inner regions of the Galaxy. One example of such profile is the isothermal profile [43, 44]

$$\rho_{\rm iso}(r) = \rho_s\,\frac{r_s^2}{r^2+r_s^2} \tag{3.3}$$

or modified Einasto profile (in this case the parameter α is smaller when compared to the parameters found in simulations which contain only DM component, [45]). While the parameter α for the Einasto profile is fixed from a fit to the simulations, the values of parameters ρ_s, a typical scale density, and r_s, a typical scale radius for the Milky Way are determined from astrophysical observations (e.g. local stellar surface brightness, stellar rotational curves, total Milky Way mass within a given distance..., see e.g. [2, 45]). The ratio of the synchrotron signal calculated with DM density of these three profiles gets smaller at higher latitudes, as at those distances (closer to the Solar position) DM density is better constrained, see section 3.3. As the rotational curve measurements are poor at distances smaller than 2 kpc (or $\sim 10^\circ$) from the Galacic Center and those regions of the Galaxy are baryon dominated, we choose the Region Of Interest (ROI) which spans $|b| \in (10 \pm 3)^\circ$ in Galactic latitudes, and $|l| \lesssim 3^\circ$ in Galactic longitudes.

Together with DM density profile, the CR propagation parameters pose one of the main uncertainties in prediction of the synchrotron signal. In [18], the three models called MIN/MED/MAX [23] and featured in table 1 are used to probe the uncertainty in CR propagation parameters. Originally, those parameters were derived to produce the maximal, median and minimal anti-proton flux from dark matter, while being compatible with the CR secondary to primary B/C ratio measurement [46, 47]. Therefore, by construction, they do not necessarily capture the uncertainty in the electron fluxes in the inner Galaxy, which is of interest here. In section 3.4 we will comment in more detail on the impact of a choice of a CR parameters, exploring additional sets consistent with the CR data and which were i) derived numerically and ii) shown to reproduce the observed whole sky gamma-ray or radio emission, therefore probing more directly the signals in the inner Galaxy, [24–26].

The Galactic magnetic field (GMF) is considered possibly the most important ingredient when dealing with synchrotron radiation. In the diffuse interstellar medium it has a large-scale regular component as well as a small-scale random part, both having a strength of

JCAP11(2012)038

Model	L_h [kpc]	K_0 [cm^2 s^{-1}]	δ	v_a [km s^{-1}]
MIN	1	$4.8\,10^{26}$	0.85	0
MED	4	$3.4\,10^{27}$	0.70	0
MAX	15	$2.3\,10^{28}$	0.46	0
1a	4	$6.6\,10^{28}$	0.26	34.2
1b	4	$6.6\,10^{28}$	0.35	42.7
2a	10	$1.2\,10^{29}$	0.3	39.2
2b	10	$1.05\,10^{29}$	0.3	39.2
PD	4	$3.4\,10^{28}$	0.5	0

Table 1. Upper three raws: parameter sets derived using a semi-analytical approach, to lead to MIN/MED/MAX anti-proton fluxes at Earth from an exotic Galactic component [23]. Lower four rows: parameters from [25], consistent with [24], derived using `GALPROP` code in a fit to CR data, and shown to reproduce the gamma-ray diffuse data well. Last row: plain diffusion model, shown to be consistent with the radio data at 22 MHz — 94 GHz frequencies, [26].

order micro-Gauss. The best available constraints in determining the *large-scale* GMF are Faraday rotation measures and polarized synchrotron radiation, see e.g. [48–51], while *random* component is deduced mainly based on the synchrotron emission.

Several 3D models of the large scale magnetic field are implemented in `GALPROP` (e.g., [52, 53]). However, as our ROI is away from the Galactic disk and the small-scale random component is expected to dominate the total value of the magnetic field, we use a simple parametrisation for a *total* magnetic field as customary in literature:

$$B(\rho, z) \propto \exp\left(-\frac{r - r_\odot}{R_m} - \frac{|z|}{L_m}\right) . \tag{3.4}$$

The parameters R_m and L_m should in principle depend on the diffusion model assumed (or *vice versa*), since the propagation in the Galactic medium is intimately related with the magnetic field. We follow [18] in taking $L_m = \delta \cdot L_h$ and $R_m = \delta \cdot R_h$. It was shown in that work that an actual extent of L_m and R_m does not play a critical role (the difference between a constant magnetic field and the exponential form defined above is $\lesssim 30\%$), as long as the field extends into our ROI (i.e. $L_m \gtrsim 1$ kpc). The normalisation at Sun's position $B_\odot$ is more or less well constrained, and we take the value of 6 μG [54], consistent with the measurements [48–51]. However the value of the field in the inner Galaxy is considerably less known and we rewrite the normalisation of (3.4) as[8]

$$B_0 \equiv B_\odot[1 + K\ \Theta(R_{IG} - r)] \tag{3.5}$$

where $\Theta(R_{IG} - r)$ is the unit step function as a function of $r = \sqrt{\rho^2 + z^2}$. With this change, while leaving $B_\odot$ unchanged *locally* we allow for the magnetic field to have a higher effective normalization $B_\odot\ (1 + K)$ in the inner Galaxy. We arbitrary set $R_{IG} = 2$ kpc, in order to cover our ROI. We therefore fix the spatial dependence of the B field and explore the impact of overall normalisation $B_\odot\ (1+K)$ in the inner Galaxy, on synchrotron fluxes in section 3.5.

Contributions to the energy losses for electrons are assumed to come only from synchrotron and IC processes in our semi-analytical approach, as commented above. In principle, the radiation density $U_{\rm rad}$ (see eq. (2.20)) has a spatial profile, which affects the synchrotron

[8] following [55].

JCAP11(2012)038

flux estimations. However, in the semi-analytical estimations used here we take $U_{\rm rad}$ to be constant, which turns out to be a good approximation for the particular study performed in this work, as is justified in the next section. For the value of $U_{\rm rad}$ we take $8\,{\rm eV\ cm^{-3}}$, which is approximately the value read off the ISRF maps used by GALPROP in our ROI.[9]

Concerning the frequency of observation we focus on the data taken at 45 MHz. In [18] it was shown that in a wide range of frequencies (22 to 1420 MHz) the change in the measured synchrotron flux is very small, while going to lower frequencies maximises a synchrotron signal of low mass WIMPs. The RMS temperature noise of this survey is 3500 K, which is generally subdominant with respect to the systematics errors involved in theoretical modelling.

3.2 Cross-check of semi-analytical calculation of synchrotron fluxes

In figure 1 we show a comparison of synchrotron spectra obtained with the semi-analytical (SA) and numerical/GALPROP (NG) approaches. We see that in our region of interest at the intermediate latitudes (of ~ 10 degrees) the agreement between the two predictions is generally good (within a factor of 1.5). This is not surprising, as the 45-MHz emission comes from low-energy electrons which diffuse over large distances, the difference between taking average properties (as in the SA method) and proper spatial profiles (as in the numerical approach) is not expected to be large. In addition, we observe that in the region of low latitudes, SA calculation gives larger fluxes than the NG counterpart, while for the region of large latitudes, it is the opposite. That too is expected, as in the SA approach we have used a constant radiation density $U_{\rm rad}$, which corresponds to its value at intermediate latitudes in the maps used in the NG approach. Typically this radiation density gets smaller as the distance from the galactic centre increases, so the synchrotron flux becomes less suppressed, explaining why the GALPROP estimations are typically larger for large angles and vice versa, see figure 1.

However, as commented in section D, the data of synchrotron flux we used to constrain dark matter models is the one taken at a latitude of $\sim 10^\circ$, and for this latitude, the semi-analytical and numerical approaches are in very good agreement. In other words, for this latitude the approximation of taking $U_{\rm rad}$ constant works very well.

Finally, we have checked a good agreement with the results of [18] using their particular setup. The biggest difference between our works is that we assume a factor of ~ 2 higher ISRF energy densities, inspired by the values implemented in the GALPROP code in our ROI. That in turn implies higher overall energy losses, and therefore lower synchrotron fluxes (by about the same factor, if IC losses are the dominant ones, see eq. (3.6)), for the otherwise same parameter set.

[9] Note however that the conditions in the inner Galaxy might be quite different from a simple CR propagation setup assumed here. In particular, observations of the bubbles like structures Centerd at the Galactic centre and extending to 50 deg in latitudes in gamma rays [56, 57] and WMAP haze at microwave frequencies, observed by WMAP [58] and Planck [59], witness of possibly more complicated configuration of the magnetic fields and CR propagation parameters in that region. While bubble-like structures appear sub-dominant with respect to the standard components of the diffuse emission in our ROI and electron energies of interest, we caution that before their origin is understood, the actual structure of magnetic fields or the CR propagation conditions, cannot be reliably modeled.

JCAP11(2012)038

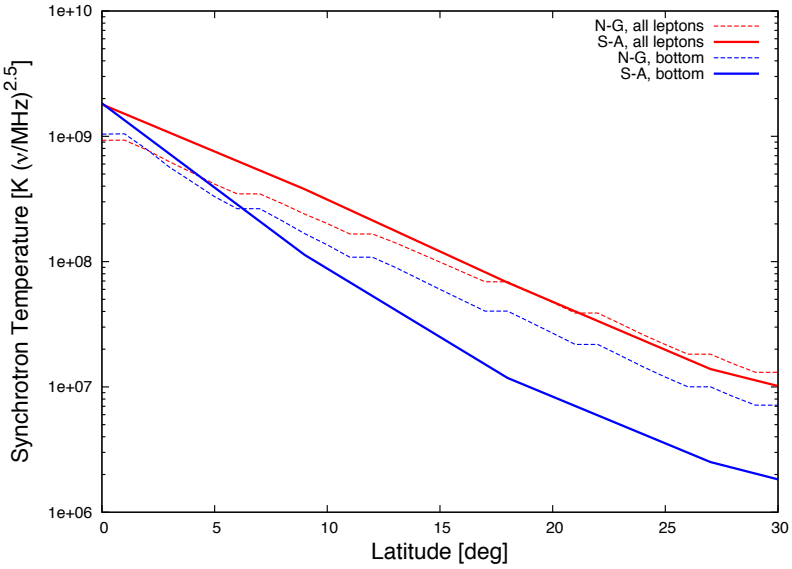

Figure 1. Comparison between semi-analytical (S-A.) and numerical/Galprop (N-G) approaches, for different annihilation channels, and DM mass of $m_{DM} = 10\,\mathrm{GeV}$. A frequency of 45 MHz was used, assuming a magnetic field normalised to $B_{\mathrm{GC}} = 10\ \mu\mathrm{G}$ (which corresponds to K=0, i.e. no enhancement of the magnetic field in our ROI).

3.3 Synchrotron signal for different choices of DM density profile

In the remainder of the text we will focus on two DM profiles, NFW, eq. (3.1) and isothermal (ISO) eq. (3.3), using the following values of parameters, consistent with observations: $\rho_s = 0.31\,\mathrm{GeV\,cm^{-3}}$, $r_s = 21$ kpc, for an NFW profile, and $\rho_s = 1.53\,\mathrm{GeV\,cm^{-3}}$ and $r_s = 5$ kpc for Isothermal profile,[10] [18]. However, in this section we also show the prediction for the synchrotron signal in the case of a modified Einasto profile. In particular, this profile is modified to have a shallower inner slope than the usual Einasto profile found in DM-only simulations and it describes better results of simulations which include baryonic feedback (parameters we use are $\alpha = 0.11$, $r_s = 35.24$ kpc, $\rho_s = 0.041\,\mathrm{GeV\ cm^{-3}}$ [45]). As this profile is 'bulkier' at distances 1 kpc from the GC, the DM signals are generally higher than those of NFW in that region.

In the parameter sets we chose, the local value of DM density is set to $\rho_\odot = 0.43\,\mathrm{GeV\,cm^{-3}}$. One should also keep in mind that the overall normalisation of DM distribution $\rho_\odot$ is uncertain, being in the $(0.43 \pm 0.113 \pm 0.096)\ \mathrm{GeV\,cm^{-3}}$ range[11] [60]. Therefore, in addition to the differences in the signal caused by the DM profile shape, and shown in figure 2, synchrotron signals scale with $\rho_\odot^2$.

[10] Note that we make a conservative choice by choosing a rather extended core. Smaller values of r_s would result in fluxes more similar to those obtained with the NFW profile.

[11] However, depending on the analysis, the uncertainty window on this value can vary in the 0.2–0.8 GeV cm^{-3} range.

JCAP11(2012)038

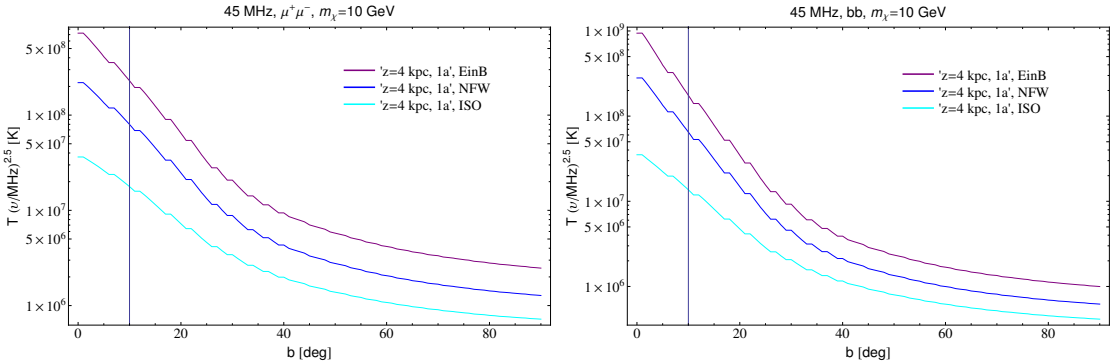

Figure 2. Comparison between synchrotron signals for a DM mass of 10 GeV annihilating to muons (left) and b quarks (right figure) for three DM density profiles: modified Einasto, NFW and ISO thermal profile. $\rho_\odot = 0.43\,\mathrm{GeV\,cm^{-3}}$ is assumed for this plot (see text for the remaining parameters) and propagation of electrons is done using a CR propagation setup as shown in table 1.

3.4 Synchrotron signal for different choices of CR parameters

As discussed above, MED/MIN/MAX sets of CR propagation parameters were derived using a semi-analytical description of CR propagation, and a fit to B/C measurement, with a requirement to produce minimal, medium, and maximal DM generated anti-proton fluxes, at a Solar position. These models were recently reanalysed in [61], where whole sky radio data together with B/C measurements where considered, testing therefore impact of these parameters on electron population, and its synchrotron emission in various regions in the Galaxy. This work concludes that both MIN and MAX models are disfavored by radio data towards the galactic anti-centre. Demanding consistency with B/C nuclei data, it is found that small halo sizes $L_h \sim 1$ kpc are essentially excluded (see also [26]), but also large values $L_h \gtrsim 15$ kpc show some tension with radio data, arguing that MIN/MAX sets of parameters present somewhat extreme choices when compared to observations complementary to CR nuclei data.

In parallel to the above mentioned analysis based on semi-analytical approaches, we also use results of three analysis based on a numerical calculation with the `GALPROP` code [24–26]. In [24] the `GALPROP` code is used to derive a set of CR parameters which provide a good fit to the CR data, and at the same time reproduce the gamma-ray data well. In a parallel work, [25], a full Bayesian analysis of a fit of CR models is made using `GALPROP` to confront CR data and to derive the best fit model and its scatter. It is shown that gamma-ray predictions of such model are consistent with the *Fermi* LAT gamma-ray measurement. We will use the best fit model from [25], and few models within a 2 sigma scatter of the Bayesian analysis, see table 1. We show a comparison of synchrotron signal calculated with these choices of CR propagation parameters in figure 3. The `GALPROP` based parameter sets in general have lower values of parameters δ and consequently higher values K_0 are obtained in a fit to B/C data. That in turn means that diffusion is higher in this set of models, i.e. electrons diffuse out of our ROI, and contribute instead more at higher latitudes, as seen in figure 3.

A study in [26] has shown, however that some models with re-acceleration ($v_a \neq 0$, similar to the case 1a above) are in tension with the large set of radio data. The main reason for this is that production of CR secondary electrons is enhanced in this case and produces too strong radio emission at low frequencies. We therefore consider also a plain diffusion

JCAP11(2012)038

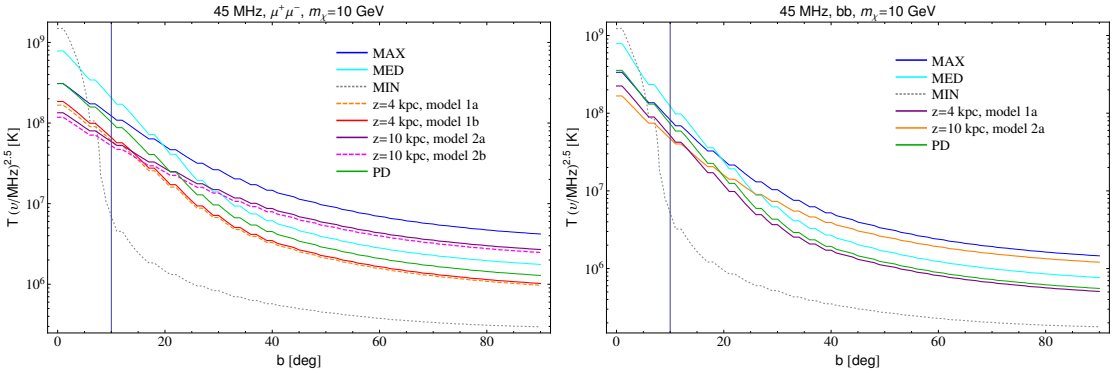

Figure 3. Comparison between synchrotron signals for a DM mass of 10 GeV annihilating to muons (left) and b quarks (right figure) for different CR propagation setups, detailed in table 1. NFW DM profile is assumed here.

model (PD) often used in literature and shown to be consistent with the radio data in [26].

In the remainder of the text we will adopt the MED model together with the NFW profile and $\rho_\odot = 0.43\,\mathrm{GeV\ cm^{-3}}$ as an moderately optimistic scenario, and the '1a', `GALPROP` based CR propagation model, together with the Isothermal profile and $\rho_\odot = 0.3\,\mathrm{GeV\ cm^{-3}}$ as a moderately conservative setup.

3.5 Synchrotron signal for different magnetic field choices

In this section we study how DM limits change depending on the assumptions of the overall normalisation of the magnetic field in our ROI. It has already been noticed (see e.g. [17]) that for a fixed electron injection spectrum there exists an optimum value for the magnetic field which maximises the synchrotron flux at a given synchrotron frequency. However in this section we want to understand this fact in more detail.

As can be seen in eq. (2.18), the magnetic field influences the flux through the energy losses, and through the electron energy. In principle, the electron spectrum dN/dE affects the maximisation of the flux with respect to the magnetic field B. A way to see this is the following: in the assumption of considering a one-to-one correspondence between the emitted synchrotron frequency ν and the electron energy E, (see eq. (2.16)), for a given value of the magnetic field B, the correspondent E could be disfavored (or not available) by the electron spectrum produced by the DM. However, as in this study we are going to work with synchrotron data with frequency of 45 MHz, and magnetic fields $\gtrsim 6\ \mu$G, the electron energies producing those desired frequencies are always smaller than 1 GeV, which can perfectly be produced by our DM candidates in the range [1-200] GeV. So in practice, for our analysis, the only dependence on B that matters are encoded in the energy losses. Indeed, given a specific frequency ν, and a given annihilation channel, it can be expressed in the following form:

$$F(\nu, B) \propto \left(\frac{B^2}{\alpha + B^2}\right) \frac{1}{\sqrt{B}}\,, \tag{3.6}$$

where α represents here the rest of energy-losses, here assumed to be only IC. Note that since both synchrotron and IC losses scale with energy as E^2, the energy dependence cancels in this particular analysis. From (3.6) one observes two extremal cases: one in which

JCAP11(2012)038

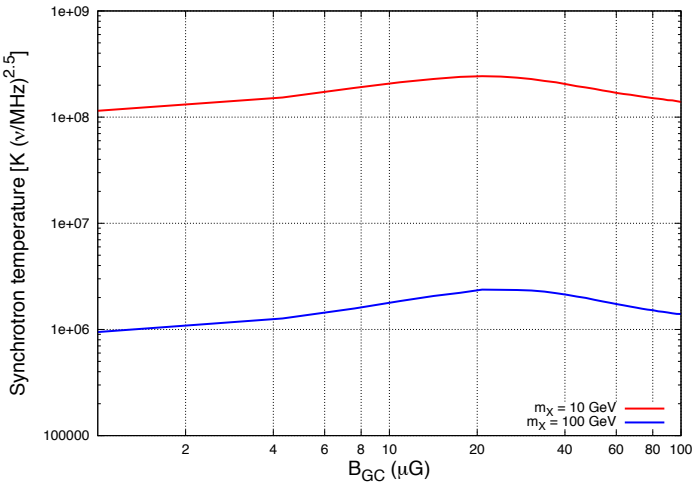

Figure 4. Flux predicted at 10 deg off the GC, as a function of the value of magnetic field at the GC (roughly, at our ROI, we have $B_{\rm ROI} \approx 0.5 B_{\rm GC}$). Lines represent the results in the semi-analytical approach. We assume a DM annihilating directly to electrons, using the NFW profile and the MED diffusion model.

synchrotron loss is negligible with respect to the rest of energy losses, for which the flux scales with B as $F \sim B^{3/2}$, thus increasing as B increases, and the other, in which synchrotron is actually the dominant energy loss, after which the flux scales as $F \sim 1/\sqrt{B}$, thus decreasing as B increases. In other words, there will be an intermediate value of the magnetic field for which synchrotron becomes the dominant energy loss, and this value is actually the one maximising the flux.

Figure 4 shows the shape of synchrotron flux as a function of the value of magnetic field at GC. Taking into account only IC (apart from synchrotron of course), one can have an idea about the maximum of the flux already by direct differentiation of (3.6), assuming the values of α correspondent to this case. The value of B for which the flux is maximal scales as $B_{\rm GC}^{\rm max} \propto \sqrt{U_{\rm rad}}$. For $U_{\rm rad} = 8\,{\rm eV/cm^3}$, $B_{\rm GC}^{\rm max} \simeq 26\ \mu$G.

In the following we will show DM limits using two cases for magnetic field configurations. The first one, a standard $B_{\rm GC} \simeq 10\ \mu$G value in our region of interest is assumed, and the second case will be the normalisation which maximises the synchrotron signal, i.e. $B_{\rm GC} \simeq 26\ \mu$G.

4 Other indirect constraints

In the following we will compare the limits we derive from considering radio data to i) those derived by the *Fermi* LAT collaboration from the non-observation of dwarf spheroidal Galaxies (dSphs) in gamma-rays [19] and ii) constraints based on the measurement of the CMB anisotropy spectra [20]. These limits are among the strongest to date and uncertainties involved in their calculation are complementary to the ones derived in this work.

The main strength of considering dSphs is that they are DM-dominated and lack active astrophysical production of gamma-rays. We will refer to an analysis of the *Fermi* LAT data which, for the first time, combines multiple Milky Way satellite galaxies in a single joint likelihood fit and includes the effects of uncertainties in J factors (line of sight integrals of DM

JCAP11(2012)038

density squared, which define the DM annihilation rates). The improvements of the limits derived in such an analysis over 10 years of *Fermi* LAT mission was estimated in [62]. In the low-energy regime, the sensitivity increases as roughly the square-root of the integration time. However, in the high-energy (limited background regime) the LAT sensitivity increases more linearly with integration time. Thus, 10 years of data could provide a factor of $\sqrt{5}$ to 5 increase in sensitivity. Additionally, new optical surveys (such as Pan-STARRS[12] and the Dark Energy Survey[13]) could provide a factor of 3 increase in the number of detected dSphs corresponding to an overall increased constraining power $\sqrt{15}$ to 15. As we focus mainly on DM masses $\lesssim 100\,\mathrm{GeV}$, we will use $\sqrt{15}$ to illustrate potential improvement in our plots.

In order to translate these limits in terms of democratic couplings to leptons and hadrons (shown in figures 6 and 7) we use i) the limits to τ channel worsened by a 1/3 branching to this channel; dSphs constraints on μ are significantly weaker (this likely holds true also for the e channel, however these limits were not published) and ii) limits on b quark states, as the gamma-ray spectra are very similar for all quark channels.

CMB constraints arise from redshifts in the range $100 \lesssim z \lesssim 1000$ [20, 63–66]. The physical effect of energy injection of (exotic) particles around the recombination epoch is that it results in an increased amount of free electrons, which survive to lower redshifts and increases the width of last scattering surface, consequently suppressing the amplitude of some of the oscillation peaks in the temperature and polarisation CMB power spectra. As constraints come from high redshifts well before the formation of any sizeable gravitationally bound structure, this set of constraints does not depend on highly uncertain parameters related to structure formation. Detailed constraints have been recently derived in [20], based on the WMAP (7-year) [67] and Atacama Cosmology Telescope 2008 data [68]. The constraints are somewhat sensitive to the dominant DM annihilation channel: annihilation modes for which a portion of the energy is carried away by neutrinos or stored in protons have a lesser impact on the CMB; on the contrary the annihilation mode which produces directly e^+e^- is the most effective one. The limits on hadronic channels were not derived in this work. We therefore show CMB limits only for the democratic coupling to leptonic states, in which case we combine the published limits to μ and e channels, renormalised by a branching factor of 1/3. We also show the projected sensitivity of the PLANCK telescope in the near future, as calculated in [20].

5 Constraints on Dark Matter Models

5.1 Effective operators

5.1.1 Mono-events at colliders

The very same interactions responsible for DM annihilation in the galactic medium that ultimately can produce synchrotron fluxes, are the ones by which a DM signal could be produced and measured in collider experiments. At LEP, for example, when a pair of electron-positron collides at high energy a plethora of final states are produced. Among these states, the production of a DM candidate χ can be characterised by missing energy and the emission of a single photon [69, 70]. These data can then be used to constrain theoretical models. We

[12] http://pan-starrs.ifa.hawaii.edu/public/.
[13] http://www.darkenergysurvey.org/.

JCAP11(2012)038

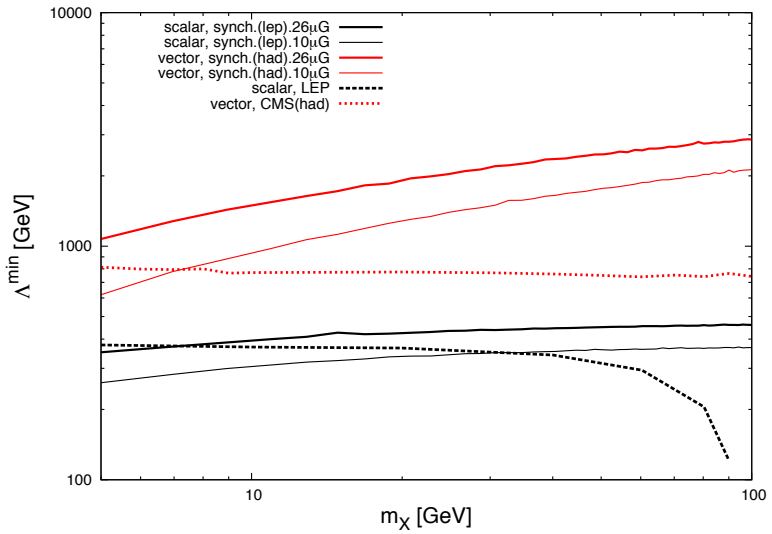

Figure 5. Lower bounds on the effective scales $\Lambda_{l,q}$ from some collider studies, as well as from synchrotron data for a certain choice of parameters (see text for details). "CMS(had)" means CMS bounds to quark operators. Solid lines are bounds from synchrotron radiation data, while dashed lines are bounds from LHC (CMS) or LEP. Red lines correspond to quark operators while black lines correspond to leptonic ones.

first choose to use the powerful machinery of effective field theory (EFT) to capture features from a broad class of WIMP models. In particular we assume that at the relevant energies, the only available degrees of freedom are the dark matter particle itself and the Standard Model. Provided this is true for all energies of interest, the EFT provides a common language which allows one to compare the constraints from different types of experiments [71]. Introducing new physics scales Λ_i one can define effective couplings between (e.g. fermionic) DM to SM fermions f by

$$\mathcal{O}_i^f = \frac{1}{\Lambda_f^2}(\bar{\chi}\Gamma_i\chi)(\bar{f}\Gamma^i f)\,, \tag{5.1}$$

where $\Gamma_i = (1; \gamma_\mu; \gamma_5\gamma_\mu)$ for scalar ($\mathcal{O}_S^f$), vector ($\mathcal{O}_V^f$) or axial ($\mathcal{O}_A^f$) operators respectively. Performing a Monte Carlo simulation studying the signal ($e^+e^- \to \gamma\bar{\chi}\chi$) plus background (e.g. $e^+e^- \to \gamma\bar{\nu}\nu$) processes, one can compare the theoretical background predictions with the real data produced at LEP [8] and put lower bounds on the effective coupling Λ_e. This effective approach can be understood as a limit of microscopic models with heavy mediator (Higgs boson or extra U(1) Z' for instance), discussed in sections 5.2 and 5.3.

A similar study has been made [6, 7] using results from the CDF collaboration with Tevatron [72], and more recently [9] from ATLAS study [73], and by the CMS Collaboration itself [10]. The analogous types of operators defined in eq. (5.1) are used as source of processes like ($\bar{q}q \to j\bar{\chi}\chi$), where q are SM quarks and j stands for a single jet. A mono-jet final state is then used to put constraints on Λ_q and thus on (in this case) hadronic annihilation cross-section, in the very same way as in [8].

As an illustration, we show in figure 5 the limits we obtained on the leptonic and hadronic effective scales, Λ_l and Λ_q, obtained by LEP and CMS as function of the DM mass

JCAP11(2012)038

m_χ in the case of scalar/vectorial interaction with universal leptonic/hadronic coupling. We notice that the bounds on $\Lambda_{f=l,q}$ become weaker as DM mass increases because of the phase space reduction, up to some point in which it is kinematically impossible -given the energies of the experiment- to produce the pair of DM particles (the threshold is of course higher in LHC experiments than at LEP). The lower bounds on $\Lambda_l(q)$ is around 300 GeV (600 GeV) and relatively independent of the DM mass as one measures missing energy. It becomes then interesting to compare this limit to the one derived from synchrotron emission. These bounds obtained by the LEP and CMS can also be converted directly into upper bounds on the leptonic/hadronic annihilation cross-section $\langle\sigma v\rangle_{ee/qq}$ from the inverse processes ($\bar{\chi}\chi \to \bar{e}e/qq$), generated by the operators defined in eq. (5.1) (see appendix A for details).

5.1.2 Synchrotron *vs* Collider and complementary Indirect Detection bounds

In order to model the synchrotron signal of a standard astrophysical origin, a HASLAM 408 MHz map [29] can be used as a template. It is a full sky radio map with the best angular resolution and sensitivity. Indeed, a 408 MHz frequency is well suited to gauge the contribution from the harder population of galactic electrons, while leaving lower frequency maps sensitive to test a possible contribution from softer electrons originating in annihilations of light dark matter candidates.

In [18] it has been shown that by extrapolating the HASLAM data down to 45 MHz, to model astrophysical synchrotron emission, one is left with $\sim 30\%$ residuals when compared to the actual 45 MHz data. Those residuals do not have the proper morphology of a DM signal and therefore no DM detection could be claimed. Based on this analysis it seems reasonable to assume that the current uncertainty (i.e. systematics) in modelling the astrophysical emission is at a level of $\sim$ 30%. However, in our analysis, we do not attempt to model specific astrophysical signals. Instead, we decide to apply a conservative 95% CL DM limits without assuming any contribution from astrophysical background, and which we label *no bckgd*, in the figures and also show how this limits change as a function of the systematic uncertainties on the astrophysical model, expressed as a background uncertainty in % of the data.

Our procedure is to compute the synchrotron flux coming from DM ($F_{\rm DM}$) in our ROI, and then constrain the result with the available data corresponding to that region, $F_{\rm obs}$, by requiring that $F_{\rm DM} \leq F_{\rm obs} + 2\sigma$, where 1σ is the uncertainty considered in each case (see figures 8 and 9). In the case of *no bckgd*, 1σ is the rms temperature noise, taken to be 3500 K.

For illustration, in figure 5 we have included the bounds on Λ_i obtained from synchrotron data at 45 MHz with a 26 and 10 μG magnetic field in our ROI, with the hypothesis that the dark matter signal lies within 5% of uncertainty of the background, and using the NFW+MED set-up. We clearly see that the synchrotron radiation, with the present data, can already give stronger limit on the effective scales, independently on the value of the magnetic field, and is complementary to the bounds from accelerator searches. Indeed, whereas there are no "threshold effect" for synchrotron radiation at large DM mass, one notice that for low masses, in the hadronic channel the bounds becomes weaker. We comment on this behaviour below.

We also translated these limits on Λ_i into limits on annihilation cross sections. We present the result in figures 6 and 7 for different values of the magnetic fields, and natures of the DM couplings, in comparison with limits coming from LEP, CMS, observation of dwarf galaxies by *Fermi* LAT and the measurement of CMB anisotropies by the WMAP and ACT.

JCAP11(2012)038

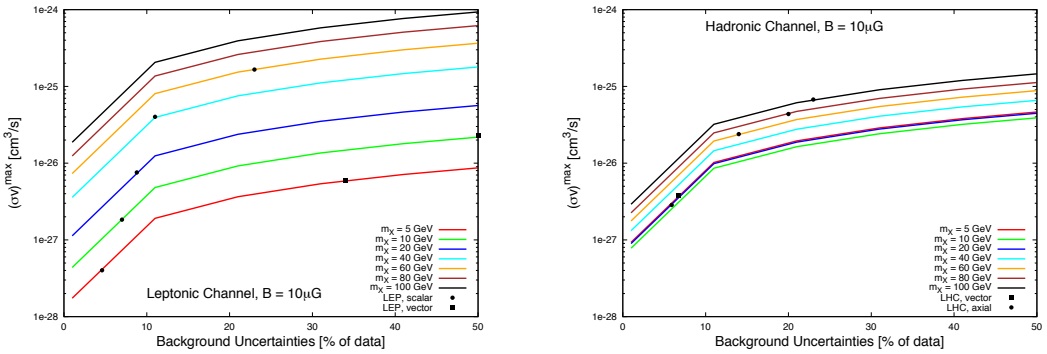

Figure 6. Synchrotron bounds on $\langle\sigma v\rangle$, assuming DM couples democratically to all charged-leptons (left panel) or to all kinematically available quarks (right panel). In both cases, comparison with bounds coming from colliders are shown explicitly. The magnetic field normalisation has been set to 10 μG. Astrophysical setup: MED diffusion model, NFW profile with $\rho_\odot = 0.43\,\mathrm{GeV/cm^3}$. Purple lines represent present (solid line) and 10-years projection (dot-dashed line) limits coming from Dwarf galaxies. Brown line in the left panel represents current DM limits based on the measurement of CMB anisotropies (solid) and near future reach based on the Planck data (dashed line).

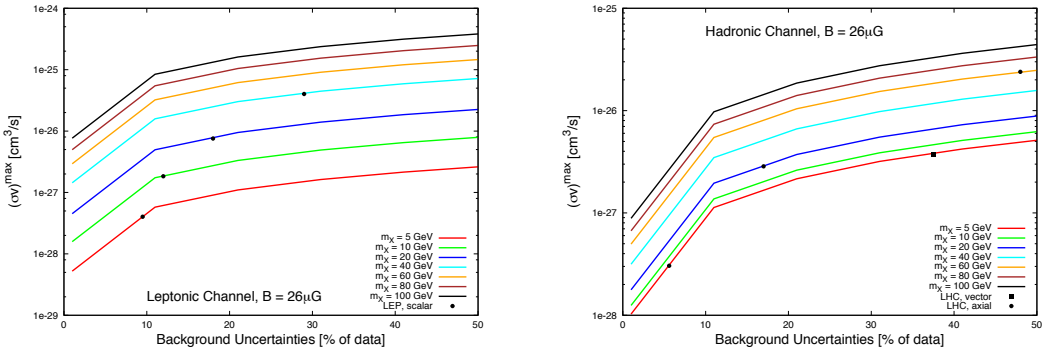

Figure 7. Same as in figure (6), with the same astrophysical setup, but now the magnetic field normalisation has been set to 26 μG.

Comparing the 2 figures, we first notice that the results are not extremely sensitive to the value of the magnetic field (10 or 26 μG) and that synchrotron bounds largely compete with bounds from other type of experiments. Secondly, the hadronic channel gives the weaker bounds on $\langle\sigma v\rangle$, especially at low masses. For low masses, the annihilation into hadronic states gives an electron spectrum much softer, especially after the kinematic closure of the $b\bar{b}$ channel, and radiates much less synchrotron emission than in the case of a pure leptonic channel: a lot of soft electron produced by later decays of final state hadrons will radiate at frequencies lower than 45 MHz and will not be bounded by current radio data. At the high mass end, the bounds coming from indirect detections searches (based on the Galactic synchrotron emission, dwarf Galaxies or CMB) get weaker because the flux of products of

JCAP11(2012)038

DM self-annihilation is proportional to $1/m_\chi^2$. We should also emphasise that even the *very conservative* result, where we supposed that all the data are generated by DM synchrotron, gives already limits competitive with LEP bounds, whereas the 5% uncertainty bounds could give the best limit obtained by an indirect detection experiment.

Concerning the accelerator constraints, from the study of the $\langle\sigma v\rangle$ predictions for different kind of effective interactions (cf. appendix A), one realizes by direct inspection of those expressions that normally the vector operator gives larger values, with respect to the scalar and axial case. This is because its Lorentz structure allows for $\langle\sigma v\rangle$ to develop a term independent on v^2 and proportional to m_χ^2, and thus not suppressed. The consequence of this is that in general, vector interaction produce weaker bounds.

In the comparison with accelerator constraints, one realises that in the case of leptonic channel, the synchrotron bounds in the conservative case of assuming no background, (orange band) is in general as competitive as the bound coming from LEP studies, assuming a vector effective interaction. It starts to be more competitive for masses larger than tens of GeV, and beyond 100 GeV, space of parameter space beyond the reach of the accelerator. In the case of CMS bound from a vector interaction, it is all the way slightly better (for light masses) or similar (for heavier masses) than synchrotron constraints, obviously up to the TeV range where LHC starts loosing sensitivity. The LEP bound coming from a scalar effective operator is however one order of magnitude stronger for light masses of $\simeq 10$ GeV. Furthermore, to have an idea of how well we would need to understand the background in order to render synchrotron more competitive than LEP or CMS, we include in figure 6 a bound assuming that background is known within 5%, at 95% CL. We observe that for these already small uncertainties the synchrotron searches start to be more competitive (in general) than collider bounds, independently of the DM mass (in the case of LEP).

We also show in figure 6 the bounds on hadronic channels, now compared to collider bounds on vectorial and axial interactions. Again, for the conservative case of no background, synchrotron bounds start to be more competitive than collider bounds for m_{DM} of about tens of GeV, in the case of vectorial interaction, for ATLAS as well as for CMS. In the case of axial coupling, collider bounds are always stronger. In the optimistic case of allowing at most 5% of uncertainties in the background, the bounds from synchrotron can exclude those from colliders already at 10 GeV in the case of vectorial interaction. The difference in the behaviour for masses lighter than 5 GeV, with respect to the leptonic case, is due to quark masses thresholds. In the hadronic case, when the $b\bar{b}$ channel opens, it gives an important contribution to the flux, causing the maximum allowed σv value to decrease. Since there no more threshold after the bottom mass (the top is heavier than the ranges considered here), the flux decreases smoothly when m_{DM} increases, as in the the case of leptonic channels (for which all thresholds are below ~ 2 GeV).

We run a similar analysis in figure 7, with the "optimum" choice of magnetic field, $B_{\rm GC} = 26\ \mu$G, studied in the previous section. We see in this case an improvement of synchrotron bounds with respect to collider bounds. If the DM interaction is vectorial, the synchrotron can exclude the collider bounds for all the mass range, for the case of leptonic channels, even in the conservative background assumption. For hadronic channel the exclusion is already effective for masses beyond 10 GeV. As before, depending on our knowledge of the background, synchrotron could be able to exclude current collider bounds on axial interaction.

JCAP11(2012)038

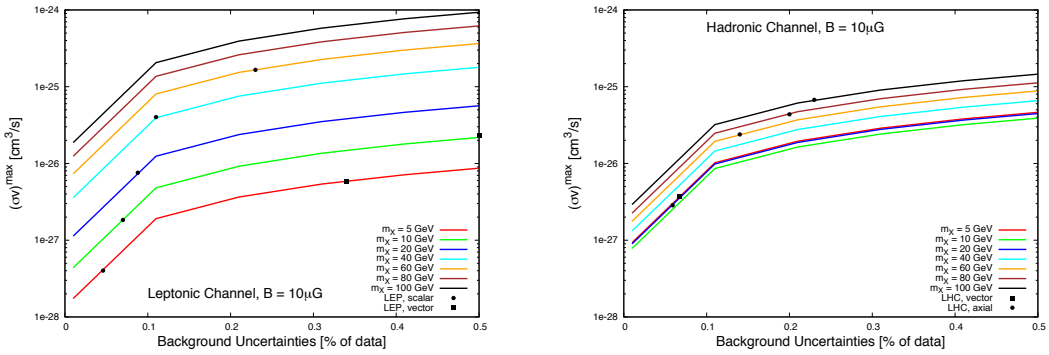

Figure 8. Bounds on $\langle\sigma v\rangle$ coming from DM synchrotron fluxes as function of background uncertainties assumptions [in % of data] at 95%CL. Different choices for DM mass are plotted. Dots represent the bounds coming from LEP (left-panel), specifically the case of a democratic coupling with leptons (as the synchrotron bounds) and assuming a scalar interaction; or LHC-ATLAS (right-panel), for democratic coupling with quarks, for both vector and axial interactions. The magnetic field normalisation has been set to 10 μG. Astrophysical setup: MED diffusion model, NFW profile with $\rho_\odot = 0.43\,\mathrm{GeV/cm^3}$.

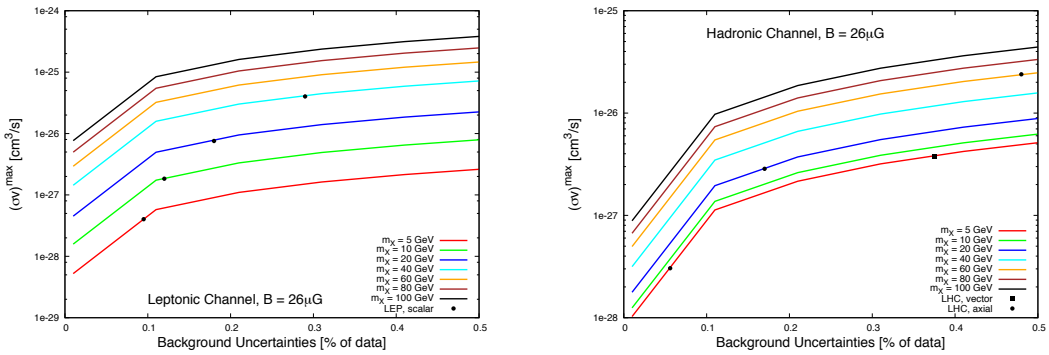

Figure 9. The same as in figure 8, with the same astrophysical setup, but with the magnetic field normalisation set to 26 μG.

To summarise, our analysis shows that synchrotron bounds, beside being complementary, could be potentially stronger than those obtained from collider searches, and that extensive studies of the astrophysical background at these frequencies is well motivated. To this purpose consistent progress is expected to be achieved in the next years with the new high quality data coming from the PLANCK mission[14] and from low frequency arrays like LOFAR,[15] which will survey low frequencies 10-240 MHz and is the pathfinder for the future SKA facility.[16] It is also worth noticing that the analysis of the Galactic diffuse emission of the *Fermi* LAT will bring further insights on CR production and propagation processes, additionally constraining the Galactic synchrotron emission (for a current status see, [24, 26]). We leave such dedicated studies for future works.

The impact of the control of the background is illustrated in figures 8 and 9 where we

[14] http://www.rssd.esa.int/index.php?project=Planck.
[15] http://www.lofar.org/
[16] http://www.skatelescope.org/.

JCAP11(2012)038

show the level of precision that would be required to be able to exclude/probe the effective models for different DM masses. The dots on top of the iso-mass lines represent collider bounds for the corresponding mass. The lines with no dots correspond to cases for which the synchrotron limit is (for the whole range of uncertainties) stronger or weaker than the respective collider bounds. So, for each iso-mass, the regions on the left-hand-side of the dots correspond to situations for which the synchrotron bounds are stronger, and on the right-hand-sides, to stronger bounds from colliders. For instance, the case of a 20 GeV DM candidate with scalar leptonic interactions is more constrained by radio synchrotron data, provided uncertainties on the background are smaller than 10%, than by the LEP data (figure 8 – left). For vector-like interactions, the synchrotron bounds were always stronger, no matter what the uncertainties considered, for DM masses above 5 GeV and assuming $B_{\rm GC} = 10$ μG (see figure 8). For $B_{\rm GC} = 26$ μG, (figure 9 – left), the synchrotron bounds are always better than collider bounds, in the case of vector interaction. The conclusion is that, for uncertainties on the background of 5%, or less, the synchrotron bounds are stronger than the LEP bounds, independently of the DM mass and of the nature of the effective DM coupling to SM leptons.

Looking at hadronic channels, we see that for uncertainties of 5% (figure 8 – right), the synchrotron bounds are stronger than those coming from LHC, if the interaction is axial-like and for $B_{\rm GC} = 10$ μG. The case of $B_{\rm GC} = 26$ μG (figure 9 – right) is of course even better, and for $m_\chi \simeq 60$ GeV, even with background uncertainties of 40%, the synchrotron can rule out the collider bounds. If the interaction is vector-like, the bounds from colliders are weaker, as we discussed above, and for masses of 10 GeV and beyond, synchrotron bounds are always stronger.

5.2 Higgs portal

The effective operator approach is quite powerful, as it encompasses many possible underlying microscopic theories with a minimum set of free parameters, but it has its limitations. This is in particular the case when other degrees of freedom become relevant at the energies considered (be in the early universe or at colliders). Also, a microscopic theory in general predicts some specific relations between the various effective couplings to which it reduces at low energies. Finally, a specific theory may have implications or predictions, that are hidden in an effective operator approach.[17] For all these reasons, it is of interest to consider more fundamental models of dark matter. Hence the purpose of this section, which is to take our analysis of constraints from synchrotron radiation to a more microscopic level.

Generally speaking, any fundamental theory that addresses the abundance of WIMPs requires two fundamental ingredients:

- A candidate. It should be a massive and weakly interacting particle, stabilised by a (discrete or continuous, possibly gauged) symmetry.
- A mediator. This component can be an existing particle or a companion of the dark matter candidate naturally present by construction. For instance it could be a particle (the Higgs, or a new scalar) or a new gauge boson (Z').

In this and the following section, we study the two simplest extensions of the SM with DM particles, the so-called Higgs-portal and Z', or kinetic mixing, portal. In particular we

[17] See [74] for two very recent examples of mono-jet/single-photon studies on specific microscopic models.

JCAP11(2012)038

determine their radio synchrotron emission, and combined with the WMAP constraint, we analyse the parameter space that is experimentally allowed.

The perhaps simplest extension of the SM consists in the addition of a real singlet scalar field, that couples to the SM through the Higgs field. In this case, the mediator is the Higgs boson itself, and the model is usually called the "Higgs portal". Although it is logically possible to generalise this scenario to more than one singlet, the simplest case of one singlet already provides a very useful framework to analyse the generic implications of an augmented scalar sector. The most general renormalisable potential involving the SM Higgs doublet H and the singlet S is

$$\begin{aligned}\mathcal{L} \supset & -\frac{\mu_S^2}{2}S^2 - \frac{\lambda_S}{4}S^4 - \frac{\lambda_{HS}}{4}S^2 H^\dagger H \\ & -\frac{\kappa_1}{2}H^\dagger H S - \frac{\kappa_3}{3}S^3\end{aligned} \tag{5.2}$$

For the case of interest, the S particle must be stable to be a dark matter candidate. This is achieved by imposing a Z_2 symmetry on the model, $S \to -S$, with H unchanged, thereby eliminating the κ_1 and κ_3 terms. We also require that the true vacuum of the theory satisfies $\langle S \rangle = 0$, thereby precluding mixing of S and the SM Higgs boson (and the existence of cosmologically problematic domain walls). In this case, the mass of the S is simply

$$m_S^2 = \mu_S^2 + \frac{\lambda_{HS}}{4}v^2 \tag{5.3}$$

with $v = 246\,\mathrm{GeV}$ is the vev of the Higgs field, and the H-SS coupling is

$$\mathcal{C}_{HSS} = -\frac{\lambda_{HS} M_W}{2g}\,, \tag{5.4}$$

where M_W is the W-boson mass and g the SU(2) gauge coupling.

Different aspects of scalar singlet extension of the SM has already been studied in [75] whereas a preliminary analysis of its dark matter consequences can be found in [76]. Some authors considered the possibility of explain the DAMA and/or COGENT excesses [77], whereas several authors looked at the consequences of earlier XENON100 data [77]. Other authors looked at the consequences on the invisible Higgs width at LHC [78] or the restriction of the parameter space due to an hypothetical 125 GeV Higgs signal [79]. Other studies probed the model by indirect searches [80–82] of $\gamma-$ray or positrons, but there is not yet and analysis of constraints from synchrotron radiation.

We show in figure 10 (left) the synchrotron flux in our ROI expected for the Higgs-portal model for two different representative values of the magnetic fields (10 μG and 26 μG) as a function of the dark matter mass, for a Higgs of 125 GeV and candidates that respect the WMAP constraint (at 5σ). We also represented the limits we obtain based on the 45 MHz radio data in the two cases discussed above: when we supposed that all the signal is due to synchrotron radiation (labelled "no backgr", extremely conservative case A), and when we allowed the signal to lie within the 5% of uncertainties due to modelling of an astrophysical background of standard origin (labelled "5% background, less conservative case B). We do this for two typical astrophysical setups, as studied above in the paper: a NFW dark matter profile, with MED diffusion model and a local normalisation of a DM density

JCAP11(2012)038

of $\rho_\odot = 0.43\,\mathrm{GeVcm}^{-3}$, and on the other hand, an Isothermal profile, with diffusion model "1a"[18] (see table I) and a local normalisation of a DM density of $\rho_\odot = 0.3\,\mathrm{GeVcm}^{-3}$.

For the (NFW + MED) setup, we observe that, in the more conservative case, dark matter masses below $\simeq 20\,\mathrm{GeV}$ are already close to be excluded for small values of the magnetic fields ($B = 10\,\mu$G), and even DM masses below 40 GeV are excluded for $B = 26\,\mu$G. This result is better that the one can obtain based on the *Fermi* LAT gamma-ray and PAMELA positron data [80, 81], which is one of the important results of our analysis. Indeed, dwarf galaxies study exclude only $m_s \lesssim 10\,\mathrm{GeV}$ [82]. Also, with the same assumption on the CR propagation model (MED), one can see that the current synchrotron constraints already reach a higher level of precision than those based on the PAMELA positron data (see figure 2 of [81]) and gives even better result than the projected AMS-02 sensitivity (see figure 3 of [81]) if the DM signal lies in the 10% uncertainty of the background. The exclusion by synchrotron emission is also similar to the one sets by the *Fermi* LAT data on galactic gamma-rays [80].

In case B, allowing the DM signal to stay within 5% uncertainty, we observe that mainly all the parameter space of the model is excluded for masses lighter than 100 GeV, except in two narrow regions, namely near the Higgs pole ($2m_s \simeq m_H$), and just above the $W^\pm$ threshold ($m_S \simeq 80\,\mathrm{GeV}$). Indeed, in a region around the pole, the enhancement of the cross section due to the Breit-Wigner form of the amplitude implies that a very low value of $\mathcal{C}_{HSS}$ is required to match the WMAP constraint, $\langle\sigma v\rangle \sim 3\times10^{-26}$ cm^{3}s^{-1}, as the amplitude is proportional to

$$\mathcal{M} \propto \frac{\mathcal{C}_{HSS}}{E_{CM}^2 - m_H^2 + i\Gamma_H m_H}$$

with E_{CM} being the CM energy of the annihilating S pair. However, the synchrotron radiation produced in the Galaxy comes from S essentially at rest, whereas its kinetic energy at freeze-out was about $T \simeq m/25$. Consequently, for annihilation in the Galaxy, the points respecting WMAP are away from the pole and the enhancement is not sufficient to counterbalance the small value of $\mathcal{C}_{HSS}$: the annihilation cross section is $\langle\sigma v\rangle_{v\simeq 200\mathrm{kms}^{-1}} \simeq 10^{-29}\mathrm{cm}^3\mathrm{s}^{-1}$. The synchrotron flux is thus largely reduced in this region of the parameter space, explaining the first dip seen in figure 10.

The second dip seen in figure 10 is also due for kinetic reasons. Indeed, as soon as the $W^\pm$ channel is open, the $W^\pm$ final state is by far the dominant one due to the large gauge coupling of the W's to the Higgs. Thus, for singlet candidate with a mass slightly below $M_{W^\pm}$, its kinetic energy at the freeze-out temperature allows its annihilation into $W^\pm$, even for small values of $\mathcal{C}_{HSS}$, as the process is dominated by the gauge interaction and not the Yukawa ones (the $b\bar{b}$ final state is the dominant one for $m_s \lesssim M_{W\pm}$). However, nowadays, such slightly lighter singlet cannot annihilate into $W^\pm$, as its kinetic energy has dropped below the threshold. Consequently, its main decay in the Galaxy is into $b\bar{b}$ pairs, but with a small value of $\mathcal{C}_{HSS}$, again giving a very low synchrotron emission. These two narrow regions are thus very difficult to observe with this type of signal. We should perhaps emphasize that the arguments we gave above are valid for any kind of, indirect detection prospect (γ or antimatter) and is not specific to synchrotron.

[18] Those models, where Alfvén velocity can not be neglected — at least for our energies of interest-, can not be studied directly by the Semi-Analytical approach followed here. Instead, we use the full numerical analysis to estimate suppression factors in every annihilation channel, and from there we derive the new bounds.

JCAP11(2012)038

We also show in figure 10 (right) the precision on the background that is required to be able to exclude/discover a synchrotron signal for a singlet DM through the Higgs portal. We observe that, except in the two narrow pole regions discussed above (where an unreasonable precision would be needed to measure any type of fluxes), if 5-10% (at 95% CL) of the observed flux is due to synchrotron radiation, the model is already excluded for $B_{\rm GC} = 26$ μG. For $B_{\rm GC} = 10$ μG one needs to suppose that $\lesssim 5\%$ of the measurement is due to the annihilation of the singlet to exclude the model. This result is then essentially independent of the precise value of $B_{\rm GC}$.

Of course, these conclusions are weaker for the second astrophysical setup considered here, where electrons diffuse more and the DM is less cusped in the inner galaxy. Independently of the magnetic field used, the model is excluded if background uncertainties are of 1% (at 95% CL) or less, for DM masses below 40 GeV. Again, as commented above for the case of the effective approach, an equally valid option for the DM distribution, as can be the Einasto profile (not shown here), can enhance the signal by a factor 3, allowing us to claim stronger conclusions about the exclusion power of the synchrotron radiation.

Finally, some words regarding the comparison with XENON100 bounds. It was shown in [83] that in general the scalar singlet model is disfavoured by XENON100 data in the region of low ($\lesssim M_W$) masses, except around the region of the Higgs-pole, and also for $m_\chi \lesssim 8$GeV, where XENON100 starts loosing sensitivity. In this sense, synchrotron bounds are complementary to XENON100 bounds, as they are able to constrain the region of very low mass, as well as the region of large mass ($\gtrsim M_W$), given some reasonable knowledge about the background. For illustration, we show in figure 11 the exclusion of the coupling λ_{HS} due to synchrotron data, assuming a value of 26μG for the magnetic field in our ROI, and compare it directly with the exclusion coming from XENON100. We see that effectively for $m_\chi \gtrsim M_W$, synchrotron constraints are stronger than those of XENON100, assuming reasonable backgrounds uncertainties of 20% at 95%CL. Also, as expected, synchrotron bounds (even in the conservative case of no-background) do better than XENON100, for masses $m_\chi \lesssim 12$ GeV. For completeness we also included in the analysis a comparison with bounds coming from LHC [79], assuming the Higgs can decay into DM particles with a branching ratio of 40%. In this case, everything which is to the left of the brown curve is excluded. In the region of relatively low masses those bounds are comparable to the ones coming from XENON.

One should notice that our analysis can also be applied to a vectorial dark matter through the Higgs portal [85]. Indeed, one can consider, to first approximation, a massive vector as a scalar particle with three internal degrees of freedom. In this case the synchrotron flux should be a factor $\simeq 3$ times greater than the one we obtained for the simplest singlet scalar extension. One thus deduces that the constraints we would obtain would be even stronger than the one we presented in the singlet scalar scenario.

5.3 Extra U(1)

Neutral gauge sectors with an additional dark $U'(1)$ symmetry in addition to the Standard Model (SM) hypercharge $\mathrm{U}(1)_Y$ and an associated Z' are among the best motivated extensions of the SM, and give the possibility that a dark matter candidate lies within this new gauge sector of the theory. Extra gauge symmetries are predicted in most Grand Unified Theories (GUTs) and appear systematically in string constructions. Larger groups than SU(5) or SO(10) allow the SM gauge group and $\mathrm{U}(1)'$ to be embedded into bigger GUT

JCAP11(2012)038

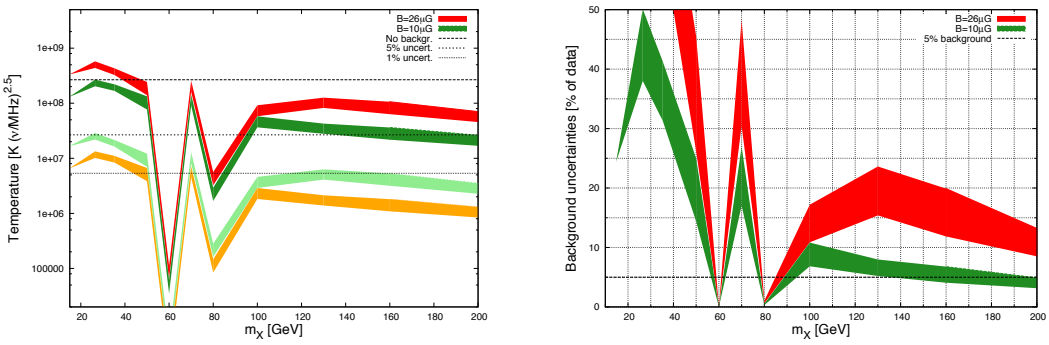

Figure 10. Left) Synchrotron flux at 45 MHz produced from the Higgs-portal model. For every $m_{\rm DM}$, the coupling $\lambda_{\rm HSS}$ is scanned while requiring that the relic abundance respects WMAP constraint at 5σ. We presented the result for a magnetic field profile normalised to 26μG (red, orange) and 10μG (green, light green). Dashed line shows bound coming from data, assuming no background; whereas dotted line shows the bound assuming a full background with uncertainties of 5% (see text for details). Red and green bands are for NFW+MED+$\rho_\odot = 0.43\,{\rm GeV\,cm^{-3}}$ astrophysical setup, while light-green and orange correspond to ISO+1a model+$\rho_\odot = 0.3\,{\rm GeV\,cm^{-3}}$. Right) Maximum background uncertainties allowed to exclude a point in the parameter space of the model, with the same conventions as above.

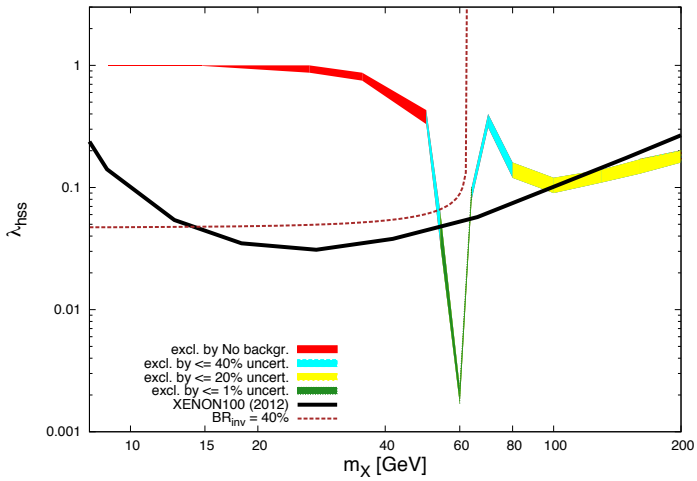

Figure 11. Constraints on the coupling λ_{HSS} for the Higgs-portal model, as a function of DM mass m_χ. Different colours show the exclusion by synchrotron data, assuming: Red) Excluded by No-background choice, Blue) Excluded by uncertainties of 40%, Yellow) Excluded by uncertainties of 20%, and Green) Excluded by uncertainties of less than 1%. Here we assume 26μG for the magnetic field at GC, as well as NFW+MED set-up. Black solid line shows the exclusion by XENON100, while the black dashed line is the LHC limit assuming that at most a 40% invisible BR of the Higgs.

JCAP11(2012)038

groups. Brane-world $U'(1)$s are special compared to GUT $U'(1)$'s because there is no reason for the SM particles to be charged under them; for a review of the phenomenology of the extra $U'(1)$s generated in such scenarios see e.g. [86]. In such framework, the extra Z' gauge boson would act as a portal between the "dark world" (particles not charged under the SM gauge group) and the "visible" sector.

Several papers considered that the key of the portal could be the gauge invariant kinetic mixing $(\delta/2)F_Y^{\mu\nu}F'_{\mu\nu}$ [87]. One of the first models of dark matter from the hidden sector with a massive additional $U'(1)$, mixing with the SM hypercharge through both mass and kinetic mixings, can be found in [88]. The DM candidate ψ_0 could be the lightest (and thus stable) particle of this secluded sector. Such a mixing has been justified in recent string constructions [90–93], but has also been studied within a model independent approach [89, 94, 95]. For typical smoking gun signals in such models, like a monochromatic gamma-ray line, see [96].

The matter content of any dark $\mathrm{U}(1)_D$ extension of the SM can be decomposed into three families of particles:

- The *Visible sector* is made of particles which are charged under the SM gauge group $\mathrm{SU}(3) \times \mathrm{SU}(2) \times U_Y(1)$ but not charged under $U_D(1)$ (hence the "dark" denomination for this gauge group).

- the dark sector is composed by the particles charged under $U_D(1)$ but neutral with respect to the SM gauge symmetries. The dark matter (ψ_0) candidate is the lightest particle of the dark sector.

- The *Hybrid sector* contains states with SM *and* $U_D(1)$ quantum numbers. These states are fundamental because they act as a portal between the two previous sectors through the kinetic mixing they induce at loop order.

From these considerations, it is easy to build the effective Lagrangian generated at one loop:

$$\begin{aligned}\mathcal{L} = \mathcal{L}_{\mathrm{SM}} - \frac{1}{4}\tilde{B}_{\mu\nu}\tilde{B}^{\mu\nu} - \frac{1}{4}\tilde{X}_{\mu\nu}\tilde{X}^{\mu\nu} - \frac{\delta}{2}\tilde{B}_{\mu\nu}\tilde{X}^{\mu\nu} \\ + i\sum_i \bar{\psi}_i\gamma^\mu D_\mu\psi_i + i\sum_j \bar{\Psi}_j\gamma^\mu D_\mu\Psi_j\,,\end{aligned} \tag{5.5}$$

$\tilde{B}_\mu$ being the gauge field for the hypercharge, $\tilde{X}_\mu$ the gauge field of $U_D(1)$ and ψ_i the particles from the hidden sector, Ψ_j the particles from the hybrid sector, $D_\mu = \partial_\mu - i(q_Y\tilde{g}_Y\tilde{B}_\mu + q_D\tilde{g}_D\tilde{X}_\mu + gT^aW_\mu^a)$, T^a being the SU(2) generators, and

$$\delta = \frac{\tilde{g}_Y\tilde{g}_D}{16\pi^2}\sum_j q_Y^j q_D^j \log\left(\frac{m_j^2}{M_j^2}\right) \tag{5.6}$$

with m_j and M_j being hybrid mass states [97] .

Notice that the sum is on all the hybrid states, as they are the only ones which can contribute to the $\tilde{B}_\mu$, $\tilde{X}_\mu$ propagator. After diagonalising of the current eigenstates that

JCAP11(2012)038

makes the gauge kinetic terms of eq. (5.5) diagonal and canonical, we can write after the $\mathrm{SU}(2)_L \times \mathrm{U}(1)_Y$ breaking[19]

$$\begin{aligned} A_\mu &= \sin\theta_W W^3_\mu + \cos\theta_W B_\mu \\ Z_\mu &= \cos\phi(\cos\theta_W W^3_\mu - \sin\theta_W B_\mu) - \sin\phi X_\mu \\ Z'_\mu &= \sin\phi(\cos\theta_W W^3_\mu - \sin\theta_W B_\mu) + \cos\phi X_\mu \end{aligned} \tag{5.7}$$

with, to first order in δ,

$$\begin{aligned} \cos\phi &= \frac{\alpha}{\sqrt{\alpha^2 + 4\delta^2\sin^2\theta_W}} \quad \sin\phi = \frac{2\delta\sin\theta_W}{\sqrt{\alpha^2 + 4\delta^2\sin^2\theta_W}} \\ \alpha &= 1 - M^2_{Z'}/M^2_Z - \delta^2\sin^2\theta_W \\ &\quad \pm\sqrt{(1 - M^2_{Z'}/M^2_Z - \delta^2\sin^2\theta_W)^2 + 4\delta^2\sin^2\theta_W} \end{aligned} \tag{5.8}$$

and + (-) sign if $M_{Z'} < (>) M_Z$. The kinetic mixing parameter δ generates an effective coupling of SM states ψ_{SM} to Z', and a coupling of ψ_0 to the SM Z boson which induces an interaction on nucleons. Developing the covariant derivative on SM and ψ_0 fermions state, we computed the effective $\psi_{\mathrm{SM}}\psi_{\mathrm{SM}}Z'$ and $\psi_0\psi_0 Z$ couplings to first order[20] in δ and obtained

$$\mathcal{L} = q_D\tilde{g}_D(\cos\phi\ Z'_\mu\bar{\psi}_0\gamma^\mu\psi_0 + \sin\phi\ Z_\mu\bar{\psi}_0\gamma^\mu\psi_0). \tag{5.9}$$

We took $q_D\tilde{g}_D = 3$ trough our analysis, keeping in mind that our results stay completely general by a simple rescaling of the kinetic mixing δ.

We show in figure 12 the synchrotron flux emitted at 45 MHz for different values of Z' masses after a scan on $(m_{DM} = m_{\psi_0}; \delta)$ for points respecting the WMAP and electroweak precision tests (including Z width, ρ parameter $g-2$ and atomic parity violation constraint). We do this exercise for the astrophysical NFW+MED setup. We first observe a similar behaviour to that in the Higgs portal around two poles, M_Z and $M_{Z'}$. Indeed, the two channels giving a good relic density are the $s-$channel exchange of the Z' bosons for $m_{DM} \simeq M_{Z'}/2$. We have restricted the fluxes for each $M_{Z'}$ in windows to avoid juxtapositions of the fluxes. However, when $M_{Z'} \simeq 200\,\mathrm{GeV}$ the value of the flux begins to be quite weak for regions of other parameter space far from the pole region, due to the reduced factor in the amplitude square of the $s-$channel process $\bar{\psi}_0\ \psi_0 \to Z' \to SM\ SM$ $|\mathcal{M}|^2 \propto 1/M^4_{Z'}$ which is almost a factor 1/6 compared to a 125 GeV Higgs exchange, factor that we recover in the synchrotron fluxes. In this case one needs a precision better than 5% to be able to distinguish a dark matter signal if $m_{DM} \gtrsim 120\,\mathrm{GeV}$ (see figure 12 – right).

One observes that the conclusions we have obtained for the Higgs portal are also quite valid for the Z' portal too, except that there are different fine-tuned pole regions for each mass of the Z'. The fluxes in both cases lie in a region of parameter space between 5% to 100% of the measured flux and could thus be probed in a near future.

6 Conclusions and prospects

In this work, we derived the constraints on synchrotron emission from the secondary products of dark matter annihilation in our Galaxy, based on the radio 45 MHz data. We expanded

[19] Our notation for the gauge fields are $(\tilde{B}^\mu, \tilde{X}^\mu)$ before the diagonalization, (B^μ, X^μ) after diagonalization and (Z^μ, Z'^μ) after the electroweak breaking.

[20] One can find a detailed analysis of the spectrum and couplings of the model in the appendix of ref. [98].

JCAP11(2012)038

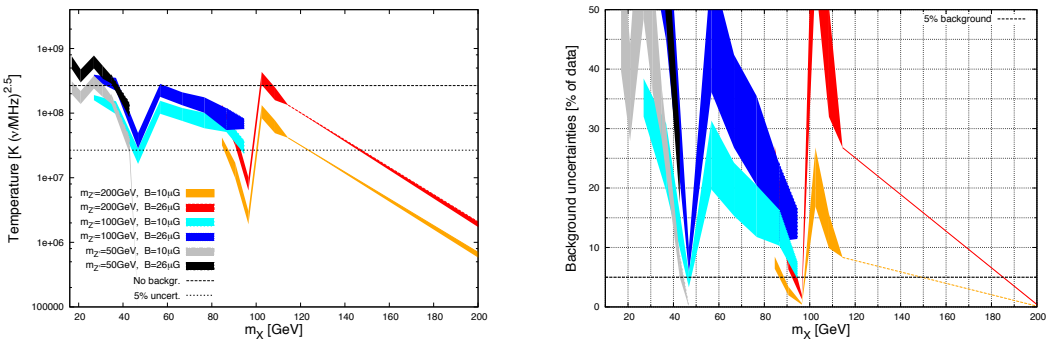

Figure 12. Left) Scatter plot of predictions for synchrotron flux coming from a Z'-portal model defined in (5.5). For every $m_{\rm DM}$, the coupling δ is scanned while requiring good relic abundance, for different Z' masses, $m_{Z'}$. A frequency of 45 MHz was used, assuming a magnetic field profile normalised to 26μG (dark colours) and 10μG (light colours). Dashed line shows bound coming from data, assuming no background; whereas dotted line shows the bound assuming a full background with uncertainties of 5% at 95%CL. Right) Maximum background uncertainties allowed to be able to exclude a point in the parameter space of the model.

upon the current literature in several aspects: a) by using both a semi-analytical approach to model the particle propagation in the intergalactic medium [34, 35], and a full numerical analysis based on the `GALPROP` code [21, 22], benefiting from the strengths of both in particular aspects of the work, b) considering intermediate Galactic latitudes, where the DM profiles are more robustly constrained, and c) taking into account the large astrophysical uncertainties on the magnetic fields. We have shown that synchrotron emissions can give very pertinent bounds on DM annihilation cross section, confirming previous results [14, 16–18].

The discussion of the astrophysical propagation setup occupies a large fraction of this work. Together with a usual set of CR propagation parameters used previously to gauge uncertainties of the astrophysical conditions on the radio signals, (MIN, MED and MAX models of propagation [23]), we have considered several other sets of CR parameters, which are shown to be consistent with CR, gamma ray and/or synchrotron data [24–26]. We have also explored the impact of the magnitude of the magnetic field in our ROI and found that it is generally mild, ranging a factor of 3–4 for magnetic fields in the inner Galaxy in the range between 1–100 μG.

One of the purpose of our work is to put in perspective various indirect bounds on dark matter models, complemented with collider constraints. Although the scope of our results is broader, this was in part motivated by the fact that both colliders and indirect searches are supposed to put very relevant limits on relatively light dark matter candidates, $m_{DM} \lesssim 10\,\text{GeV}$, for which direct detection limits are weaker, or altogether inexistent. In this spirit, we have briefly reviewed (and applied to particle physics models in question, including forecasts) the constraints from *Fermi* LAT observations of nearby dwarf spheroidal galaxies [19], as well as the limits set by CMB anisotropies [20]. Both of these observations give stringent indirect limits on dark matter annihilation cross sections and treat targets different than the one we focus on to derive the radio DM constraints, providing therefore independent probes of DM self-annihilation signatures.

JCAP11(2012)038

We have applied our results to various DM particle models, starting with a generic approach based on effective operators. There, we have shown that, for reasonable values of parameters, and for a conservatively chosen ROI, synchrotron searches for DM could be comparable to those of colliders, and sometimes even do better. In particular, in the case of effective couplings to leptons, we have shown that, even for very conservative setups, where we supposed that all the radio data are saturated by the synchrotron radiation produced by DM annihilation, the limits obtained are already competitive with those based on LEP measurements (photon+missing energy). In this case too, radio constraints can even be better than the ones derived from CMB, depending on the uncertainty on the astrophysical modelling. Concretely, allowing that DM contribute to 5% the background signal could give the best limit obtained by current indirect detection signals. For effective couplings to quarks, the synchrotron have a strong potential too, but due to huge uncertainties in the prediction of this signal, one cannot robustly claim that the most conservative synchrotron constraints can improve over the collider bounds. As expected, if DM couples to hadrons, dwarf constraint generally perform better.

The effective approach is powerful, but reaches its limits when resonance effects become relevant. To assess such effects, and for the own sake of a more microscopic approach to DM phenomenology, we have considered the constraints set by radio synchrotron radiation on two specific DM models: the so-called Higgs and Z' portals. This is motivated by the fact that these models are among the simplest extensions of the SM with DM candidates. Moreover, each of these models provide fully self-consistent UV completions of the effective operator approach, and thus provide complementary, albeit model dependent, information. We have shown that radio data may put severe constraints on these models, but at some price. Provided the uncertainty on the background could be assessed at the 5% level, and assuming a cuspy profile (NFW), and a large magnetic field, most of the Higgs portal parameter space is excluded, except near resonance (the Higgs pole), or close the threshold for W^+W^- annihilation, which is impeded in the Galaxy (by construction both these effects are inexistent in an effective operator approach). We have also shown a very good complementarity between synchrotron bounds and the last XENON100 bounds when considering the exclusion of the parameter space of the model. For the case of the Z' portal, because of substantial annihilation into leptons, the constraints are stronger, or alternatively, the astrophysical setup may be more conservative (smaller magnetic field, less cuspy profile), but some control of the background is also required to exclude (most of) the parameter space.

This work illustrates again, if necessary, that a multi-signal approach provides very complementary information on DM phenomenology. If on the long run, DM production at colliders is likely to give the strongest constraints, one should keep in mind that missing energy may not be directly related to the actual DM that is supposedly present in our Galaxy. Our results present (part of) the state of art in confronting indirect searches, with a particular emphasis on synchrotron radio data, a very promising signal for dark matter, provided some control may be gained on the mundane, astrophysical background, a fascinating challenge for both future observations and theoretical works. To pave the road, in the near future, PLANCK will be able to study Galactic emission in the frequency range where it is dominated by the dust emission, mapping with unprecedented precision dust (and therefore indirectly gas) content of our Galaxy. Together with improvements in measurement of the charge cosmic ray spectra we will soon be getting from AMS–02[21] and measurement of diffuse emission in

[21] http://ams.cern.ch/.

JCAP11(2012)038

gamma rays of such CR population, with the *Fermi* LAT, models of propagation and energy losses of CR are expected to advance significantly over the next 5-10 year period. Finally, the future radio telescope facilities, like the LOFAR and SKA, will provide further leverage on the possible radio synchrotron signal from DM particles, in particular for lighter candidates.

Acknowledgments

The authors want to thank Illias Cholis, Alessandro Cuoco, Timur Delahaye, and Roberto Lineros for very useful discussions and opinions. Y.M. was supported by the French ANR TAPDMS ANR-09-JCJC-0146 and the Spanish MICINN's Consolider-Ingenio 2010 Programme under grant Multi- Dark CSD2009-00064. B.Z. acknowledges the financial support of the FPI (MICINN) grant BES-2008-004688, and the contracts FPA2010-17747 and PITN-GA-2009-237920 (UNILHC) of the European Commission, as well as LPT-Orsay of Université Paris Sud, for the hospitality during the development of this project. The work of M.T. is supported by the IISN and an ULB-ARC grant. He also thanks the LPT-Orsay group for support and hospitality. G.Z. is grateful to the Institut d'Astrophysique de Paris for hospitality during completion of this work.

JCAP11(2012)038

A Annihilation cross-sections $\langle \sigma v \rangle$, for different effective operators

The expressions for the annihilation cross-sections coming from the operators $\mathcal{O}_S, \mathcal{O}_V$ and $\mathcal{O}_A$ are given by:

$$\sigma_S v = \frac{1}{8\pi\Lambda^4}\sqrt{1-\frac{m_f^2}{m_\chi^2}}(m_\chi^2 - m_f^2)v^2\,, \tag{A.1}$$

$$\sigma_V v = \frac{1}{48\pi\Lambda^4}\sqrt{1-\frac{m_f^2}{m_\chi^2}} \times\left(24(2m_\chi^2+m_f^2)+\frac{8m_\chi^4-4m_\chi^2m_f^2+5m_f^4}{m_\chi^2-m_f^2}v^2\right)\,, \tag{A.2}$$

$$\sigma_A v = \frac{1}{48\pi\Lambda^4}\sqrt{1-\frac{m_f^2}{m_\chi^2}} \times\left(24m_f^2+\frac{8m_\chi^4-22m_\chi^2m_f^2+17m_f^4}{m_\chi^2-m_f^2}v^2\right)\,; \tag{A.3}$$

where m_f is the fermion mass and m_χ the DM mass, while v is the relative velocity of incoming particles, which at the moment of freeze-out it is assumed to be $v^2 = 0.24$ [8].

References

[1] L. Bergstrom, *Nonbaryonic dark matter: Observational evidence and detection methods*, *Rept. Prog. Phys.* **63** (2000) 793 [hep-ph/0002126] [INSPIRE].

[2] G. Bertone, D. Hooper and J. Silk, *Particle dark matter: Evidence, candidates and constraints*, *Phys. Rept.* **405** (2005) 279 [hep-ph/0404175] [INSPIRE].

[3] G. Bertone (ed.), *Particle dark matter: Observations, models and searches*, Cambridge University Press, Cambridge U.K. (2010).

[4] CDMS-II collaboration, Z. Ahmed et al., *Results from a Low-Energy Analysis of the CDMS II Germanium Data*, *Phys. Rev. Lett.* **106** (2011) 131302 [arXiv:1011.2482] [INSPIRE].

[5] XENON100 collaboration, E. Aprile et al., *Dark Matter Results from 100 Live Days of XENON100 Data*, *Phys. Rev. Lett.* **107** (2011) 131302 [arXiv:1104.2549] [INSPIRE].

[6] J. Goodman et al., *Constraints on Dark Matter from Colliders*, *Phys. Rev.* **D 82** (2010) 116010 [arXiv:1008.1783] [INSPIRE].

[7] Y. Bai, P.J. Fox and R. Harnik, *The Tevatron at the Frontier of Dark Matter Direct Detection*, *JHEP* **12** (2010) 048 [arXiv:1005.3797] [INSPIRE].

[8] P.J. Fox, R. Harnik, J. Kopp and Y. Tsai, *LEP Shines Light on Dark Matter*, *Phys. Rev.* **D 84** (2011) 014028 [arXiv:1103.0240] [INSPIRE].

[9] P.J. Fox, R. Harnik, J. Kopp and Y. Tsai, *Missing Energy Signatures of Dark Matter at the LHC*, *Phys. Rev.* **D 85** (2012) 056011 [arXiv:1109.4398] [INSPIRE].

[10] CMS collaboration, S. Chatrchyan et al., *Search for Dark Matter and Large Extra Dimensions in pp Collisions Yielding a Photon and Missing Transverse Energy*, *Phys. Rev. Lett.* **108** (2012) 261803 [arXiv:1204.0821] [INSPIRE].

[11] Y. Mambrini and B. Zaldivar, *When LEP and Tevatron combined with WMAP and XENON100 shed light on the nature of Dark Matter*, *JCAP* **10** (2011) 023 [arXiv:1106.4819] [INSPIRE].

[12] G. Bertone, G. Sigl and J. Silk, *Astrophysical limits on massive dark matter*, *Mon. Not. Roy. Astron. Soc.* **326** (2001) 799 [astro-ph/0101134] [INSPIRE].

[13] R. Aloisio, P. Blasi and A.V. Olinto, *Neutralino annihilation at the Galactic Center revisited*, *JCAP* **05** (2004) 007 [astro-ph/0402588] [INSPIRE].

[14] L. Bergstrom, G. Bertone, T. Bringmann, J. Edsjo and M. Taoso, *Gamma-ray and Radio Constraints of High Positron Rate Dark Matter Models Annihilating into New Light Particles*, *Phys. Rev.* **D 79** (2009) 081303 [arXiv:0812.3895] [INSPIRE].

[15] T. Bringmann, *Antiproton and Radio Constraints on the Dark Matter Interpretation of the Fermi Gamma Ray Observations of the Galactic Center*, arXiv:0911.1124 [INSPIRE].

[16] E. Borriello, A. Cuoco and G. Miele, *Radio constraints on dark matter annihilation in the galactic halo and its substructures*, *Phys. Rev.* **D 79** (2009) 023518 [arXiv:0809.2990] [INSPIRE].

[17] C. Boehm, J. Silk and T. Ensslin, *Radio observations of the Galactic Centre and the Coma cluster as a probe of light dark matter self-annihilations and decay*, arXiv:1008.5175 [INSPIRE].

[18] N. Fornengo, R.A. Lineros, M. Regis and M. Taoso, *Galactic synchrotron emission from WIMPs at radio frequencies*, *JCAP* **01** (2012) 005 [arXiv:1110.4337] [INSPIRE].

[19] FERMI-LAT collaboration, M. Ackermann et al., *Constraining Dark Matter Models from a Combined Analysis of Milky Way Satellites with the Fermi Large Area Telescope*, *Phys. Rev. Lett.* **107** (2011) 241302 [arXiv:1108.3546] [INSPIRE].

[20] S. Galli, F. Iocco, G. Bertone and A. Melchiorri, *Updated CMB constraints on Dark Matter annihilation cross-sections*, *Phys. Rev.* **D 84** (2011) 027302 [arXiv:1106.1528] [INSPIRE].

[21] T.A. Porter, I.V. Moskalenko, A.W. Strong, E. Orlando and L. Bouchet, *Inverse Compton Origin of the Hard X-Ray and Soft Gamma-Ray Emission from the Galactic Ridge*, *Astrophys. J.* **682** (2008) 400 [arXiv:0804.1774] [INSPIRE].

JCAP11(2012)038

[22] A.E. Vladimirov et al., *GALPROP WebRun: an internet-based service for calculating galactic cosmic ray propagation and associated photon emissions*, *Comput. Phys. Commun.* **182** (2011) 1156 [arXiv:1008.3642] [INSPIRE].

[23] F. Donato, N. Fornengo, D. Maurin and P. Salati, *Antiprotons in cosmic rays from neutralino annihilation*, *Phys. Rev.* **D 69** (2004) 063501 [astro-ph/0306207] [INSPIRE].

[24] FERMI-LAT collaboration, *Fermi-LAT Observations of the Diffuse Gamma-Ray Emission: Implications for Cosmic Rays and the Interstellar Medium*, *Astrophys. J.* **750** (2012) 3 [arXiv:1202.4039] [INSPIRE].

[25] R. Trotta et al., *Constraints on cosmic-ray propagation models from a global Bayesian analysis*, *Astrophys. J.* **729** (2011) 106 [arXiv:1011.0037] [INSPIRE].

[26] A. Strong, E. Orlando and T. Jaffe, *The interstellar cosmic-ray electron spectrum from synchrotron radiation and direct measurements*, *Astron. Astrophys.* **534** (2011) A54 [arXiv:1108.4822] [INSPIRE].

[27] A.E. Guzman, J. May, H. Alvarez and K. Maeda, *All-sky Galactic radiation at 45 MHz and spectral index between 45 and 408 MHz*, *Astron. Astrophys.* **525** (2011) A138 [arXiv:1011.4298] [INSPIRE].

[28] A. de Oliveira-Costa et al., *A model of diffuse Galactic Radio Emission from 10 MHz to 100 GHz*, arXiv:0802.1525 [INSPIRE].

[29] C.G.T. Haslam, C.J. Salter, H. Stoffel and W.E. Wilson, *A 408 MHz all-sky continuum survey. II. The atlas of contour maps*, *Astron. Astrophys. Suppl. Ser.* **47** (1982) 1.

[30] M.E. Nord et al., *High-resolution, wide-field imaging of the Galactic Center region at 330 MHz*, *Astron. J.* (2004) [astro-ph/0407178] [INSPIRE].

[31] P. Gondolo and J. Silk, *Dark matter annihilation at the galactic center*, *Phys. Rev. Lett.* **83** (1999) 1719 [astro-ph/9906391] [INSPIRE].

[32] D. Merritt, *Evolution of the dark matter distribution at the galactic center*, *Phys. Rev. Lett.* **92** (2004) 201304 [astro-ph/0311594] [INSPIRE].

[33] V.L. Ginzburg et al. (ed.), *Astrophysics of cosmic rays*, North-Holland, Amsterdam Netherlands (1990).

[34] E.A. Baltz and J. Edsjo, *Positron propagation and fluxes from neutralino annihilation in the halo*, *Phys. Rev.* **D 59** (1998) 023511 [astro-ph/9808243] [INSPIRE].

[35] T. Delahaye, R. Lineros, F. Donato, N. Fornengo and P. Salati, *Positrons from dark matter annihilation in the galactic halo: Theoretical uncertainties*, *Phys. Rev.* **D 77** (2008) 063527 [arXiv:0712.2312] [INSPIRE].

[36] G. Rybicki and A. Lightman, *Radiative processes in astrophysics*, Wiley-VCH (2004).

[37] G. Bertone, M. Cirelli, A. Strumia and M. Taoso, *Gamma-ray and radio tests of the e^+e^- excess from DM annihilations*, *JCAP* **03** (2009) 009 [arXiv:0811.3744] [INSPIRE].

[38] M. Regis and P. Ullio, *Multi-wavelength signals of dark matter annihilations at the Galactic center*, *Phys. Rev.* **D 78** (2008) 043505 [arXiv:0802.0234] [INSPIRE].

[39] J.F. Navarro, C.S. Frenk and S.D. White, *The Structure of cold dark matter halos*, *Astrophys. J.* **462** (1996) 563 [astro-ph/9508025] [INSPIRE].

[40] A.W. Graham, D. Merritt, B. Moore, J. Diemand and B. Terzic, *Empirical models for Dark Matter Halos. I. Nonparametric Construction of Density Profiles and Comparison with Parametric Models*, *Astron. J.* **132** (2006) 2685 [astro-ph/0509417] [INSPIRE].

[41] J.F. Navarro et al., *The Diversity and Similarity of Cold Dark Matter Halos*, arXiv:0810.1522 [INSPIRE].

JCAP11(2012)038

[42] A.V. Maccio' et al., *Halo expansion in cosmological hydro simulations: towards a baryonic solution of the cusp/core problem in massive spirals*, arXiv:1111.5620 [INSPIRE].

[43] K. Begeman, A. Broeils and R. Sanders, *Extended rotation curves of spiral galaxies: Dark haloes and modified dynamics*, *Mon. Not. Roy. Astron. Soc.* **249** (1991) 523 [INSPIRE].

[44] J.N. Bahcall and R. Soneira, *The Universe at faint magnetidues. 2. Models for the predicted star counts*, *Astrophys. J. Suppl.* **44** (1980) 73 [INSPIRE].

[45] M. Cirelli, G. Corcella, A. Hektor, G. Hutsi, M. Kadastik, et al., *PPPC 4 DM ID: A Poor Particle Physicist Cookbook for Dark Matter Indirect Detection*, *JCAP* () 032011051 [*Erratum ibid.* **1210** (2012) E01] [arXiv:1012.4515] [INSPIRE].

[46] D. Maurin, F. Donato, R. Taillet and P. Salati, *Cosmic rays below $z = 30$ in a diffusion model: new constraints on propagation parameters*, *Astrophys. J.* **555** (2001) 585 [astro-ph/0101231] [INSPIRE].

[47] D. Maurin, R. Taillet and F. Donato, *New results on source and diffusion spectral features of galactic cosmic rays: I- B/C ratio*, *Astron. Astrophys.* **394** (2002) 1039 [astro-ph/0206286] [INSPIRE].

[48] R. Jansson and G.R. Farrar, *A New Model of the Galactic Magnetic Field*, *Astrophys. J.* **757** (2012) 14 [arXiv:1204.3662] [INSPIRE].

[49] M. Pshirkov, P. Tinyakov, P. Kronberg and K. Newton-McGee, *Deriving global structure of the Galactic Magnetic Field from Faraday Rotation Measures of extragalactic sources*, *Astrophys. J.* **738** (2011) 192 [arXiv:1103.0814] [INSPIRE].

[50] J. Brown et al., *Rotation Measures of Extragalactic Sources Behind the Southern Galactic Plane: New Insights into the Large-Scale Magnetic Field of the Inner Milky Way*, *Astrophys. J.* **663** (2007) 258 [arXiv:0704.0458] [INSPIRE].

[51] J. Han, R. Manchester, A. Lyne, G. Qiao and W. van Straten, *Pulsar rotation measures and the large-scale structure of Galactic magnetic field*, *Astrophys. J.* **642** (2006) 868 [astro-ph/0601357] [INSPIRE].

[52] X. Sun and W. Reich, *The Galactic halo magnetic field revisited*, *Res. Astron. Astrophys.* **10** (2010) 1287 [arXiv:1010.4394] [INSPIRE].

[53] X. Sun, W. Reich, A. Waelkens and T. Enslin, *Radio observational constraints on Galactic 3D-emission models*, arXiv:0711.1572 [INSPIRE].

[54] A.W. Strong, I.V. Moskalenko and O. Reimer, *Diffuse galactic continuum gamma rays. A Model compatible with EGRET data and cosmic-ray measurements*, *Astrophys. J.* **613** (2004) 962 [astro-ph/0406254] [INSPIRE].

[55] G. Dobler, I. Cholis and N. Weiner, *The Fermi Gamma-Ray Haze from Dark Matter Annihilations and Anisotropic Diffusion*, *Astrophys. J.* **741** (2011) 25 [arXiv:1102.5095] [INSPIRE].

[56] M. Su, T.R. Slatyer and D.P. Finkbeiner, *Giant Gamma-ray Bubbles from Fermi-LAT: AGN Activity or Bipolar Galactic Wind?*, *Astrophys. J.* **724** (2010) 1044 [arXiv:1005.5480] [INSPIRE].

[57] M. Su and D.P. Finkbeiner, *Evidence for Gamma-ray Jets in the Milky Way*, *Astrophys. J.* **753** (2012) 61 [arXiv:1205.5852] [INSPIRE].

[58] D.P. Finkbeiner, *Microwave ism emission observed by wmap*, *Astrophys. J.* **614** (2004) 186 [astro-ph/0311547] [INSPIRE].

[59] http://www.esa.int/SPECIALS/Planck/SEM0FLYXHYG_0.html.

[60] P. Salucci, F. Nesti, G. Gentile and C. Martins, *The dark matter density at the Sun's location*, *Astron. Astrophys.* **523** (2010) A83 [arXiv:1003.3101] [INSPIRE].

JCAP11(2012)038

[61] T. Bringmann, F. Donato and R.A. Lineros, *Radio data and synchrotron emission in consistent cosmic ray models*, *JCAP* **01** (2012) 049 [arXiv:1106.4821] [INSPIRE].

[62] R. Cotta et al., *Constraints on the pMSSM from LAT Observations of Dwarf Spheroidal Galaxies*, *JCAP* **04** (2012) 016 [arXiv:1111.2604] [INSPIRE].

[63] N. Padmanabhan and D.P. Finkbeiner, *Detecting dark matter annihilation with CMB polarization: Signatures and experimental prospects*, *Phys. Rev.* **D 72** (2005) 023508 [astro-ph/0503486] [INSPIRE].

[64] T.R. Slatyer, N. Padmanabhan and D.P. Finkbeiner, *CMB Constraints on WIMP Annihilation: Energy Absorption During the Recombination Epoch*, *Phys. Rev.* **D 80** (2009) 043526 [arXiv:0906.1197] [INSPIRE].

[65] S. Galli, F. Iocco, G. Bertone and A. Melchiorri, *CMB constraints on Dark Matter models with large annihilation cross-section*, *Phys. Rev.* **D 80** (2009) 023505 [arXiv:0905.0003] [INSPIRE].

[66] G. Hutsi, J. Chluba, A. Hektor and M. Raidal, *WMAP7 and future CMB constraints on annihilating dark matter: implications on GeV-scale WIMPs*, *Astron. Astrophys.* **535** (2011) A26 [arXiv:1103.2766] [INSPIRE].

[67] WMAP collaboration, E. Komatsu et al., *Seven-Year Wilkinson Microwave Anisotropy Probe (WMAP) Observations: Cosmological Interpretation*, *Astrophys. J. Suppl.* **192** (2011) 18 [arXiv:1001.4538] [INSPIRE].

[68] ACT collaboration, J. Fowler et al., *The Atacama Cosmology Telescope: A Measurement of the* $600 < \ell < 8000$ *Cosmic Microwave Background Power Spectrum at 148 GHz*, *Astrophys. J.* **722** (2010) 1148 [arXiv:1001.2934] [INSPIRE].

[69] DELPHI collaboration, J. Abdallah et al., *Photon events with missing energy in* e^+e^- *collisions at* $\sqrt{s} = 130\,GeV$ *to* $209\,GeV$, *Eur. Phys. J.* **C 38** (2005) 395 [hep-ex/0406019] [INSPIRE].

[70] DELPHI collaboration, J. Abdallah et al., *Search for one large extra dimension with the DELPHI detector at LEP*, *Eur. Phys. J.* **C 60** (2009) 17 [arXiv:0901.4486] [INSPIRE].

[71] M. Beltrán, D. Hooper, E.W. Kolb, Z.A. Krusberg and T.M. Tait, *Maverick dark matter at colliders*, *JHEP* **09** (2010) 037 [arXiv:1002.4137] [INSPIRE].

[72] http://www-cdf.fnal.gov/physics/exotic/r2a/20070322/monojet/public/ykk.html.

[73] ATLAS collaboration, G. Aad et al., *Search for new phenomena with the monojet and missing transverse momentum signature using the ATLAS detector in* $\sqrt{s} = 7\ TeV$ *proton-proton collisions*, *Phys. Lett.* **B 705** (2011) 294 [arXiv:1106.5327] [INSPIRE].

[74] M.T. Frandsen, F. Kahlhoefer, A. Preston, S. Sarkar and K. Schmidt-Hoberg, *LHC and Tevatron Bounds on the Dark Matter Direct Detection Cross-Section for Vector Mediators*, *JHEP* **07** (2012) 123 [arXiv:1204.3839] [INSPIRE];
G. Bélanger, M. Heikinheimo and V. Sanz, *Model-Independent Bounds on Squarks from Monophoton Searches*, *JHEP* **08** (2012) 151 [arXiv:1205.1463] [INSPIRE].

[75] J. McDonald, *Gauge singlet scalars as cold dark matter*, *Phys. Rev.* **D 50** (1994) 3637 [hep-ph/0702143] [INSPIRE];
C. Burgess, M. Pospelov and T. ter Veldhuis, *The Minimal model of nonbaryonic dark matter: A Singlet scalar*, *Nucl. Phys.* **B 619** (2001) 709 [hep-ph/0011335] [INSPIRE];
H. Davoudiasl, R. Kitano, T. Li and H. Murayama, *The New minimal standard model*, *Phys. Lett.* **B 609** (2005) 117 [hep-ph/0405097] [INSPIRE];
B. Patt and F. Wilczek, *Higgs-field portal into hidden sectors*, hep-ph/0605188 [INSPIRE];
X.-G. He, T. Li, X.-Q. Li, J. Tandean and H.-C. Tsai, *Constraints on Scalar Dark Matter from Direct Experimental Searches*, *Phys. Rev.* **D 79** (2009) 023521 [arXiv:0811.0658] [INSPIRE];

JCAP11(2012)038

X.-G. He, T. Li, X.-Q. Li, J. Tandean and H.-C. Tsai, *The Simplest Dark-Matter Model, CDMS II Results and Higgs Detection at LHC*, *Phys. Lett.* **B 688** (2010) 332 [arXiv:0912.4722] [INSPIRE];
V. Barger, Y. Gao, M. McCaskey and G. Shaughnessy, *Light Higgs Boson, Light Dark Matter and Gamma Rays*, *Phys. Rev.* **D 82** (2010) 095011 [arXiv:1008.1796] [INSPIRE];
V. Barger, P. Langacker, M. McCaskey, M.J. Ramsey-Musolf and G. Shaughnessy, *LHC Phenomenology of an Extended Standard Model with a Real Scalar Singlet*, *Phys. Rev.* **D 77** (2008) 035005 [arXiv:0706.4311] [INSPIRE];
T. Clark, B. Liu, S. Love and T. ter Veldhuis, *The Standard Model Higgs Boson-Inflaton and Dark Matter*, *Phys. Rev.* **D 80** (2009) 075019 [arXiv:0906.5595] [INSPIRE];
R.N. Lerner and J. McDonald, *Gauge singlet scalar as inflaton and thermal relic dark matter*, *Phys. Rev.* **D 80** (2009) 123507 [arXiv:0909.0520] [INSPIRE];
O. Lebedev and H.M. Lee, *Higgs Portal Inflation*, *Eur. Phys. J.* **C 71** (2011) 1821 [arXiv:1105.2284] [INSPIRE];
A. Biswas and D. Majumdar, *The Real Gauge Singlet Scalar Extension of Standard Model: A Possible Candidate of Cold Dark Matter*, arXiv:1102.3024 [INSPIRE];
O. Lebedev, *On Stability of the Electroweak Vacuum and the Higgs Portal*, *Eur. Phys. J.* **C 72** (2012) 2058 [arXiv:1203.0156] [INSPIRE];
S. Kanemura, S. Matsumoto, T. Nabeshima and N. Okada, *Can WIMP Dark Matter overcome the Nightmare Scenario?*, *Phys. Rev.* **D 82** (2010) 055026 [arXiv:1005.5651] [INSPIRE];
C. Arina, F.-X. Josse-Michaux and N. Sahu, *A Tight Connection Between Direct and Indirect Detection of Dark Matter through Higgs Portal Couplings to a Hidden Sector*, *Phys. Rev.* **D 82** (2010) 015005 [arXiv:1004.3953] [INSPIRE].

[76] V. Barger, P. Langacker, M. McCaskey, M.J. Ramsey-Musolf and G. Shaughnessy, *LHC Phenomenology of an Extended Standard Model with a Real Scalar Singlet*, *Phys. Rev.* **D 77** (2008) 035005 [arXiv:0706.4311] [INSPIRE].

[77] S. Andreas, C. Arina, T. Hambye, F.-S. Ling and M.H. Tytgat, *A light scalar WIMP through the Higgs portal and CoGeNT*, *Phys. Rev.* **D 82** (2010) 043522 [arXiv:1003.2595] [INSPIRE];
M. Farina et al., *Implications of XENON100 and LHC results for Dark Matter models*, *Nucl. Phys.* **B 853** (2011) 607 [arXiv:1104.3572] [INSPIRE].

[78] Y. Mambrini, *Higgs searches and singlet scalar dark matter: Combined constraints from XENON 100 and the LHC*, *Phys. Rev.* **D 84** (2011) 115017 [arXiv:1108.0671] [INSPIRE];
M. Raidal and A. Strumia, *Hints for a non-standard Higgs boson from the LHC*, *Phys. Rev.* **D 84** (2011) 077701 [arXiv:1108.4903] [INSPIRE];
X.-G. He and J. Tandean, *Hidden Higgs Boson at the LHC and Light Dark Matter Searches*, *Phys. Rev.* **D 84** (2011) 075018 [arXiv:1109.1277] [INSPIRE];
Y. Mambrini, *Invisible Higgs and Scalar Dark Matter*, arXiv:1112.0011 [INSPIRE];
X.-G. He, B. Ren and J. Tandean, *Hints of Standard Model Higgs Boson at the LHC and Light Dark Matter Searches*, *Phys. Rev.* **D 85** (2012) 093019 [arXiv:1112.6364] [INSPIRE];
J.F. Kamenik and C. Smith, *Could a light Higgs boson illuminate the dark sector?*, *Phys. Rev.* **D 85** (2012) 093017 [arXiv:1201.4814] [INSPIRE];
M. Pospelov and A. Ritz, *Higgs decays to dark matter: beyond the minimal model*, *Phys. Rev.* **D 84** (2011) 113001 [arXiv:1109.4872] [INSPIRE];
I. Low, P. Schwaller, G. Shaughnessy and C.E. Wagner, *The dark side of the Higgs boson*, *Phys. Rev.* **D 85** (2012) 015009 [arXiv:1110.4405] [INSPIRE];
E. Weihs and J. Zurita, *Dark Higgs Models at the 7 TeV LHC*, *JHEP* **02** (2012) 041 [arXiv:1110.5909] [INSPIRE];
C. Englert, J. Jaeckel, E. Re and M. Spannowsky, *Evasive Higgs Maneuvers at the LHC*, *Phys. Rev.* **D 85** (2012) 035008 [arXiv:1111.1719] [INSPIRE];
X. Chu, T. Hambye and M.H. Tytgat, *The Four Basic Ways of Creating Dark Matter Through a Portal*, *JCAP* **05** (2012) 034 [arXiv:1112.0493] [INSPIRE];
P.P. Giardino, K. Kannike, M. Raidal and A. Strumia, *Reconstructing Higgs boson properties*

from the LHC and Tevatron data, *JHEP* **06** (2012) 117 [arXiv:1203.4254] [INSPIRE];
A. Arhrib, R. Benbrik and N. Gaur, $H \to \gamma\gamma$ *in Inert Higgs Doublet Model*, *Phys. Rev.* **D 85** (2012) 095021 [arXiv:1201.2644] [INSPIRE];
Y. Cai, X.-G. He and B. Ren, *Low Mass Dark Matter and Invisible Higgs Width In Darkon Models*, *Phys. Rev.* **D 83** (2011) 083524 [arXiv:1102.1522] [INSPIRE];
M. Frigerio, A. Pomarol, F. Riva and A. Urbano, *Composite Scalar Dark Matter*, *JHEP* **07** (2012) 015 [arXiv:1204.2808] [INSPIRE].

[79] A. Djouadi, O. Lebedev, Y. Mambrini and J. Quevillon, *Implications of LHC searches for Higgs–portal dark matter*, *Phys. Lett.* **B 709** (2012) 65 [arXiv:1112.3299] [INSPIRE];
L. Lopez-Honorez, T. Schwetz and J. Zupan, *Higgs portal, fermionic dark matter and a Standard Model like Higgs at 125 GeV*, *Phys. Lett.* **B 716** (2012) 179 [arXiv:1203.2064] [INSPIRE].

[80] C.E. Yaguna, *Gamma rays from the annihilation of singlet scalar dark matter*, *JCAP* **03** (2009) 003 [arXiv:0810.4267] [INSPIRE].

[81] A. Goudelis, Y. Mambrini and C. Yaguna, *Antimatter signals of singlet scalar dark matter*, *JCAP* **12** (2009) 008 [arXiv:0909.2799] [INSPIRE].

[82] S. Andreas, C. Arina, T. Hambye, F.-S. Ling and M.H. Tytgat, *A light scalar WIMP through the Higgs portal and CoGeNT*, *Phys. Rev.* **D 82** (2010) 043522 [arXiv:1003.2595] [INSPIRE];
C. Arina and M.H. Tytgat, *Constraints on Light WIMP candidates from the Isotropic Diffuse Gamma-Ray Emission*, *JCAP* **01** (2011) 011 [arXiv:1007.2765] [INSPIRE].

[83] M. Farina et al., *Implications of XENON100 and LHC results for Dark Matter models*, *Nucl. Phys.* **B 853** (2011) 607 [arXiv:1104.3572] [INSPIRE];
Y. Mambrini, *Higgs searches and singlet scalar dark matter: Combined constraints from XENON 100 and the LHC*, *Phys. Rev.* **D 84** (2011) 115017 [arXiv:1108.0671] [INSPIRE].

[84] P.P. Giardino, K. Kannike, M. Raidal and A. Strumia, *Reconstructing Higgs boson properties from the LHC and Tevatron data*, *JHEP* **06** (2012) 117 [arXiv:1203.4254] [INSPIRE].

[85] T. Hambye, *Hidden vector dark matter*, *JHEP* **01** (2009) 028 [arXiv:0811.0172] [INSPIRE];
T. Hambye and M.H. Tytgat, *Confined hidden vector dark matter*, *Phys. Lett.* **B 683** (2010) 39 [arXiv:0907.1007] [INSPIRE];
J. Hisano, K. Ishiwata, N. Nagata and M. Yamanaka, *Direct Detection of Vector Dark Matter*, *Prog. Theor. Phys.* **126** (2011) 435 [arXiv:1012.5455] [INSPIRE];
O. Lebedev, H.M. Lee and Y. Mambrini, *Vector Higgs-portal dark matter and the invisible Higgs*, *Phys. Lett.* **B 707** (2012) 570 [arXiv:1111.4482] [INSPIRE];
T. Abe, M. Kakizaki, S. Matsumoto and O. Seto, *Vector WIMP Miracle*, *Phys. Lett.* **B 713** (2012) 211 [arXiv:1202.5902] [INSPIRE].

[86] P. Langacker, *The Physics of Heavy Z' Gauge Bosons*, *Rev. Mod. Phys.* **81** (2009) 1199 [arXiv:0801.1345] [INSPIRE].

[87] R. Foot and X.-G. He, *Comment on Z Z-prime mixing in extended gauge theories*, *Phys. Lett.* **B 267** (1991) 509 [INSPIRE];
R. Foot, H. Lew and R. Volkas, *A Model with fundamental improper space-time symmetries*, *Phys. Lett.* **B 272** (1991) 67 [INSPIRE];
B. Holdom, *Two U(1)'s and Epsilon Charge Shifts*, *Phys. Lett.* **B 166** (1986) 196 [INSPIRE];
D. Feldman, Z. Liu and P. Nath, *The Stueckelberg Z-prime Extension with Kinetic Mixing and Milli-Charged Dark Matter From the Hidden Sector*, *Phys. Rev.* **D 75** (2007) 115001 [hep-ph/0702123] [INSPIRE];
S.P. Martin, *Implications of supersymmetric models with natural R-parity conservation*, *Phys. Rev.* **D 54** (1996) 2340 [hep-ph/9602349] [INSPIRE];
T.G. Rizzo, *Gauge kinetic mixing and leptophobic Z' in E_6 and* SO(10), *Phys. Rev.* **D 59** (1998) 015020 [hep-ph/9806397] [INSPIRE];

JCAP11(2012)038

F. del Aguila, M. Masip and M. Pérez-Victoria, *Physical parameters and renormalization of U(1)-a x U(1)-b models*, *Nucl. Phys.* **B 456** (1995) 531 [hep-ph/9507455] [INSPIRE];
B.A. Dobrescu, *Massless gauge bosons other than the photon*, *Phys. Rev. Lett.* **94** (2005) 151802 [hep-ph/0411004] [INSPIRE];
K.R. Dienes, C.F. Kolda and J. March-Russell, *Kinetic mixing and the supersymmetric gauge hierarchy*, *Nucl. Phys.* **B 492** (1997) 104 [hep-ph/9610479] [INSPIRE];
T. Cohen, D.J. Phalen, A. Pierce and K.M. Zurek, *Asymmetric Dark Matter from a GeV Hidden Sector*, *Phys. Rev.* **D 82** (2010) 056001 [arXiv:1005.1655] [INSPIRE];
Z. Kang, T. Li, T. Liu, C. Tong and J.M. Yang, *Light Dark Matter from the $U(1)_X$ Sector in the NMSSM with Gauge Mediation*, *JCAP* **01** (2011) 028 [arXiv:1008.5243] [INSPIRE];
N. Fornengo, P. Panci and M. Regis, *Long-Range Forces in Direct Dark Matter Searches*, *Phys. Rev.* **D 84** (2011) 115002 [arXiv:1108.4661] [INSPIRE].

[88] D. Feldman, B. Körs and P. Nath, *Extra-weakly Interacting Dark Matter*, *Phys. Rev.* **D 75** (2007) 023503 [hep-ph/0610133] [INSPIRE].

[89] D. Feldman, Z. Liu and P. Nath, *The Stueckelberg Z-prime Extension with Kinetic Mixing and Milli-Charged Dark Matter From the Hidden Sector*, *Phys. Rev.* **D 75** (2007) 115001 [hep-ph/0702123] [INSPIRE].

[90] M. Cicoli, M. Goodsell, J. Jaeckel and A. Ringwald, *Testing String Vacua in the Lab: From a Hidden CMB to Dark Forces in Flux Compactifications*, *JHEP* **07** (2011) 114 [arXiv:1103.3705] [INSPIRE].

[91] J. Kumar, A. Rajaraman and J.D. Wells, *Probing the Green-Schwarz Mechanism at the Large Hadron Collider*, *Phys. Rev.* **D 77** (2008) 066011 [arXiv:0707.3488] [INSPIRE].

[92] M. Goodsell, J. Jaeckel, J. Redondo and A. Ringwald, *Naturally Light Hidden Photons in LARGE Volume String Compactifications*, *JHEP* **11** (2009) 027 [arXiv:0909.0515] [INSPIRE];
S. Abel, M. Goodsell, J. Jaeckel, V. Khoze and A. Ringwald, *Kinetic Mixing of the Photon with Hidden U(1)s in String Phenomenology*, *JHEP* **07** (2008) 124 [arXiv:0803.1449] [INSPIRE].

[93] S. Cassel, D. Ghilencea and G. Ross, *Electroweak and Dark Matter Constraints on a Z-prime in Models with a Hidden Valley*, *Nucl. Phys.* **B 827** (2010) 256 [arXiv:0903.1118] [INSPIRE].

[94] M. Pospelov, *Secluded U(1) below the weak scale*, *Phys. Rev.* **D 80** (2009) 095002 [arXiv:0811.1030] [INSPIRE];
M. Pospelov, A. Ritz and M.B. Voloshin, *Secluded WIMP Dark Matter*, *Phys. Lett.* **B 662** (2008) 53 [arXiv:0711.4866] [INSPIRE];
W.-F. Chang, J.N. Ng and J.M. Wu, *A Very Narrow Shadow Extra Z-boson at Colliders*, *Phys. Rev.* **D 74** (2006) 095005 [*Erratum ibid.* **D 79** (2009) 039902] [hep-ph/0608068] [INSPIRE];
Z. Liu, *Hidden Sector Models and Signatures*, *Nucl. Phys. Proc. Suppl.* **200-202** (2010) 133 [arXiv:0910.0061] [INSPIRE];
R. Foot, *A comprehensive analysis of the dark matter direct detection experiments in the mirror dark matter framework*, *Phys. Rev.* **D 82** (2010) 095001 [arXiv:1008.0685] [INSPIRE].

[95] Y. Mambrini, *Specific Dark Matter signatures from hidden U(1)*, PoS(QFTHEP2010)027 [arXiv:1012.0447] [INSPIRE];
E.J. Chun, J.-C. Park and S. Scopel, *Dark matter and a new gauge boson through kinetic mixing*, *JHEP* **02** (2011) 100 [arXiv:1011.3300] [INSPIRE];
Y. Mambrini, *The ZZ' kinetic mixing in the light of the recent direct and indirect dark matter searches*, *JCAP* **07** (2011) 009 [arXiv:1104.4799] [INSPIRE]; *The Kinetic dark-mixing in the light of CoGENT and XENON100*, *JCAP* **09** (2010) 022 [arXiv:1006.3318] [INSPIRE].

[96] E. Dudas, Y. Mambrini, S. Pokorski and A. Romagnoni, *Extra U(1) as natural source of a monochromatic gamma ray line*, *JHEP* **10** (2012) 123 [arXiv:1205.1520] [INSPIRE];
Y. Mambrini, *A Clear Dark Matter gamma ray line generated by the Green-Schwarz mechanism*, *JCAP* **12** (2009) 005 [arXiv:0907.2918] [INSPIRE];

JCAP11(2012)038

E. Dudas, Y. Mambrini, S. Pokorski and A. Romagnoni, *(In)visible Z-prime and dark matter*, *JHEP* **08** (2009) 014 [arXiv:0904.1745] [INSPIRE];
C. Jackson, G. Servant, G. Shaughnessy, T.M. Tait and M. Taoso, *Higgs in Space!*, *JCAP* **04** (2010) 004 [arXiv:0912.0004] [INSPIRE].

[97] M. Baumgart, C. Cheung, J.T. Ruderman, L.-T. Wang and I. Yavin, *Non-Abelian Dark Sectors and Their Collider Signatures*, *JHEP* **04** (2009) 014 [arXiv:0901.0283] [INSPIRE].

[98] E.J. Chun, J.-C. Park and S. Scopel, *Dark matter and a new gauge boson through kinetic mixing*, *JHEP* **02** (2011) 100 [arXiv:1011.3300] [INSPIRE].

JCAP11(2012)038

CHAPTER 7

CONCLUSIONS

Next I mention briefly the main conclusions of the works presented in this thesis.

Regarding the Seesaw mechanism and Lepton Flavour Violation:

- The extended believe that in supersymmetric Seesaw models $BR(\mu \to e\gamma)$ depends strongly on the θ_{13} value, is not correct, as a careful analytical and numerical study shows. In this analysis we have scanned in a complete way the Seesaw parameter space using two alternative parametrisations, obtaining consistent results.

- The potential dependence of $BR(\mu \to e\gamma)$ en θ_{13} comes mainly from the $Y_\nu^\dagger Y_\nu$ matrix, where Y_ν is the neutrino Yukawa matrix. In one of the parametrisations we used (the so-called V_L-parametrisation) this magnitude is trivially insensitive to θ_{13} or any other observable parameter. This fact causes $BR(\mu \to e\gamma)$ to be also insensitive. In the other parametrisation (the so-called R-parametrisation), the quantity $Y_\nu^\dagger Y_\nu$ depends a priori on θ_{13}, but this dependence disappears when a complete scan of the parameter space is performed. Hence, the results of the two parametrisations are consistent, as expected.

- In this work we have obtained very simple rules to scan in a complete way the R-matrix of the second parametrisation, while respecting the perturbativity of the Yukawa couplings. These rules are valid for the supersymmetric as well as for the non-supersymmetric Seesaw.

- An important result is that the values of $BR(\mu \to e\gamma)$ in the supersymmetric Seesaw are typically larger than those reported in the literature (and above the experimental bounds). Essentially this is due to the fact that a complete scan of the R-matrix allows access to regions where the matrix entries are typically larger than those considered so far.

- When the condition of successful leptogenesis is imposed, the qualitative conclusions do not change; i.e. the requirement of leptogenesis does not introduce extra dependences of $BR(\mu \to e\gamma)$ on θ_{13}. However it does have an effect on the surviving values of BR, which tend to be lower.

Summarising, the conclusion of the first part of the thesis is that a complete scan of the parameter space of the $R-$matrix (for which we provide precise rules) is necessary, in order to arrive to general conclusions about predictions of the Seesaw scenario. This has not been taken into account in part of the works in previous literature, and thus we consider it an interesting line of research, which can be exploited in future projects

Regarding Dark Matter Phenomenology:

- We have computed the percentage of hadronic coupling (with respect to leptonic one) of Dark Matter with Standard Model particles, which is compatible with data coming from LEP, Tevatron, WMAP and XENON experiments. The bounds coming from LEP (Tevatron) are obtained from the study of final-state topologies consisting of a single photon (jet) plus missing energy.

- We have demonstrated that for thermally produced fermionic Dark Matter, whose interactions with the Standard Model can be described by an effective theory, the bounds are such that light DM candidates ($\lesssim$ 10 GeV) are basically excluded whatever the type of interactions they have with the SM fermions. Besides, heavier candidates ($\gtrsim$ 20GeV) are excluded if they have scalar-like interactions. If they have vector-like interactions, their couplings should be highly hadrophobic.

- An important conclusion is that models with light candidates, which are mainly coupled to electrons (which are favoured by experiments as INTEGRAL), are excluded by the bounds coming from LEP and Tevatron.

- More exotic models, as those containing DM candidates which do not couple to electron or lightest quarks, can escape the conclusions mentioned above, because then the bounds coming from LEP and Tevatron can not be applied.

- We have also computed the predictions of several Dark Matter Models for the synchrotron radiation fluxes reaching the Earth at radio frequencies, which has been used to put bounds on those models from existent experimental constraints. We have done this taking into account all sources of uncertainties, as the galactic magnetic field, the cosmic ray diffusion model and the dark matter density profile. The calculation has been performed semi-analytically and verified by full numerical analyses.

- We have compared the bounds coming from synchrotron radiation, with those coming from various colliders: LEP, Tevatron and LHC, as well as with other bounds coming from indirect detection, as White Dwarfs and CMB measurements. Also, for one particular model, we have made the comparison with bounds coming from XENON experiment of direct detection.

- The conclusion is that the bounds coming from synchrotron radiation are competitive with those from the rest of experiments. This conclusion depends of course on the assumed uncertainties for the background contributions, coming from standard astrophysical sources. However, for reasonable uncertainties, of the order of 5–10%, the data coming from synchrotron are able to exclude regions of the parameter space of these models for which other experiments are less sensitive, although there are some regions for which synchrotron bounds are less constraining.

CHAPTER 8

CONCLUSIONES

A continuación menciono brevemente las conclusiones principales de los trabajos de esta tesis.

En relación al mecanismo de Seesaw y Lepton Flavour Violation:

- La creencia (extendida entre la comunidad) de que en modelos Seesaw supersimétricos $BR(\mu \to e\gamma)$ depende fuertemente del valor de θ_{13}, no es correcta, como demuestra un cuidadoso estudio tanto analítico como numérico, en el cual se ha escaneado el espacio de parámetros del Seesaw de forma completa usando dos parametrizaciones alternativas.

- La potencial dependencia de $BR(\mu \to e\gamma)$ en θ_{13} se da principalmente a través de la matriz $Y_\nu^\dagger Y_\nu$, donde Y_ν es la matriz Yukawa de los neutrinos. En una de las parametrizaciones utilizadas (la llamada "parametrización$-V_L$") esta magnitud es trivialmente insensible a θ_{13}, o a cualquier otro parámetro observable; por lo que $BR(\mu \to e\gamma)$ lo es también. En la otra parametrización ("parametrización$-R$"), la cantidad $Y_\nu^\dagger Y_\nu$ depende en principio de θ_{13}, pero esa dependencia desaparece al hacer un scan completo del espacio de parámetros. Por tanto, el resultado es consistente en las dos parametrizaciones, como era de esperar.

- En el trabajo obtenemos unas reglas muy simples para escanear de forma completa la matriz R de la segunda parametrización, respetando la condición de que los acoplos de Yukawa sean perturbativos (estas reglas son válidas tanto para el Seesaw supersimétrico o el no supersimétrico) .

- Un resultado importante es que los valores de $BR(\mu \to e\gamma)$ en el Seesaw supersimétrico son típicamente más grandes que muchos de los reportados en la literatura (y por

encima de las cotas experimentales). Esto se debe básicamente a que cuando se realiza el scan completo, se accede a regiones de valores la matriz R que no habían sido consideradas antes.

- Cuando se incluye el requisito de una leptogénesis exitosa en el análisis el resultado no cambia en esencia; es decir, la condición de leptogenesis no introduce dependencias extras de $BR(\mu \to e\gamma)$ en θ_{13}. Sin embargo sí afecta a sus valores permitidos, pues tiende a seleccionar valores bajos del BR.

En resumen, la conclusión de la primera parte de la tesis es que un scan completo del espacio de parámetros de la matriz R (para el cual damos reglas precisas) es necesario en orden a sacar conclusiones generales sobre las predicciones del escenario del Seesaw. Esto no ha sido tomado en cuenta en una parte de los trabajos en la literatura previa, y por tanto lo consideramos como una línea de investigación interesante para ser explorada en proyectos futuros.

En relación con la fenomenología de Materia Oscura:

- Hemos calculado el porcentaje de acoplo hadrónico necesario (con respecto al leptónico) de la Materia Oscura con las partículas del Modelo Estándar para que ésta sea consistente con los datos de WMAP, XENON, LEP y Tevatron. Para los dos últimos experimentos los datos relevantes provienen de considerar estados finales de un fotón (en el caso de LEP) o un jet (en el caso de Tevatron) más energía perdida.

- Hemos mostrado que si la Materia Oscura está hecha de fermiones, está generada de forma térmica y su interacción con las partículas observables puede ser descrita con una teoría efectiva, entonces los candidatos ligeros ($\lesssim$ 10GeV) están básicamente excluidos cualquiera sea el tipo de interacción que tengan con el resto de fermiones del Modelo Estándar. Además, los candidatos más pesados ($\gtrsim$ 20GeV) están también excluidos si esas interacciones son de tipo escalar y están forzados a tener acoplos hadrónicos muy suprimidos si son de tipo vectorial.

- En este mismo marco general, una conclusión importante es que los modelos con candidatos ligeros principalmente acoplados a electrones, que son favorecidos por experimentos como INTEGRAL, resultan estar excluidos por las cotas de LEP y Tevatron.

- Modelos más exóticos, los cuales por ejemplo contengan candidatos a Materia Oscura que no se acople al electrón o a los quarks más ligeros, pueden escapar las conclusiones anteriores, ya que entonces las cotas de LEP y Tevatron no pueden aplicarse.

- Se ha calculado las predicciones de varios modelos de Materia Oscura sobre los flujos de radiación de sincrotrón a frecuencias de radio, y por tanto, hemos sido capaces de poner cotas a los modelos considerados provenientes de datos experimentales existentes. Esto se ha hecho tomando en cuenta todas las fuentes de error presentes en el cálculo estándar del flujo, como son el campo magnético de la galaxia, el modelo de difusión de rayos cósmicos o el perfil de densidad de energía de la Materia Oscura. El cálculo se ha hecho de forma semi-analítica, y ha sido verificado por herramientas numéricas.

- Hemos comparado la potencia de las cotas provenientes de los flujos de radiación sincrotrón, con la de las que provienen de los colisionadores de partículas, como LEP, Tevatron y LHC; así como con la de otras cotas de detección indirecta, como flujos desde Enanas Blancas y mediciones del CMB. Además, para uno de los modelos comparamos también con las cotas provenientes del experimento XENON de detección directa.

- La conclusión es que las cotas provenientes de la radiación de sincrotrón son competitivas con las del resto de los experimentos. Esta conclusión depende de las incertidumbres que se asuman para las contribuciones de "background", proveniente de procesos astrofísicos estándar. Pero para incertidumbres razonables, del orden del 5–10%, los

datos de sincrotrón son capaces de excluir regiones del espacio de parámetros de los escenarios anteriores, insensibles a los otros experimentos; si bien en otras regiones los datos de sincrotrón son menos sensibles.

Appendices

APPENDIX A

CORRECTED BOLTZMANN EQUATION

In this appendix I continue to analyse the Boltzmann equation, without assuming a Maxwell-Boltzmann distribution function for the bath particles which, as we have seen, should not be -a priori- valid for the $m_{\rm bath} \lesssim T$ regime.

The collision operator C_B of the Boltzmann equation -i.e. the RHS of (3.33)- should describe how the number density of a species changes in time, assuming the system is a FLRW gas of particles with defined distribution functions. First of all, I revert back the simplified Boltzmann equation (3.38), which can be rewritten as

$$a^{-3}\frac{d(n_\chi a)}{dt} = \langle\sigma v\rangle_{b\bar{b}\to\chi\bar{\chi}} n_b^2 - \langle\sigma v\rangle_{\chi\bar{\chi}\to b\bar{b}} n_\chi^2 \equiv C_Y \ , \tag{A.1}$$

where I made explicit that in principle the annihilation cross-section of the bath differs from that of DM. n_b is the number density of the bath particles. Next I will show that this equation corresponds to a thermal bath which (as the DM) follows a Maxwell-Boltzmann distribution function. Indeed we have

$$\begin{aligned} C_Y \ &\supset \ \langle\sigma v\rangle_{b\bar{b}\to\chi\bar{\chi}} n_b^2 \\ &= \ \frac{n_b^2}{(n_b^{\rm eq})^2}\int\prod_{i=1}^{4}\frac{d^3p_i}{(2\pi^3)2E_i}(2\pi)^4\delta^{(4)}(p_{\rm in}-p_{\rm out})|\mathcal{M}|^2 f_b^{\rm eq} f_{\bar{b}}^{\rm eq} \ , \end{aligned} \tag{A.2}$$

where the equilibrium distributions $f^{\rm eq}$ have zero chemical potentials. So the only way to recover the original -exact- collision operator

$$C_B \supset \int\prod_{i=1}^{4}\frac{d^3p_i}{(2\pi^3)2E_i}(2\pi)^4\delta^{(4)}(p_{\rm in}-p_{\rm out})|\mathcal{M}|^2 f_b f_{\bar{b}} \tag{A.3}$$

is if the f_b can be expressed as a product of functions of μ_b and E_b only, which is realised in the Maxwell-Boltzmann form, where $f_b(\mu_b, E_b)/f_b^{\rm eq}(E_b) \approx e^{\mu_b/T} = n_b/n_b^{\rm eq}$.

Search for a more complete expression

The original equation (3.33), after doing the reasonable simplification of considering the DM (but not the bath particles) to follow a Maxwell-Boltzmann distribution can be rewritten as

$$\begin{aligned} a^{-3}\frac{d(n_\chi a)}{dt} &\approx \int \prod_{i=1}^{4} \frac{d^3p_i}{(2\pi)^3 2E_i}(2\pi)^4\delta^{(4)}(p_{\rm in}-p_{\rm out})|\mathcal{M}|^2 \\ &\times \ [f_b f_{\bar{b}} - f_\chi f_{\bar{\chi}}(1\pm f_b)(1\pm f_{\bar{b}})] \equiv \mathcal{P}-\mathcal{A}\ , \end{aligned} \tag{A.4}$$

where $\mathcal{P}$ and $\mathcal{A}$ are DM production and annihilation terms, respectively. Taking into account

$$\begin{aligned} \int \frac{d^3p_b}{(2\pi)^3 2E_b}\frac{d^3p_{\bar{b}}}{(2\pi)^3 2E_{\bar{b}}} &= \frac{1}{64\pi^4}\int dE_b dE_{\bar{b}} ds\ , \\ \int \frac{d^3p_\chi}{(2\pi)^3 2E_\chi}\frac{d^3p_{\bar{\chi}}}{(2\pi)^3 2E_{\bar{\chi}}}(2\pi)^4\delta^{(4)}(p_{\rm in}-p_{\rm out}) &= \int \frac{d^3p_\chi}{(2\pi)^3 2E_\chi}\frac{d^3p_{\bar{\chi}}}{(2\pi)^3 2E_{\bar{\chi}}} \\ &\times \ (2\pi)\delta(\sqrt{s}-E_\chi-E_{\bar{\chi}})(2\pi)^3\delta^{(3)}(\vec{p}_\chi+\vec{p}_{\bar{\chi}}) \\ &= \frac{1}{32\pi^2 s}\sqrt{(s-2m_\chi^2)^2-4m_\chi^4}\int d\Omega_{\chi\bar{\chi}}\ , \end{aligned} \tag{A.5}$$

we can express $\mathcal{P}$ as

$$\mathcal{P} = \frac{1}{64\pi^4}\int dE_b f_b \int dE_{\bar{b}} f_{\bar{b}} \int ds \frac{1}{32\pi^2 s}\sqrt{(s-2m_\chi^2)^2-4m_\chi^4}\int d\Omega_{\chi\bar{\chi}}|\mathcal{M}|^2\ . \tag{A.6}$$

On the other hand, the annihilation term $\mathcal{A}$ contains a term proportional to $f_\chi f_{\bar{\chi}} f_b f_{\bar{b}}$, which allows us to factorise the integral, so having

$$\begin{aligned} \mathcal{A} &\supset \frac{1}{64\pi^4}\int dE_\chi\ e^{-(E_\chi-\mu_\chi)/T}\int dE_{\bar{\chi}}\ e^{-(E_{\bar{\chi}}-\mu_{\bar{\chi}})/T} \\ &\times \int ds \int \frac{d^3p_b}{(2\pi)^3 2E_b}\frac{d^3p_{\bar{b}}}{(2\pi)^3 2E_{\bar{b}}}(2\pi)^4\delta^{(4)}(p_{\rm in}-p_{\rm out})|\mathcal{M}|^2 f_b f_{\bar{b}} \\ &= \frac{1}{64\pi^4}\int dE_\chi\ e^{-(E_\chi-\mu_\chi)/T}\int dE_{\bar{\chi}}\ e^{-(E_{\bar{\chi}}-\mu_{\bar{\chi}})/T} \\ &\times \int ds \frac{1}{32\pi^2 s}\sqrt{(s-2m_b^2)^2-4m_b^4}(f_b f_{\bar{b}})|_{E_{b,\bar{b}}=\sqrt{s}/2}\int d\Omega_{b\bar{b}}|\mathcal{M}|^2\ . \end{aligned} \tag{A.7}$$

in the absence of the $f_b f_{\bar{b}}$ factor, the above expression would be equal to $n_\chi n_{\bar{\chi}}\langle\sigma v\rangle_{\chi\bar{\chi}\to b\bar{b}}$. So the complete expression for $\mathcal{A}$ is:

$$\begin{aligned} \mathcal{A} &= n_\chi n_{\bar{\chi}}\langle\sigma v\rangle_{\chi\bar{\chi}\to b\bar{b}} + \frac{1}{64\pi^4}\left(\int dE_\chi\ e^{-E_\chi/T}\right)^2 \\ &\times \ \frac{1}{32\pi^2}\int ds d\Omega_{b\bar{b}}\frac{1}{s}\sqrt{(s-2m_b^2)^2-4m_b^4}|\mathcal{M}|^2\,[f_{\bar{b}}f_b \pm f_b \pm f_{\bar{b}}]_{E_{b,\bar{b}}=\sqrt{s}/2}\ . \end{aligned} \tag{A.8}$$

It is straightforward to show from (A.6) and (A.8) that in the limit where $f_{b,\bar{b}}$ follow a Maxwell-Boltzmann law, (A.4) reduces to the familiar equation (A.1).

Let us take a closer look at (A.8). There we see that the bath distribution functions $f_{b,\bar{b}}$ are evaluated at $E_{b,\bar{b}} = \sqrt{s}/2$, with $\sqrt{s} \geq 2m_\chi$. This means that even if in the large majority of cases $E_b \sim T$, for the reaction to occur one must have quite energetic bath particles: $E_b \sim m_\chi$. Thus energy conservation forces the energy of the bath particles to be close to the DM mass, for the process to take place. When this happens, the bath distribution function has a value very similar to the one given by its Maxwell-Boltzmann approximation, because $E_b \sim m_\chi >> T$.

A similar situation occurs for the production term (A.6). The integrals over $E_{b,\bar{b}}$ are sensitive to m_χ, because if $m_b << s$:

$$s = 2m_b^2 + 2E_bE_{\bar{b}} - 2|\vec{p}_b||\vec{p}_{\bar{b}}|\cos\theta_{b\bar{b}} \approx 2E_bE_{\bar{b}}(1-\cos\theta_{b\bar{b}}) \tag{A.9}$$

So the integration limits can be expressed as

$$\int_{m_b}^{\infty} E_b \int_{s/4E_b}^{\infty} E_{\bar{b}} \, . \tag{A.10}$$

So for very large masses m_χ, s -and thus- E_b are very large, making the distribution function f_b very suppressed, and close in value to its Maxwell-Boltzmann approximation.

To summarise: the energy conservation $E_b + E_{\bar{b}} = E_\chi + E_{\bar{\chi}}$ forces the bath distributions functions to behave very similarly to their Maxwell-Boltzmann approximations.

LIST OF FIGURES